Corneal Light Scattering following Excimer Laser Surgery

Dirk De Brouwere

June 2008

Thesis submitted in partial fulfilment of the requirements for the degree of Doctor of Philosophy of the University of Crete.

University of Crete

CORNEAL LIGHT SCATTERING FOLLOWING EXCIMER LASER SURGERY

Submitted June 6^{th}, 2008

Supervised by:

Ioannis G Pallikaris	Professor in Ophthalmology , University of Crete
	Rector of the University of Crete
Miltiadis K Tsilimbaris	Assistant Professor, University of Crete
	Director of the Eye Clinic of the University Hospital, Heraklion
Konstandinos C Fotakis	Professor in Physics, University of Crete
	Director of Institute of Electronic Structure and Laser

Members of the examination committee :

Ioannis G Pallikaris	Professor in Ophthalmology , University of Crete
	Rector of the University of Crete
Konstandinos C Fotakis	Professor in Physics, University of Crete
	Director of Institute of Electronic Structure and Laser
Theofanis Kitsopoulos	Professor in Chemistry, University of Crete
	Vice Rector of the University of Crete
	Chairman, Department of Chemistry
Miltiadis K Tsilimbaris	Assistant Professor, University of Crete
	Director of the Eye Clinic of the University Hospital, Heraklion
Michalis Taroudakis	Associate Professor, University of Crete
Dimitris Papazoglou	Lecturer, University of Crete
Charalampos Siganos	Assistant Professor, University of Crete

- 2008 -

Abstract

Introduction Increased corneal scattering is assumed to be a considerable side-effect of refractive surgery due to the postoperative healing response after photoablative surface treatments. Clinically, corneal scattering is associated with haze development. Corneal haze is subjectively evaluated method based on the observation of the light backscattered on the cornea as seen under a slit lamp. However, corneal light scattering affects the retinal image quality only by its forward scattering component. The scope of this thesis is to evaluate the the effect of corneal light scattering on the retinal image quality, specifically in relation to the morphological changes in the cornea following excimer laser surgery.

Methods Initially, the optical mechanisms of the image formation on the retina are discussed. Following, the optical parameters of the corneal morphology are characterized to form a theoretical model describing the forward light scattering in the cornea. Simulation of this theoretical model is done by a physical model of light scattering on microspheres. This model is evaluated both by psychophysical and optical measurements. Further, we compared the use of two psychophysical and three optical methods to evaluate both the amount of light scattered in the cornea and the angular distribution of the scattered light.

Results Based on histological data of stained corneal samples and in vivo confocal microscopy, the morphologic corneal changes addressed to the wound healing response are induced by the activation of keratocytes, inhibiting a newly formed unorganized collagen layer, a scar tissue called the foam layer. The theoretical models developed in

this thesis reveal the presence of scattering particles that cause a local distortion of the incoming wavefront. The point spread function of this scattered wavefront is strongly forward distributed with a full width at the half maximum of approximately 20 minutes of arc. After refractive treatments, the light scattering increases until 1 month after treatment, reducing to a long term moderate level of increased light scattering after 6 months. Moreover, we derived that where, in a healthy cornea approximately 20 percent of the incoming light is scattered, this value increases up to 70 percent for corneas with marked haze. Furthermore, psychophysical data suggest that the amount of light scattered over angles from 5 to 10 degrees increases in a similar extend as observed in the ageing eye.

Conclusion The wound healing response of the cornea on photorefractive ablation treatments result in an increase of corneal scattering. The light distribution of this scattered light is narrowly forward peaked. Correlation of the foam layer with amount of forward light scattering suggests that the increased corneal scattering following refractive surgery mainly originates on this foam layer. Therefore, a correct postoperative care of the cornea following excimer laser surgery is detrimental for an optimal retinal image quality. The effect of light scattering in the eye results on a lowering of the contrast sensitivity and an increased disability glare around light sources in night vision.

Περίληψη

Εισαγωγή Η αυξανόμενη σκέδαση στον κερατοειδή, θεωρείται ένα αξιοσημείωτο μειονέκτημα της διαθλαστικής χειρουργικής, η οποία εμφανίζεται λόγω της μετεγχειρητικής επουλωτικής δραστηριότητας που αναπτύσσει ο κερατοειδής, μετά από επεμβάσεις φωτοαποδόμησης της επιφάνειας του. Σε κλινικό επίπεδο, η σκέδαση στον κερατοειδή συνδέεται με την θόλωση του. Η θολερότητας του κερατοειδή σήμερα, υπολογίζεται υποκειμενικά μεσω παρατήρησης με χρήση σχισμοειδούς λυχνίας, του φωτός που σκεδάζεται προς τα πίσω από το κερατοειδή. Ωστόσο, η σκέδαση του φωτός στον κερατοειδή, επηρεάζει την ποιότητα του αμφιβληστροειδικού ειδώλου λόγω της ποσότητας του φωτός που σκεδάζεται στην κατεύθυνση διάδοσης του. Ο σκοπός αυτής της διατριβής, είναι να αποτιμήσει την επίδραση που έχει η σκεδαζόμενη από στον κερατοειδή ακτινοβολία στην ποιότητα του αμφιβληστροειδικού ειδώλου, και ειδικότερα σε σχέση με τις μορφολογικές αλλαγές που υφίστατι ο κερατοειδής μετά από επεμβάσεις με την χρήση excimer laser.

Μέθοδοι Αρχικά, γίνεται αναφορά στους μηχανισμούς οπτικής απεικόνισης ενός αντικειμένου στον αμφιβληστροειδή. Στην συνέχεια, εξετάζονται οι οπτικοί παράμετροι της μορφολογίας του κερατοειδή, έτσι ώστε να αναπτυχθεί ένα θεωρητικό μοντέλο που θα περιγράφει την σκέδαση του φωτός, κατά την διεύθυνση διάδοσης του, στον κερατοειδή. Η προσομοίωση αυτού του θεωρητικού μοντέλου έγινε με ένα φυσικό μοντέλο σκέδασης της H/M ακτινοβολίας από μικροσφαιρίδια. Τα ποσοστά σκέδασης και η κατανομή της σκεδαζόμενης, από το φυσικό αυτό μοντέλο, H/M ακτινοβολίας μελετήθηκαν με ψυχοφυσικές αλλά και οπτικές μετρήσεις. Στην συνέχεια, έγινε σύγκριση μεταξύ δύο ψυχοφυσικών και τριών οπτικών μεθόδων που χρησιμοποιήθηκαν για την αποτίμηση τόσο του ποσοστού της σκεδαζόμενης από τον κερατοειδή H/M ακτινοβολίας όσο και της γωνιακής

κατανομής της.

Αποτελέσματα Βασισμένοι σε ιστολογικά δεδομένα από μελέτες κερατοειδικών δειγμάτων αλλά και την χρήση της οπτικής μικροσκοπίας στην in vivo μελέτη του κερατοειδούς, προκύπτει ότι οι μορφολογικές αλλαγές που παρατηρούνται κατά την ανάπτυξη της επουλωτικής δραστηριότητας του κερατοειδούς, προκαλούνται από την ενεργοποίηση των κερατοκυττάρων. Τα ενεργοποιημένα κερατοκύτταρα αναπτύσσουν ένα στρώμα νέων ινών κολλαγόνου, οι οποίες ωστόσο είναι διατεταγμένες με τυχαίο προσανατολισμό, δημιουργώντας έτσι ένα στρώμα ουλώδη ιστού (foam layer). Το θεωρητικό μοντέλο που αναπτύχθηκε, αποκαλύπτει την παρουσία σωματιδίων που σκεδάζουν την H/M ακτινοβολία, προκαλώντας την τοπική αλλοίωση του εισερχόμενου, στο οπτικό σύστημα του οφθαλμού, μετώπου κύματος. Η συνάρτηση διασποράς σημείου (PSF) του σκεδαζόμενου μετώπου κύματος, κατανέμεται ισχυρά στην κατεύθυνση διάδοσης του φωτός, με το πλάτος στο ήμισυ του μεγίστου της κατανομής (FWHM) να είναι 20 arcmin. Μετά από διαθλαστικές επεμβάσεις, το ποσοστό της σκεδαζόμενης ακτινοβολίας αυξάνεται μέχρι τον πρώτο μήνα μετά την επέμβαση, και μειώνεται σε ένα μικρότερο βαθμό μετά από έξι μήνες. Επιπλέον, ενώ σε υγιείς κερατοειδείς περίπου το 20% της εισερχόμενης H/M ακτινοβολίας σκεδάζεται, αυτό το ποσοστό αυξάνεται σε 70% για κερατοειδείς με σημαντικό ποστσό θολερότητας. Επιπροσθέτως, δεδομένα που προέκυψαν από ψυχοφυσικές μετρήσεις, οδηγούν στο συμπέρασμα ότι το ποσοστό της ακτινοβολίας που σκεδάζεται σε γωνίες από 5deg έως 10 deg, αυξάνεται σε μια αντίστοιχη έκταση με αυτήν που παρατηρείται σε οφθαλμούς μεγάλης ηλικίας.

Συμπεράσματα Η επουλωτική δραστηριότητα που αναπτύσσει ο κερατοειδής σαν αντίδραση σε διαθλαστικές επεμβάσεις φωτοαποδόμησης του, προκαλεί την αύξηση της σκεδαζόμενης από τον κερατοειδή H/M ακτινοβολίας. Η κατανομή της σκεδαζόμενης ακτινοβολίας είναι ισχυρά συγκεντρωμένη στην κατεύθυνση διάδοσης της. Συσχετίζοντας την σκεδαζόμενη ακτινοβολία με την νέο στρώμα των ινών κολλαγόνου που αναπτύσσεται στον κερατοειδή μετά από διαθλαστικές επεμβάσεις, προκύπτει ότι τα αυξημένα ποσοστά σκέδασης οφείλονται στην παρουσία του νέου αυτού στρώματος (foam layer). Έτσι, μια σωστή μετεγχειρητική θεραπεία του κερατοειδή μετά από επεμβάσεις με excimer laser είναι

καθοριστική για μια καλύτερη ποιότητα αμφιβληστροειδικού ειδώλου. Η επιρροή της σκεδαζόμενης ακτινοβολίας στην όραση, συνίσταται στην μείωση της ευαισθησίας φωτεινής αντίθεσης και την εμφάνιση αυξημένης λάμψης γύρω από φωτεινές πηγές κατά την νυχτερινή όραση.

Acknowledgements

During the writing of my Phd thesis, I consistently conjugated the verbs in the *plural* form. This is because the thesis I am presenting in this book could not be completed without the help of several people who have given me ideas, supported me or spent long days in the lab to establish this thesis.

We is in the first place also Harilaos Ginis, a great supervisor, scientist and friend, who gave me his hospitality since the first day I arrived in Crete, the many ideas (and coffees) he brough me and the ideal supervising of my work in BEMMO.

Professor Pallikaris, who gave me the opportunity to work in a lab where new ideas are supported from the early stage to the clinical implementatio.

The coordinators and members of the RTN network *SharpEye*, that has funded the major part of this thesis. Thanks for the very interesting meetings and discussions.

The MSc students Giannis Sgouros, Iro Pentari, Tassos Papadiamantis, Trisevgeny Giannakopoulou and Kelly Giannakoudaki whose master projects had lead to a significant contribution of my thesis.

Professor Molebny, who came up with the idea of evaluating corneal light scattering after refractive surgery, Juanma Bueno and Tom van den Berg, who have conducted very interesting work in the field of ocular scattering and whom we had the luck to establish a constructive collaboration with.

Scott Hampton for his support and collaboration for the development and evaluation of the single pass in vitro characterization of corneal scattering.

Giannis Staviannoudakis who was always ready to manufacture the necessary tools to build a laboratory setup.

Thanks also to Daniel Sahagun for the careful proof reading of the manuscript.

The entire team of BEMMO and the eye clinic in the UH in Heraklion, who taught me during the many discussions about the basics of clinical ophthalmology, biology and optometry. This has given me a broad background in the field.
My family and friends in Belgium, for their visits, the beers and chocolates they brought me and the warm home that was waiting for me every time I went to Belgium.
So far, my time in Crete has been of the best life experience I could imagine. Not only the wonderful nature and the warm spirit of the Cretan people, the lifestyle of the Cretan windsurfers, the sailing company, but mostly the friends who have been part of *my family* here in Crete, who shared the joy and pleasure of this island, and who give me a place where I always felt home. $\epsilon\upsilon\chi\alpha\rho\iota\sigma\tau\omega$!

Contents

Chapter 1

Introduction

Light scattering in the eye is a natural phenomenon caused by the local variation of optical properties of the ocular tissue. In the anterior part of the eye, the cornea and the crystalline lens consist of cells and a connective tissue that are the sources of light scattering affecting the visual function. However light scattering affects the visual function as well in healthy young eyes, certain pathologies tend to arise increased light scattering that can drastically reduce the image quality on the retina. These pathologies can be the result of the a wound healing response after injury, inflammation or infection at the cornea or a degeneration of the crystalline or corneal collagen tissue. Whereas in a young healthy eye, the lens and the cornea contribute to the same amount of scattered light on the retina, it is known that the ageing eye significantly increases light scattering in the crystalline lens [27][25] [59]. Thus, most researchers have focused their study on the ocular light scattering to lens scattering [2]. However corneal light scattering does not significantly increase with age, it is the part of the eye which is directly exposed to the environment and therefore more vulnerable to injuries.

The advances in refractive surgery have lead to several reliable techniques for the correction of the refractive error in the eye [40][43]. Laser ablation of the cornea though causes a trauma on its tissue and the morphologic changes related to the resulting wound healing response can lead to increased scattering in the cornea [11] [36] [29] . At present, corneal scattering is usually clinically quantified by haze [13] [30] [52], which is a subjective estimation of the light backscattered from the cornea. Whereas backscattered light on the cornea does not affect the retinal image quality, most light

scattered on the cornea is narrowly forward directed, giving rise to reduction of the image quality. Therefore, a profound study on the forward light scattering properties in the eye is needed [3]. The aim of this thesis is to quantify the amount of light scattering addressed to the morphologic changes after refractive laser treatments and its affect on the retinal image quality.

The basics of the image formation on the retina are presented in Chapter 2, which is a general description of the optical parameters as refraction, higher order aberrations and light scattering affecting the retinal image quality. Also, a brief overview of the state of the art in refractive surgery is given.

The optical irregularities causing ocular light scattering are inherent to the biological nature of the corneal and crystalline tissue. For this reason, Chapter 3 gives a study of the present morphologic structures in the eye leading to light scattering and also the natural mechanisms wound healing response in the cornea after laser ablation. Finally, some methods aimed to reduce the contribution of light scattering on retinal image quality are described in this chapter.

As previously mentioned, light scattered in the eye has a narrowly forward peaked intensity distribution. The angular scattering distribution is detrimental for the image quality affected by the scattered light. In Chapter 4 several theoretical models are proposed to describe the angular distribution of corneal light scattering based on the scattering properties of the cornea.

Based on a theoretical scattering model, we developed a physical model to simulate corneal scattering based on microspheres suspended in a set of custom made contact lenses. The description and characterization of this model is presented in Chapter 5.

Most data available on ocular scattering are based on psychophysical measurements, i.e. a description of the 'glare' that an observer perceives in the periphery of an intense source. In Chapter 6, we give an overview of the present psychophysical methods for quantification of this glare and a derived mathematical description of the perceived point spread function (PSF) , generally known as the 'glare spread function'.

Chapter 7 describes a range of optical methods that we developed for the optical characterization of forward light scattering in the cornea. Finally, the effect of light scattering on the visual function is evaluated in Chapter 8.

Chapter 2

Image Formation on the Retina

"The eye is an example of robust optical design"

Pablo Artal [1]

One could compare the optics of the eye with a camera, where the refractive parts consisting of the cornea and the lens form an image sampled on the retina. This chapter gives an overview of the optical properties of the eye that contribute to the image quality on the retina.

2.1 Optical resolution

2.1.1 Rayleigh criterium

The resolution of an optical system is generally defined by the smallest angle under which two points can be discriminated. A decisive function that controls this resolution is the point spread function (PSF). The PSF describes the light distribution of a point source imaged on a plane through and optical system.

In a perfect optical system with a circular entrance pupil, the PSF is defined

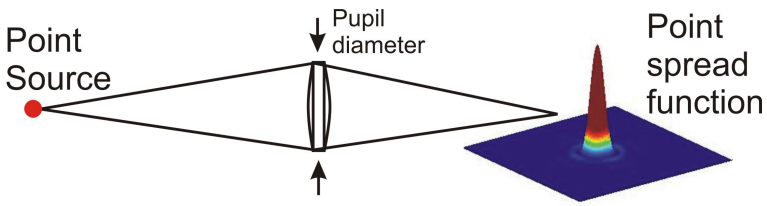

Figure 2.1: Impulse response of an optical system

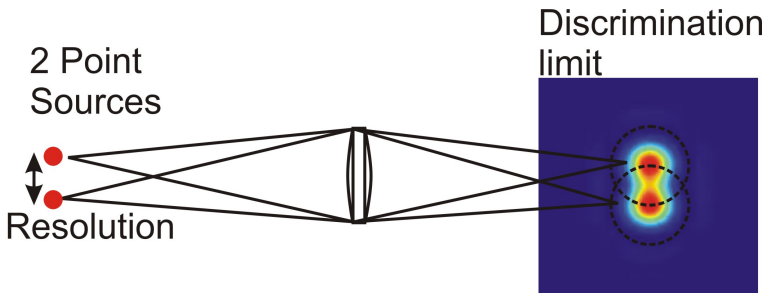

Figure 2.2: Angular resolution in a diffraction limited system

by the pupil diameter and the wavelength of the incident light (figure 2.1). The mathematical derivation of the PSF is based on Fourier optics [23]. The result is the following function:

$$I(\theta) \simeq [\frac{J_1(\frac{kd\theta}{2})}{\frac{kd\theta}{2}}]^2 \tag{2.1}$$

Where J_1 is a first order Bessel function, d is the pupil diameter and k describes the wavenumber $\frac{2\pi}{\lambda}$ with the wavelength λ. The pattern describes by this function is generally known as the 'Airy pattern' When two point sources approach very close, their PSF on the image plane will overlap. Usually the angular resolution is defined by the *Rayleigh Criterium* as the angular separation where the maximum of the second point overlaps with the first minimum in the airypattern of the first point. The above described perfect optical system is called a *diffraction limited* system. Its resolution is:

$$\theta_{lim} = 1.22\frac{\lambda}{d} \tag{2.2}$$

The given configuration is illustrated in figure 2.2.

2.1.2 Optical aberrations

Ray Tracing

A perfect lens mounted in an optical system focusses the light from an object to an image. The local curvature of the lens surface will refract each beam coming from an object to its image. The method of tracing an appropriate number of rays coming from an object to its image through the optical system is called *ray tracing*. Abberations are present even in perfect rotationally symmetric surfaces; in the general case abberations

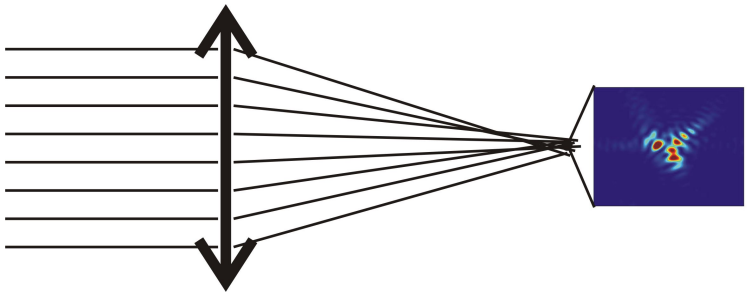

Figure 2.3: Ray tracing analysis of optical aberrations

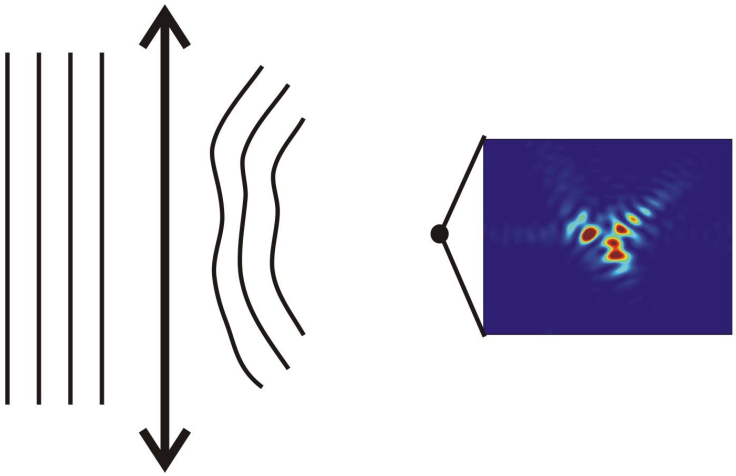

Figure 2.4: Wavefront analysis of an aberrated optical surface

are not related to irregularities, the are related to the fact that standard surfaces (eg. spheres) are not ideal for image formation. When tracing all the rays through its optical irregularities, we obtain an extended image of the point source (figure 2.3). The irregularities on the optical surfaces are called the optical aberrations.

Wavefront analysis

The optical aberrations on a lens surface are generally described by wavefront optics. Indeed, the surface irregularities that cause the aberrations lead to a local retardation of the wavefront (figure 2.4).

The image transfer through an aberrated surface is described by Fourier optics. The PSF of an image formed through an aberrated surface can be reconstructed when the optical aberrations are precisely described. A common description of the ocular aberrations in done by the Zernike polynomials [1][37][46]. The lower order Zernike

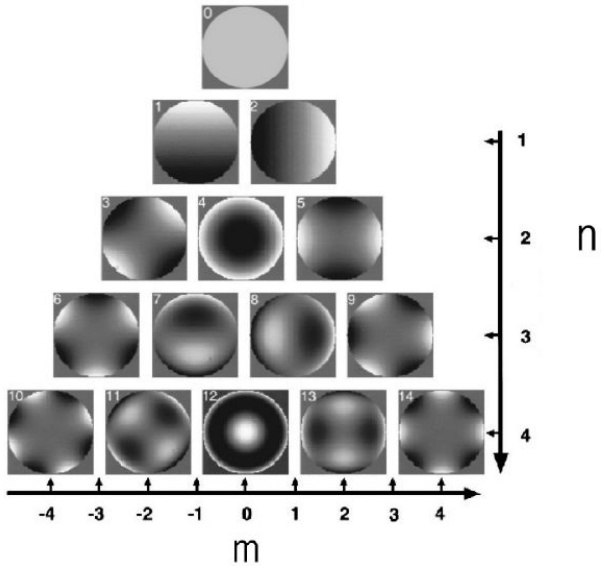

Figure 2.5: The Zernike functions

functions correspond to the common refractive errors as defocus and astigmatism, whereas the higher order Zernike functions correspond to more complex surfaces. Given the fast convergence of the Zernike expansion to describe the ocular aberrations, usually only Zernike coefficients up to the third order are taken into consideration. Figure 2.5 illustrates the a set of Zernike functions.

2.1.3 Measurement of wavefront aberrations

In the last decade, several methods have been applied for the ocular wavefront aberrations. Most of these techniques are based on double pass imaging and have become a reliable technique for measuring the refractive aberrations of the eye. The principle of these aberrometers is generally very similar. They are based on the propagation of a set of discrete light rays entering or exiting the eye through different positions. These rays are imaged on a CCD. The position of the image of each ray depends on the propagation direction refracted by the lens and the cornea. Calculation of the distortion of the positions of the rays on the image (CCD) plane lead to the direct measurement of the transverse ray aberration at each corresponding portion of the entrance pupil and to the subsequent reconstruction of the aberrated wavefront. The methods has recently gained interest both since the introduction of customized wavefront ablation refractive

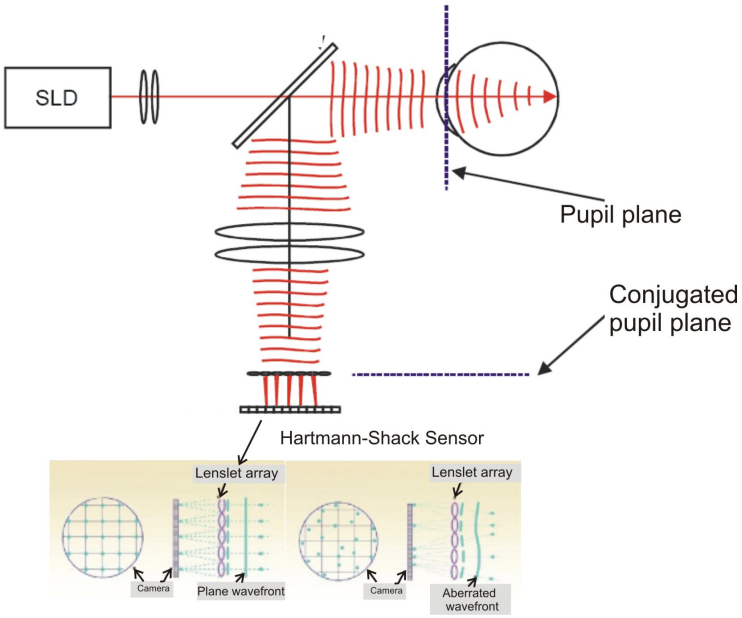

Figure 2.6: Working principle of the Hartmann-Shack wavefront sensor. Up: light propagation in the wavefront sensor. Down: Working of the lenslet array

surgery and the implementation of adaptive optics in the field of visual optics.

Below we describe the most common techniques available for wavefront sensing in the eye:

The Hartmann-Shack aberrometer uses an array of microlenses to separate the different light rays **exiting** the eye. The principle is illustrated in figure 2.6. A source laser diode (SLD) is projected on a small dot on the retina. A second optical arm is focussed to image the retinal dot on a CCD camera through a lenslet array. This array consists of microlenses that separate the incoming wavefront into a discrete set of different beams that are focussed on the CCD. The optical system is modeled to conjugate the eye's pupil on the lenslet array in order to reconstruct the the wavefront aberrations on the pupil plane.

The Tscherning aberrometer separates the light rays on a multi-subaperture mask before the light **enters** the eye. The working principle is illustrated in figure 2.7. A 10 diopters aberrometer lens shifts the focal point of the light source in front of the

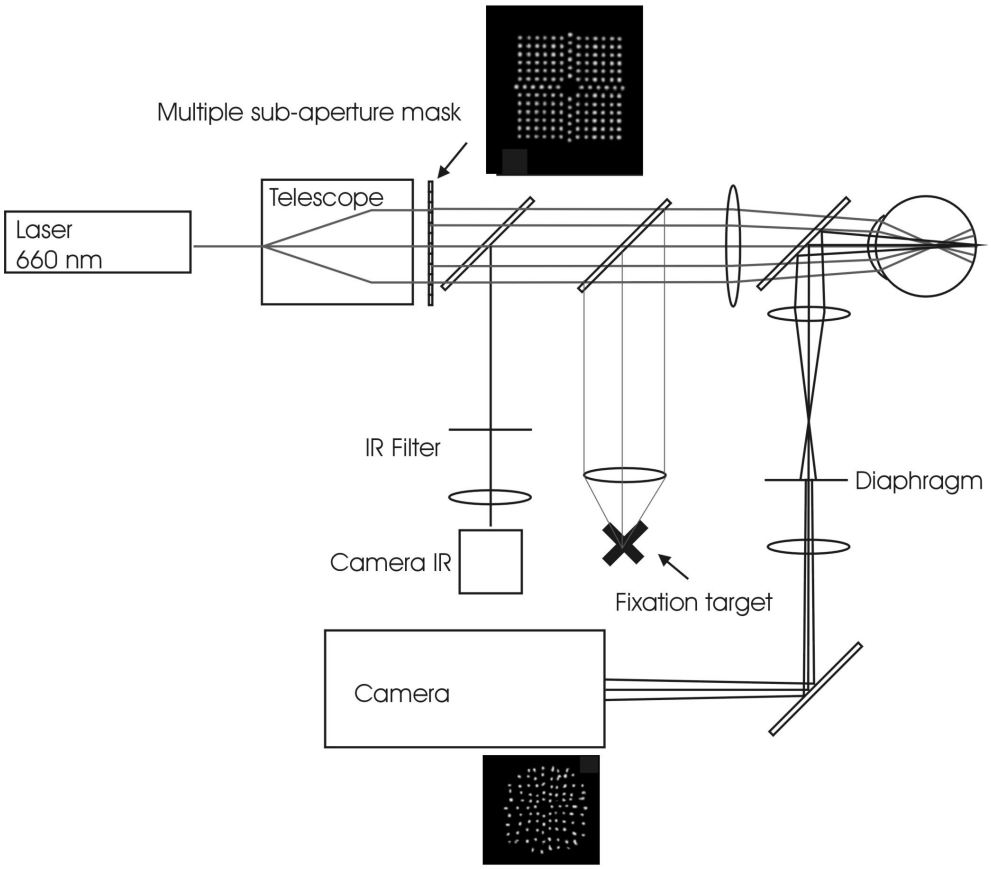

Figure 2.7: Working principle of the Tscherning wavefront analyzer.

retina so the mask is projected on the retina. The position of each spot of the masks' image on the retina depends on the local refraction of the pupil position where the beam entered the eye. In a second arm, the retinal image is reconstructed on a CCD camera.

A commercially available Tscherning aberrometer (WaveLight Wavefront Analyzer, WaveLight AG, Erlangen, Germany) has been modified for the scope of this thesis for in vivo analysis of the ocular light scattering in the eye's anterior segment. A more detailed description of the method is given in section 7.2.

The Ray Tracing aberrometer is similar to the Tscherning aberrometer. Its working is illustrated in figure 2.8. Instead of a multi subaberture mask, an acousto-optical modulator (scanner) sequentially generates a set of thin light beams. A collimator makes each beam entering the pupil parallel to the eye's optical axis, entering the pupil on a different position. Following, the position of each beam on the retina is

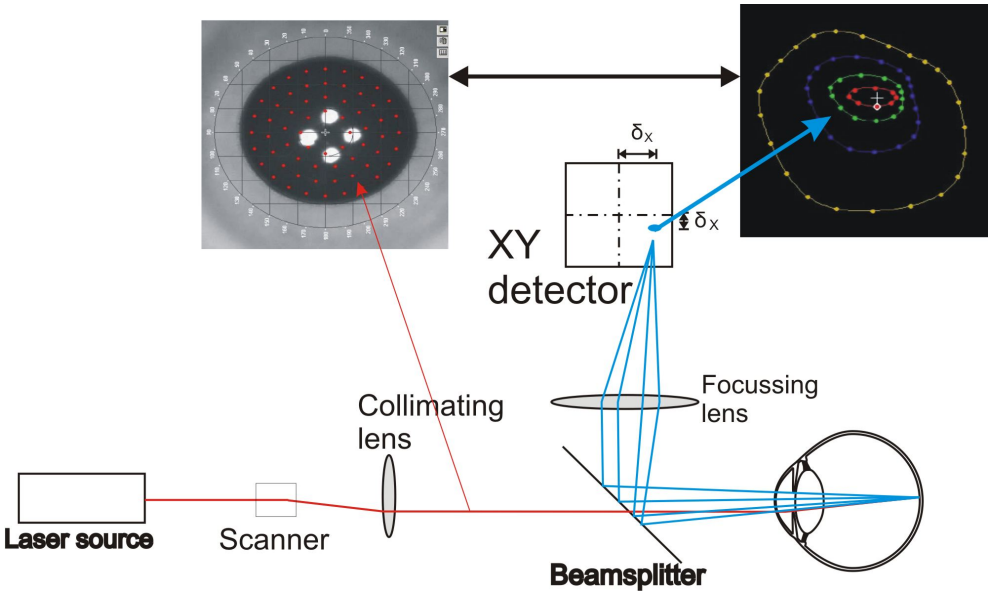

Figure 2.8: Principle working of the Ray tracing aberrometer.

sensed on an XY detector. Where a retinal map with the position of each beam is generated, than the eye's aberrated wavefront can be reconstructed.

2.2 Light scattering

Ocular light scattering is usually associated with *elastic scattering*, i.e. the scattered light has the same wavelength as the incoming wavefront. It occurs when a wavefront travels through a medium with a non-homogenous refractive index. When the wavelength of the scattered light is different from the incoming wavefront, the scattering is originated by atomic or molecular interactions between the light and the scattering particles[51]. This type of scattering is called *non-elastic scattering*. A typical case of this non-elastic scattering is fluorescence. Since non-elastic scattering in the anterior segment of the eye has only a negligible contribution on the retinal image quality, we will not discuss the phenomenon in more detail.

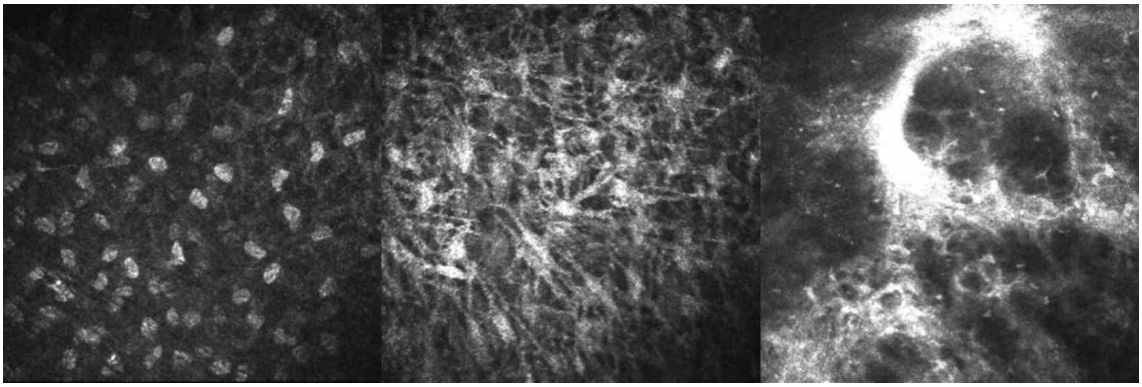

Figure 2.9: Typical images of in vivo corneal confocal microscopy (HRTII, corneal Rostock module). They represent the subepithelial stromal layer in a healthy eye (left), moderate healing response (center) and severe healing response (right). The field of view is 400x400 um

2.2.1 Origin of scattering

Light scattering on the optics of the eye

As previously mentioned, elastic light scattering occurs in media with a non-homogenous refractive index. Given the homogeneity of the vitreous and aqueous humor, we can conclude that the most light scattering in the anterior segment of the eye happens in the cornea and the crystalline lens, or at surface irregularities on the eye's refractive surfaces. A detailed description of the biologic structures in the lens and cornea causing these refractive irregularities is given in Chapter 3. As and example, figure 2.9 illustrates some scattering structures in the subepithelial stromal layer which are associated with the increased corneal scattering after photorefractive keratectomy (PRK). Since the principle of confocal microscopy is based on *"detecting"* small variations of refractive index, these images give a representative overview of the light scattering origin in the cornea.

Retinal diffusion

The retina consists of several layers that have different absorption/reflection and scattering properties. Figure 2.10 gives a schematic overview of the different layers in the retina.

In the anterior layer of the retina, a portion of the light is diffused by the blood

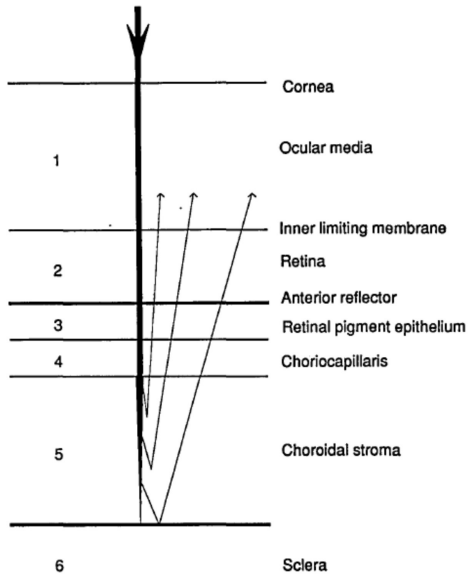

Figure 2.10: Schematic overview of the diffusive layers in the eye (Hodgkinson *et al.* [26])

vessels and capillaries. The photoreceptors do not specifically contribute to light diffusion, their behavior is described in the next paragraph. Behind the photoreceptors, there is a highly absorbing layer, the retinal pigment epithelium (RPE). The amount of light absorption in the RPE can vary between different subjects and is related to the color of the eye.

The choroid is probably the most diffusive layer in the posterior segment of the eye. It has a thickness of approximately $400\mu m$. It is believed that the scattering in the choroid comes from interactions with the melanin in the blood and the scattering distribution is forward peaked on small angles. Given the spectral absorption curve of melanin, the effect of choroidal diffusion is stronger for red light [26].

The last layer, the sclera, is assumed to be a reflector for the light that traveled through the choroid.

A precise description of the scattering properties in the retina exceeds the scope of this thesis, but we should remember from this discussion that retinal reflection can vary for different subjects. Low pigmented eyes absorb less (diffuse) light reflected from the sclera and can there overestimate the light scattering from the anterior eye segment [26].

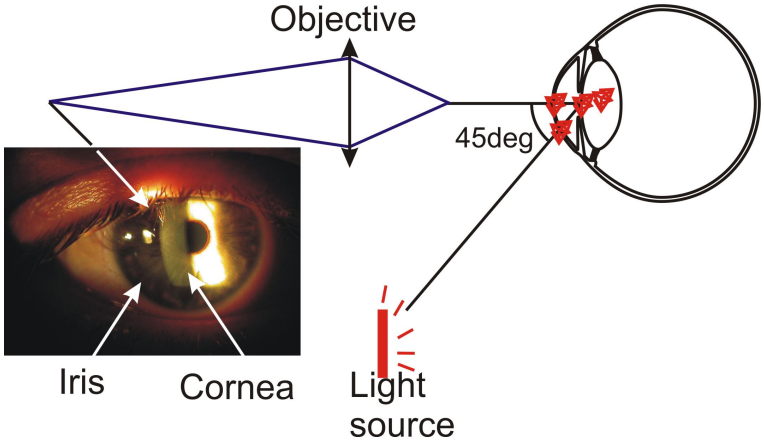

Figure 2.11: Principle of the haze exam

2.2.2 Backscattered and forward scattered light

Nowadays, corneal scattering is usually clinically associated with corneal haze. Haze is a subjective parameter assessed by a clinician when the cornea is examined under a slit lamp. The haze exam is illustrated by figure 2.11. A light source (generally it has the shape of a slit) is projected on the cornea under an incident angle of (commonly) 45 degrees. The clinician focusses the objective of the ophthalmoscope to the cornea until the hazy structure of the cornea is visible. According to the density of the hazy structure, a haze parameter between 0 (clear cornea) to 4 (severe haze) is given [18].

Apart from the subjective estimation for haze, which can vary from one clinician to the other, a major disadvantage of the method is that the assessed scattered light does not reach the retina and thus does not affect the image quality on the retina. When light gets scattered over an angle wider than 90 degrees with the incident beam, we say that the light is *backscattered*. Light which is backscattered, such as observed in a slit lamp (or other optical microscopes imaging the cornea) cannot reach the retina. Thus, it is appropriate to say that forward scattered light, reaching the retina, is more detrimental for the retinal image quality. A comparison between forward light scattering and corneal haze is discussed in more detail in chapter 7. The characterization of forward light scattering in the cornea is discussed throughout the rest of this thesis.

2.2.3 Scattering vs. optical aberrations

The inhomogeneities of refractive index characterizing light scattering in the lens and the cornea could be converted to the local optical path differences of a plane wave entering the scattering medium. This results in a distorted wave due to light scattering. From this point of view, there should be a clear relation between optical aberrations and ocular scattering. To some extend, we could indeed say that light scattering is a type of optical aberrations. Given the characteristic size of the scattering structures ranging from 0.5 to 35 μm [1], the spatial frequency of the wave distortions due to scattering are of two to four orders of magnitude higher than the spatial frequency of the distorted wave due to optical aberrations. For this reason, a precise description of light scattering by Fourier analysis of the scattered pupil function will require a very dense spatial sampling of the pupil function. A theoretical model characterizing light scattering by the local distortion of a plane wave is described in section 4.1.
When comparing the effect of light scattering on the lens and the cornea to the optical aberrations on the retinal image quality, one should remember two major differences:

Angular distribution

However the angular distribution of the scattering and the optical PSF can vary from subject to subject, we can say that scattered light has a much wider angular distribution on the retina than the light distribution from the optical PSF. Whereas the optical PSF of an aberrated eye will seldom exceed a with of 10min of arc, scattered light is usually assessed over angles wider than 30 minutes of arc [3].

Effect of pupil size

Given the small characteristic size of the scattering particles, we should consider light scattering as a *"local distortion"*, whereas the optical aberrations originate to a more *"global distortion"* of the pupil function. Provided that the scatterers are evenly distributed across the pupil, we can say that light scattering is a phenomenon which is

[1] Scattering structures with sizes of the order of the wavelength of the incident light have been identified with electron microscopy. Other microscopic techniques reveal also the presence larger scattering particles.

not affected by the pupil size, whereas the reduction of retinal image quality due to optical aberrations strongly depends on the pupil size.

2.3 Evaluation of the retinal image quality

As mentioned in section 2.1, an optical system is characterized by its PSF. Ideally, a point is imaged on an infinitely small dot on the image plane. The wave nature of light, ocular aberrations and light scattering in the eye reduce the image quality on the retina and cause a broadening of the PSF. A convenient method to evaluate the effect of each optical phenomenon on the retinal image quality is done by evaluating the Modulation Transfer Function (MTF). The MTF describes the contrast reduction of a sinusoidal grating with a specific spatial frequency imaged through the optical system. The MTF is also defined as the Fourier transformation of the PSF [23].
Generally, the contrast of a grating is defined as follows:

$$contrast = \frac{L_{max} - L_{min}}{L_{max} + L_{min}} \tag{2.3}$$

Where L_{max} and L_{min} are respectively the maximum and the minimum luminance of the grating. In a perfect optical system, the MTF is 1 for each spatial frequency. Given the asymmetry of the PSF in some optical systems, e.g. in an astigmatic eye, the MTF can depend on the orientation of the grating. Often a simplified one dimensional MTF is proposed as the radial average of the Fourier transform of the PSF.
Using the MTF for the evaluation of the retinal image quality, we can separate the effect of the different optical phenomena that were previously discussed. When evaluating the effect of diffraction, aberrations an scattering in the eye, we can calculate the MTF of the eye's optics as follows:

$$MTF(eye) = MTF(diffraction) \cdot MTF(aberrations) \cdot MTF(scattering) \tag{2.4}$$

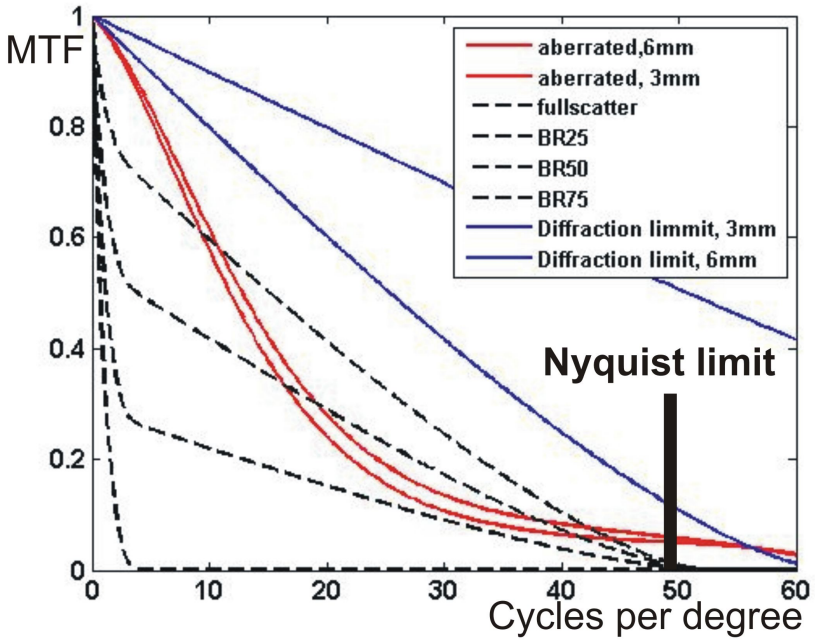

Figure 2.12: Modulation transfer function of the eye's optical system

Commonly, diffraction and aberrations are evaluated in the same MTF describing the wave propagation through the eye:

$$MTF(eye) = MTF(optics) \cdot MTF(scattering) \tag{2.5}$$

Figure 2.12 gives an overview of the MTFs affecting the retinal image quality. The blue lines represent image transfer in a diffraction limited system, i.e. in the absence of aberrations and scattering. The red lines describe the MTF of a normal eye (sphere corrected) in the presence of aberrations, but no ocular scattering. The dashed lines show the MTF of corneal scattering for different amount of scattering, as proposed in section 7.1.

2.4 Image sampling on the retina

As for most imaging systems, the optimal resolution in the eye is limited by the sampling density on the retina. The image of a scene on the retina is sampled by two types of photoreceptors: the rods (distributed over the entire retina) and the cones (which

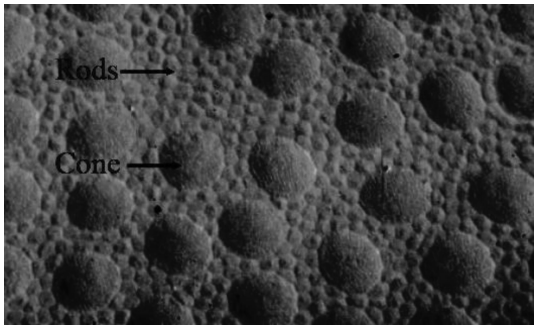

Figure 2.13: Scanning electron microscopy of the retina outside the fovea. The large structures are the cones, the small structures are rods (Curcio *et al.* [9]).

are only found in the fovea). There are three different types of cones with different spectral responses allowing us to distinguish the colors in a scene. Figure 2.13 shows an image of the retina outside the fovea. However the most accurate sampling can be done by the rods (since they are much smaller), the retinal resolution is commonly associated with the cone sampling in the fovea [64]. The fovea is the region of the retina around the visual axis, i.e. it corresponds to the central 5 degrees of our visual field. The spacing between the cones in the fovea is of the order of $3\mu m$, which corresponds to a visual angle of approximately 0.6 minutes of arc [64]. According to the Nyquist sampling theorem, this gives us an absolute limit of the visual resolution to be of approximately 50 cycles per degree (CPD). Coming back on the MTF of the eye, the Nyquist sampling limit of the retina is drawn in figure 2.12. Regarding the retinal image quality, we can conclude that the eye's optics are optimized for the retinal sampling density.

2.5 Excimer laser treatments for the correction of the refractive error

The aim of refractive surgery is to permanently correct the refractive error of the eye by modifying the corneal curvature. For myopes, the cornea is *flattened*, whereas in hypermetropes the corneal curvature is increased to correct the refractive error. At present, most refractive treatments are based on laser ablation to permanently remove a portion of the corneal stroma. In this section, we give a brief overview of the

most common refractive treatments based on laser ablation. A deeper description of refractive laser treatments can be found in the literature [21].

2.5.1 Basics of refractive surgery

The cornea of the human eye consists of three fundamental layers (The corneal morphology is described in more detail by chapter 3):

The epithelium has a thickness of approximately $50\mu m$, consists of a auto recovering tissue and can be seen as a layer that "polishes" the corneal surface. Small scratches due to injuries are recovered in a time interval of approximately 12 hours after the injury. The epithelial cells regenerate about every 14 days [53].

The stroma is a $500\mu m$ thick layer under the epithelium, mainly consisting of collagen layers. This is the layer on which the laser is targeting for changing the corneal topography in refractive surgery. However cellular structures (keratocytes) are present in the stroma to recover stromal injuries, laser ablation of the stroma will result in a permanent change of the corneal topography.

The endothelium is the last layer of the cornea. It consists of a monocellular layer that controls the hydration of the cornea. This layer is not regenerative and therefore, endothelial cell death can lead to a malfunction of the corneal hydration mechanism.

Laser-tissue interaction

After epithelial removal, laser ablation on the stroma is done by a controlled UV irradiation on the corneal stroma. Common laser systems are excimer lasers (Ar:F), radiating at a wavelength of 193nm or a solid state (Nd:YAG), which radiates at a wavelength of 1064nm, from which the fifth harmonic wavelength is selected after the light travels though a non-linear crystal, resulting in a radiation of 213.2nm. The radiation on the cornea is delivered in short pulses, with a repetition rate of 100 to 400Hz. An optical system focusses the light on the cornea on a 1mm spot. A scanning

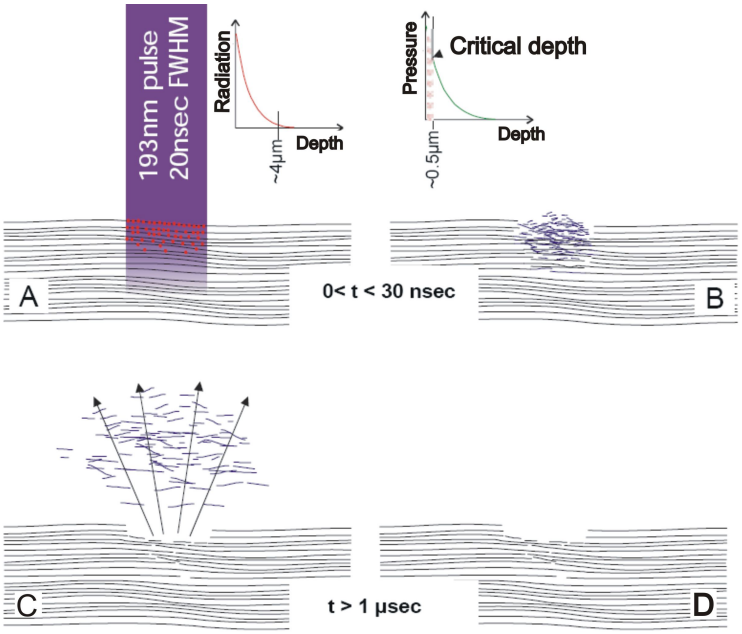

Figure 2.14: Response of the collagen tissue during laser ablation

Figure 2.15: Explosion of collagen tissue of a hair after laser ablation

system in the laser is programmed to deliver the laser pulses in a specific pattern on the cornea in order to achieve its desired curvature.

A major benefit of laser ablation on the cornea is the high accuracy of the amount of stromal tissue that is removed by the laser irradiation. A pulse with duration of approximately 30ns, delivers an energy fluency of $180mJ/cm^2$ on a 1mm spot on the cornea. A schematic of the collagen response during laser ablation is illustrated in figure 2.14.

The high pressure caused by this fluency creates a local breakup of collagen fibers on the stroma. To illustrate the amount of energy delivered in one pulse, figure 2.15 gives an image of the instantaneous response of the collagen after laser irradiation on a hair.

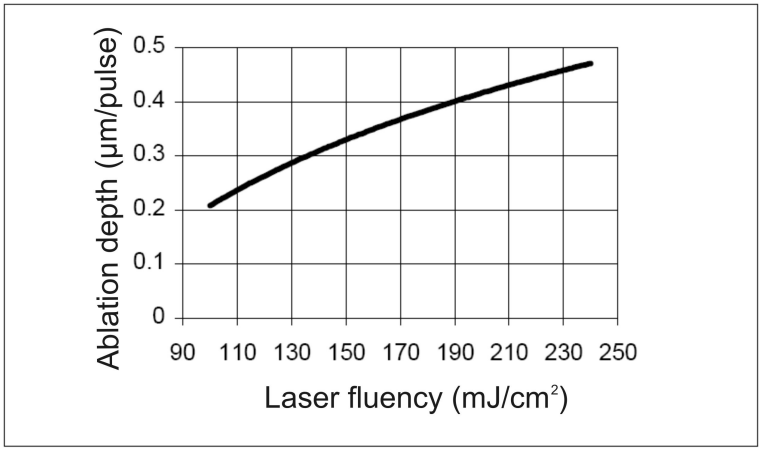

0

Figure 2.16: Collagen tissue removal per pulse (Seiler *et al.* [49])

The amount of collagen tissue removed in one pulse depends on the fluency of the laser. The relation between the laser fluency and the ablation depth is shown in figure 2.16.

Ablation patterns

Refractive surgery is performed with laser treatments for the correction of myopic eyes up to 10 diopters, and for hyperopic eyes for the correction up to 4 diopters [41]. The difference between both treatments is illustrated in figure 2.17. For the correction of myopia, more tissue is removed in the center of the cornea, and the corneal thickness in the periphery is changed little. In this way, the cornea is "flattened" in order to move the focal point deeper towards the retina. For the correction of hypermetropia on the other hand, the corneal curvature should be reduced to shift the focal point to the retina. Therefore, more tissue needs to be removed in the periphery of the cornea. This leads to a discontinuity in the attempted corneal topography. This discontinuity is smoothened by the epithelial layer. In order not to affect the pupil function, it needs to be enough in the periphery of the cornea, resulting in the ablation of more corneal tissue.

The higher the attempted correction, the more tissue should be ablated. Attempting a high reduction of the central corneal thickness (CCT) can result in mechanical

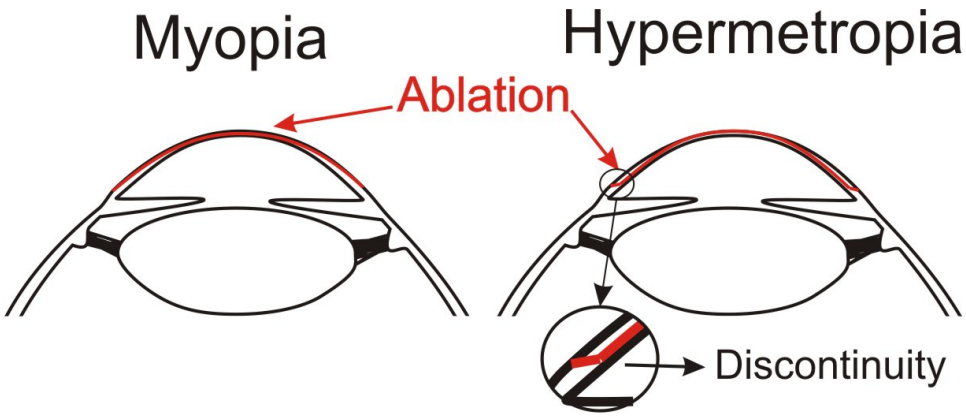

Figure 2.17: Different ablation patterns for the correction of myopia (left) and hypermetropia (right)

inconsistency of the cornea, yieding to mechanical deformations or, in the extreme case, corneal ectasia, a degeneration of the corneal tissue.

A second parameter that affects the change of CCT is the size of the ablated surface, also called the *optical zone*. When restricting the laser treatment over a small area (figure 2.18 right), only a small portion of the central corneal thickness will be removed in order to attempt the same correction. When reducing the optical zone however, the limited factor is given by the pupil size. When, in a scotopic (dark) environment, the pupil size increases and, when it exceeds the optical zone of the laser treatment, this

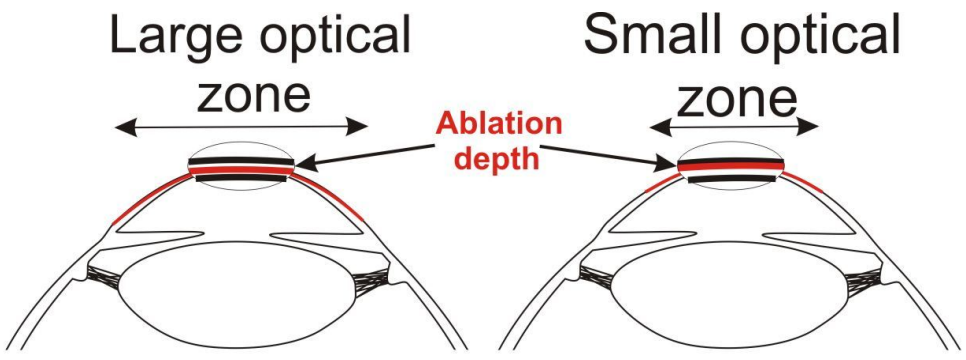

Figure 2.18: Ablation depth for different optical zone

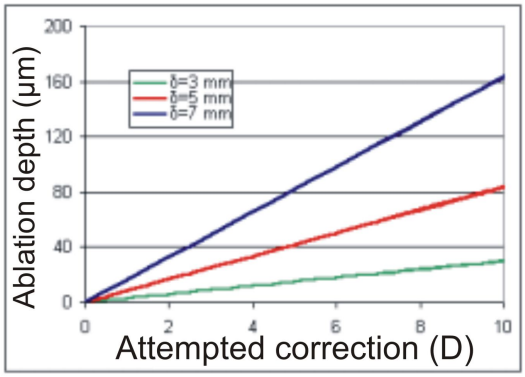

Figure 2.19: Central ablation depth for the correction of myopia with different optical zones (Munnerlyn *et al.* [38])

will lead to a significant reduction of the retinal image quality. For the correction of low to moderate myopia, an optical zone of 6-7 mm is attempted, which usually corresponds to the scotopic pupil diameter. A chart showing the amount of collagen tissue removed for different myopic corrections and different optical zones is given in figure 2.19.

Reduction of the peripheral image quality

As discussed in the previous paragraph, the retinal image quality is reduced after refractive treatments when the pupil size exceeds the optical ablation zone. Around this zone, there is a *transition zone*, an area where the corneal curvature flows from its natural, uncorrected curvature to the newly formed, treated curvature. This transition zone will not only affect the retinal image quality when the pupil is larger than the optical zone, but also the image quality of the peripheral light can be affected by the transition zone [7]. The effect is illustrated in figure 2.20.

2.5.2 Refractive treatments

In the past 2-3 decades, several refractive procedures have been developed for the laser guided removal of collagen fibers in the stroma. The procedures are generally characterized by the method of epithelial removal. Below we give a brief description of the most common procedures that are currently applied in refractive surgery.

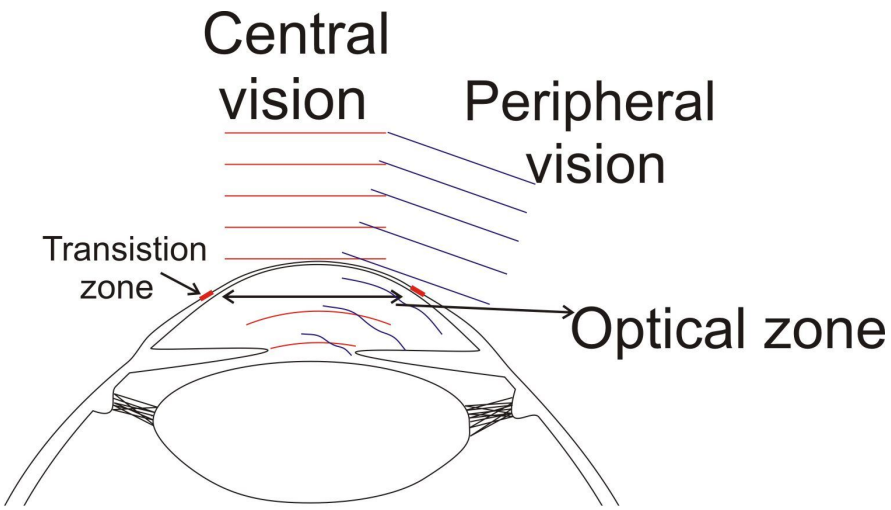

Figure 2.20: Peripheral light propagation after refractive surgery

Photorefractive Keratectomy (PRK)

Photorefractive Keratectomy [41] is the oldest refractive procedure. The epithelium is mechanically removed by means of a brush. Consequently, the ablated surface is the subepithelial stroma. Since the ablated surface is exposed to the environment, a significant drawback of this technique is that a more severe wound healing response can lead to corneal haze development. To reduce the exposure of the cornea to the environment, a contact lens is applied on the cornea after the treatment until the epithelial layer has regenerated its structure over the ablated surface (usually from 5 to 7 days).

Laser In Situ Keratomileusis (LASIK)

LASIK is a technique introduced by Pallikaris et al in 1989 [43] and is currently the most common procedure for the correction of myopia worldwide. In this procedure, a corneal flap is created to expose the stroma to the laser irradiation. The flap can be created either mechanically, by means of a microkeratome, or laser guided, where a femtosecond laser creates the flap [20]. Depending on the used keratome, flap thickness can vary from $70\mu m$ to $150\mu m$. Since the ablated stromal surface is intrastromal, and the flap is replaced on its original position after treatment, the epithelial layer remains intact and the ablated surface is not exposed to the environment. This results in a

very moderate healing response, low haze development and few regression. The main drawback of this method is that the flap does not fully attaches to its original fibers and brings a permanent reduction of mechanical strength of the cornea.

LASEK

LASEK is a method which is very similar to PRK. The epithelium is separated from the stroma chemically with an alcohol solution applied on the cornea before treatment [42]. After treatment, the (dead) separated epithelial cells are replaced on the ablated surface before applying the contact lens. This is done to reduce the effect of the wound healing response that gives rise to haze development and regression.

epiLASIK

epiLASIK has been introduced by Pallikaris et al in 2003 [42] [40] as a compromise between the traditional LASIK and PRK. During epiLASIK, a blunt keratome separates the epithelial layer from the stroma, so the flap consists only of epithelial cells. After laser treatment, the epithelial flap is restored on the ablated surface. Since the epithelial cells survive for some time after treatment, a contact lens is applied on the cornea until a new epithelial layer is composed.

2.5.3 Accuracy of refractive surgery

Low order aberrations (sphere and astigmatism)

Currently available laser systems are capable to correct the low order refractive errors. Figure 2.21 shows a chart of refractive outcomes after laser treatment. The variation between attempted and achieved correction has various reasons, mainly addressed to the biologic nature of the corneal tissue. Several parameters such as corneal thickness, IOP, corneal hydration level and other physical parameters affect a very little amount the amount of collagen ablation per pulse, resulting in visible variations between attempted and achieved correction of the refractive error. However it is almost impossible to characterize the effect of these parameters on the achieved ablation, sev-

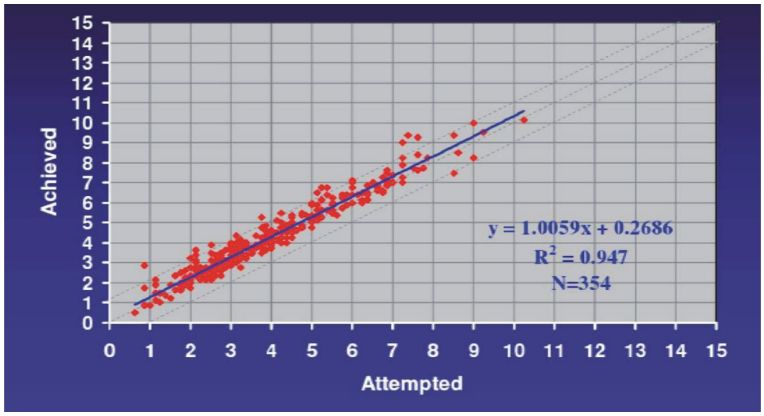

Figure 2.21: Attempted versus achieved correction of refractive error

eral algorithms are developed to optimize the relation between attempted and achieved refraction as a function of the physical parameters during the treatment. These algorithms result in a nomogram, which is an optimized table that gives the best correction a laser system should be programmed to achieve an accurate result of refractive outcome. These algorithms are based on data mining, such as neural networks and tend to be more efficient when more data between attempted and achieved correction are available. The nomogram is a *"self training"* algorithm and is dependent on each laser system. Using this nomogram, the correction of lower order aberrations for a specific laser system gets more accurate when a larger patient database of the system is available.

Chapter 3

Corneal Morphology

Rather than questioning why the cornea is not perfectly transparent, it is noteworthy that the cornea has a surprisingly high degree of transparency. However the cornea consists of cells and connective tissue, that contains inhomogeneities on a scale ranging of the order of the wavelength of visible light to 40microns, they appear to be much more transparent than other cells in the body such as those in the skin which strongly scatter light. We need to understand why the normal cornea has such a high transparency.

This chapter gives a brief overview of the morphologic structure of the cornea and the changes of the corneal structure associated with laser treatments for refractive surgery. In particular, the main structures that are believed to be responsible for corneal light scattering will be highlighted. For a detailed description of corneal morphology and associated pathologies, we refer to more detailed sources [31].

3.1 Corneal structure

This section describes the main corneal structures, shown in figure 3.1 .

3.1.1 Tear film ($\pm 10\mu m$)

Even though the tear film is the thinnest layer of the cornea, without it the retinal image quality would dramatically decrease. The tear film consists of an anterior lipid layer, a central aqueous layer and, on the interface with the epithelium, a mucin layer. It can be seen as a *lubricating* layer that has the goal to control the corneal constitution,

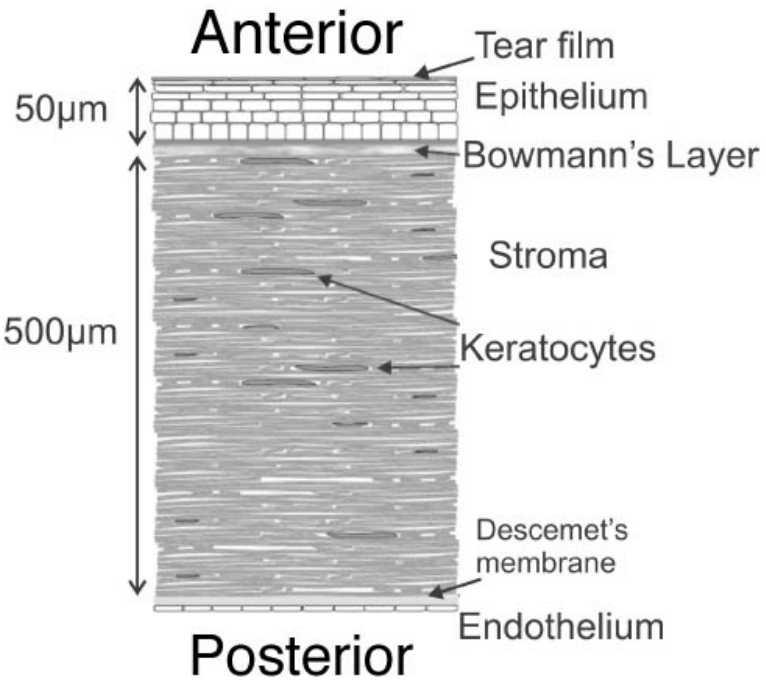

Figure 3.1: Schematic drawing of the human corneal structure.

clean epithelial debris and to smoothen the anterior surface of the eye. Indeed, given the refractive power of the cornea (40D), slight surface roughnesses on the cornea could give rise to a dramatic distortion of the wavefront.

3.1.2 Epithelium($\pm 50\mu m$)

The epithelium is a 50 microns thick layer of fast regenerating cells, the cycle of an epithelial cell is of approximately 14 days. The function of the epithelium is to protect the stroma from external injuries. When the epithelium gets scratched, the cells regenerate the epithelial layer back to its original morphology in a time interval of 6-12 hours (depending on severity of the scratch). When the injury causes roughnesses in the stromal layer, as in laser surface treatments (section 2.5), the epithelium will act as a filter to smoothen out the stromal roughnesses. The slight refractive index transition on these surface irregularities can be responsible of a (minor) source of increased light scattering after refractive surgery (the so-called *corneal cracks*). Figure 3.2 gives a set of representative in vivo confocal images of epithelial cells.

Bowman's Layer

The Bowman's layer is a thin acellular layer consisting of collagen fibers on the interface between the epithelium and the stroma. As this layer is only present in the cornea of few vertebrates. Little is known about its function. Moreover, this layer is removed during several refractive treatments (PRK, epiLASIK and LASEK)

3.1.3 Stroma ($\pm 500 \mu m$)

Most light scattering originates from the stroma because it occupies 90 percent of the corneal thickness. Basically, the stroma consists of well organized collagen fibrils stacked in a specific way to optimize the corneal transparency [24]. As it is the main structure in the cornea, it is advisable to distinguish between two stromal areas:

Anterior stroma

Below the epithelium, the *subepithelial stroma* contains a nerve layer. Also cellular structures in the shape of thin disks of approximately 10-20 microns an be observed (figure 3.1 and figure 3.2 right). They are keratocytes and are inactive in a healthy cornea. They activate when the stroma gets damaged by an injury. Activated keratocytes, also called fibroblasts, tend to repair the stroma by the formation of new collagen tissue substituting the damaged area. This wound healing response is discussed in more detail in section 3.2.

Posterior stroma

As seen in figure 3.2, the confocal image show larger keratocytes in the posterior stroma, but they seem to be less densely concentrated.

3.1.4 Endothelium ($\pm 20 \mu m$)

The last surface of the cornea is the endothelium (see figure 3.2). It is a monocellular layer separating the stroma from the aqueous humor. More than a physical barrier, the

endothelium serves as a pump to control the hydration level of the cornea. Endothelial cell damage can therefore result in irregular corneal thickness, not only reducing its mechanical strenght, but also causing a significantly distorting the wavefront of the incoming light.

Descemet's Membrane

The Descemet's membrane is a 10 microns thick membrane secreted by the endothelium between the stroma and the endotelium

3.2 The cornea after refractive surgery

3.2.1 Morphology

As mentioned, the aim of refractive surgery is to permanently correct the refractive error of the eye by laser ablation of stromal tissue. This tissue is either ablated intrastromal (LASIK), at a depth of approximately 100 microns or subepithelial (PRK, epiLASIK and LASEK). As the epithelial layer remains intact during LASIK, it is reasonable to conclude that the wound healing response is more moderate in intrastromal treatments. The created interface (consisting of disrupted collagen fibers) will mildly reconnect without an overwhelming activation of keratocytes. For this reason, LASIK is supposed to be the most safe technique in refractive surgery in the scope of development of increased corneal scattering. On the other hand, the remaining pseudo-instability of the flap interface reduces the mechanical properties of the treated cornea.

During subepithelial treatments on the other hand, the stroma is exposed during an extended amount of time to abnormal structures (either contact lens or dead cellular tissue). Consequently, we can hypothesize that the more severe wound healing response of these techniques make the cornea more sensitive to a risk of increased corneal light scattering. Figure 3.2 gives a chart of the representative structures in the cornea before and after refractive surgery. In the next paragraph, we discuss the morphologic changes of the cornea over time corresponding to the corneal wound healing response.

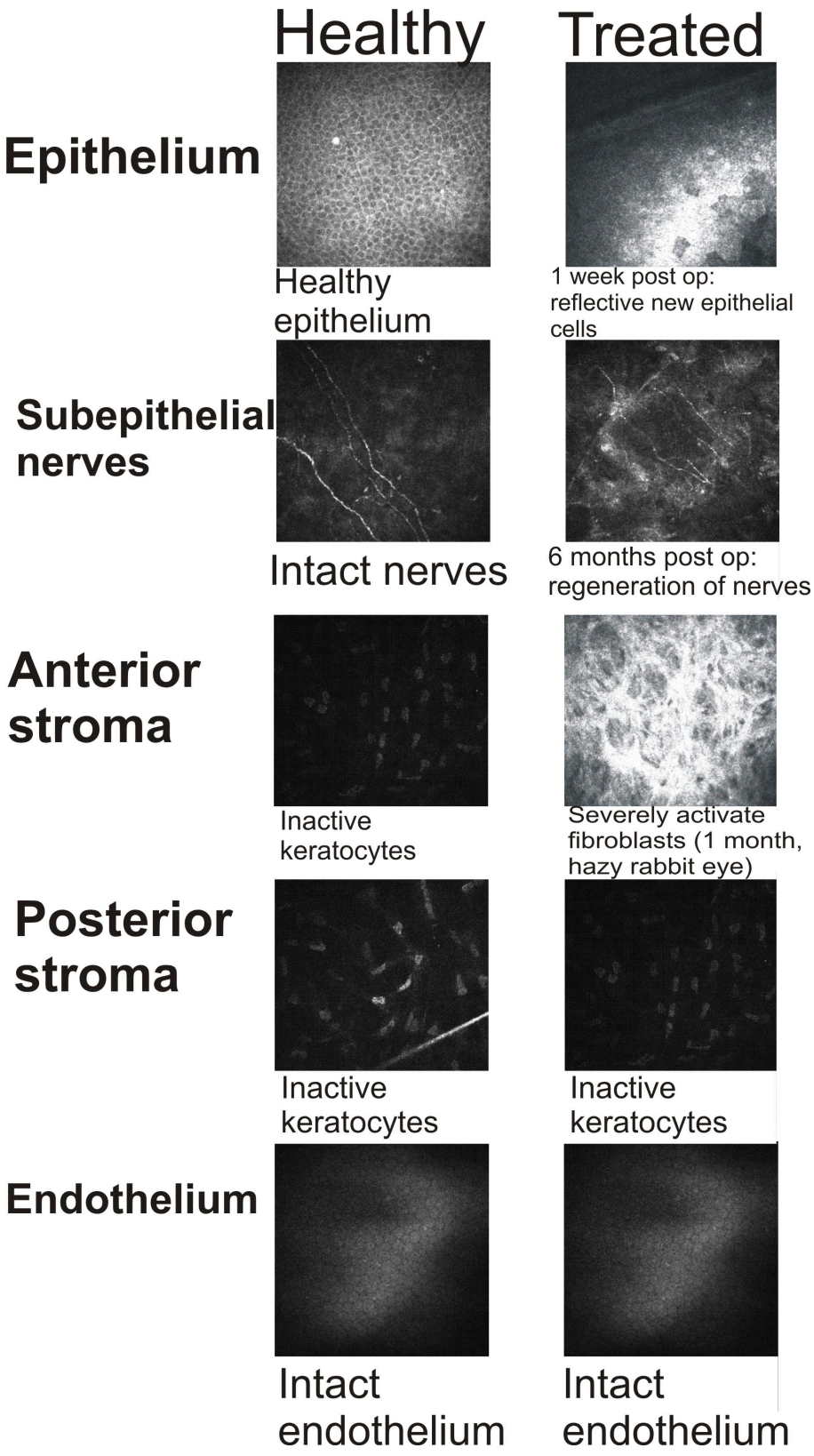

Figure 3.2: Representative images of the different corneal layers before (left) and after (right) refractive surgery as seen in in vivo confocal microscopy.

3.2.2 Postoperative corneal follow-up

The immediate response of laser ablation on the stromal tissue was earlier discussed in section 3.2. In this section, we highlight the response of the cornea in a long term follow up after refractive treatment.

Immediate response: corneal edema and epithelial regrowth

In the first days after laser treatment, the ablated area is occupied by *water lakes*, also called edema due containing a portion of the ablated collagen that was not secreted immediately after treatment. The water is occupying spaces between the collagen layers and is excreted a few days after treatment.
Moreover, after surface ablations as PRK, LASEK and epiLASIK, the removed epithelium regrows back from the periphery (where the epithelium remained intact) to the center covering back the entire cornea after 5-7days.

1 month postoperatively: Activation of keratocytes

Whereas during the laser treatment also keratocytes were ablated, the keratocyte density in the treated area reduces the first week after treatment, but as a wound healing response, the cells in the non treated stroma migrate towards the *injury*, and reach a maximum density one month after treatment. According to the the severity of the inhibited injury, keratocytes will activate to fibroblasts producing new collagen in an attempt to replace the destroyed fibers. The new collagen is a form of *scar tissue* and often called the *foam layer* and described below.

3 months and later: remanent scar tissue

After approximately 3 months, the keratocytes stop producing scar tissue and return to their inactive state [36].

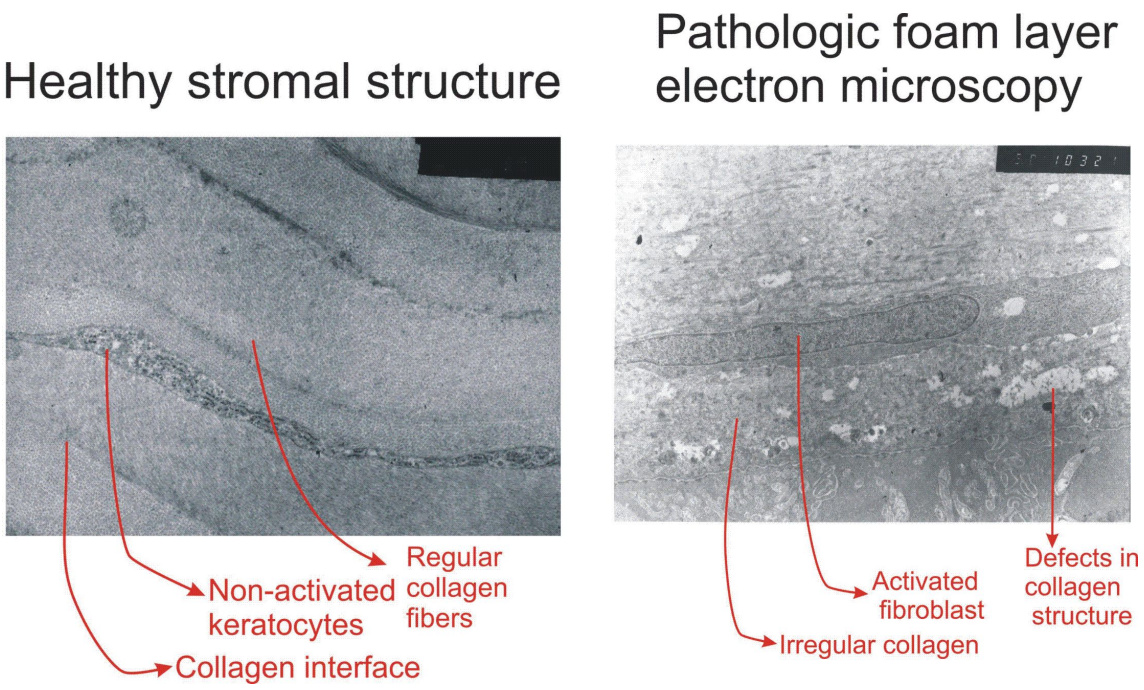

Figure 3.3: Electron microscopy of healthy original collagen (left) and scar tissue (right) as observed in scanning electron microscopy (FOV: 40x40μm)

3.2.3 Corneal scar tissue

As the laser treatment is a controlled technique for the removal of the stromal collagen, regeneration of the collagen previously mentioned as scar tissue is a side effect we want to reduce. Not only the regeneration of new collagen will increase the optical path of the light traveling through the cornea, resulting in induced optical aberration. But also, the newly formed scar tissue does not have the same order organization as the original collagen layers. Figure 3.3 has two electron microscope scans illustrating the difference between the original collagen and scar tissue under a high magnification. The white vacuoles present in the scar tissue correspond to defects in the collagen representing a severe form of foam layer. Around the fibroblasts, we observe the unorganized collagen fibers. The scar tissue can also be observed in optical microscopy of stained corneas as a darker area in the stromal tissue. Representative images of this scar tissue in rabbit corneas are shown in figure 7.6. Correlation between the thickness of this foam layer and single pass forward scattering, as described in chapter 7 suggests that this layer could play a key role in the increased corneal scattering addressed to refractive surgery. Moreover, as the foam layer can be distinguished as a highly reflective layer in in vivo

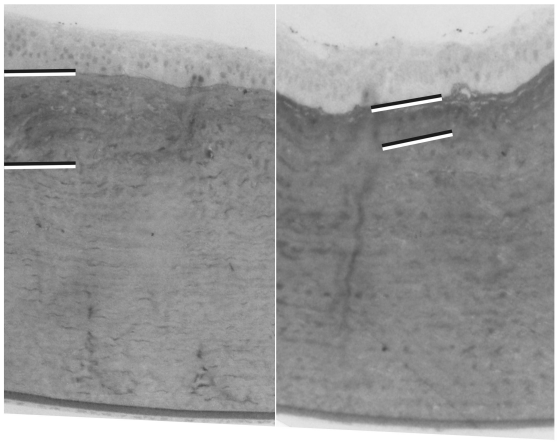

Figure 3.4: Scar tissue after refractive surgery

confocal microscopy, the variations of the refractive index of the scar tissue cause local distortions on the wavefront of the incoming light. These wavefront variations are translated into a theoretic model described in chapter 4.

3.3 Drug treatments to control corneal wound healing

As we suggested in the previous section, a goal of the post operative drug treatment is to control the corneal wound healing response, specifically the activation of keratocytes. The precise mechanisms of these drugs are the scope of a new generation of pharmaceutics developed that exceeds the extent of this thesis. However, given its effect on corneal scattering following refractive treatments, we will briefly discuss the most common drug protocols currently used in the follow-up of refractive surgery.

3.3.1 Post operative drug treatment: Anti-inflammatory Corticoids and steroids

The use of corticoids is a standard treatment to prevent inflammation after the corneal injury. They are delivered on the cornea in the form of eye drops or ointments.

3.3.2 Intraoperative drug treatment: Mitomycin C (MMC)

Mitomycin belongs to a group of medicines called cytotoxic antibiotics, it both inhibits cell dead and blocks the cell functioning. Lately, MMC has been used intraoperatively after PRK [56]. The MMC is generally delivered on a sponge in a small concentration (0.02%) during a short time interval (5-30 seconds) on the cornea, depending on the attempted correction. The penetration of MMC will cause cell apoptosis of the keratocytes, thus preventing them from activation and formation of scar tissue. Despite the inhibition of haze formation by MMC's cytostatic action, several concerns regarding its adverse effects on different ocular tissues and its long term safety have been raised [14].

Chapter 4

Theoretical Models of Corneal Light Scatter

Light scattering in the cornea originates on irregularities of the refractive index of the tissue. When a light ray passes these "optical irregularities", it will further propagate on an optical path different from its refractive path. The scattering phenomenon is due to the light-tissue interaction, and thus depends on both the properties of the incoming light and the scattering tissue. Besides scattered light intensity, a major characteristic of light scattering affecting the retinal image quality is the angular scattering distribution. This distribution defines the light distribution over a solid angle $d\Omega$ of the light scattered through a scattering surface.

For an exact description of the scattering distribution in the cornea, we would need very precise information on values of refractive indices of the smallest particles present in the cornea, their dimension and relative positions. Also the spectrum and coherence of the incoming light is a parameter that would affect the scattering function. Thereafter, one might be more interested on a general theoretical model describing the light scattering in the cornea. In this paragraph, we will present three models based on 3 different approaches.

4.1 Wavefront analysis

In a first approach, we study the wave propagation of a plane wave traveling through a scattering medium. In chapter 2, we discussed the retinal image formation based on Fourier optics. Image degradation was a result of high or low order optical aberrations.

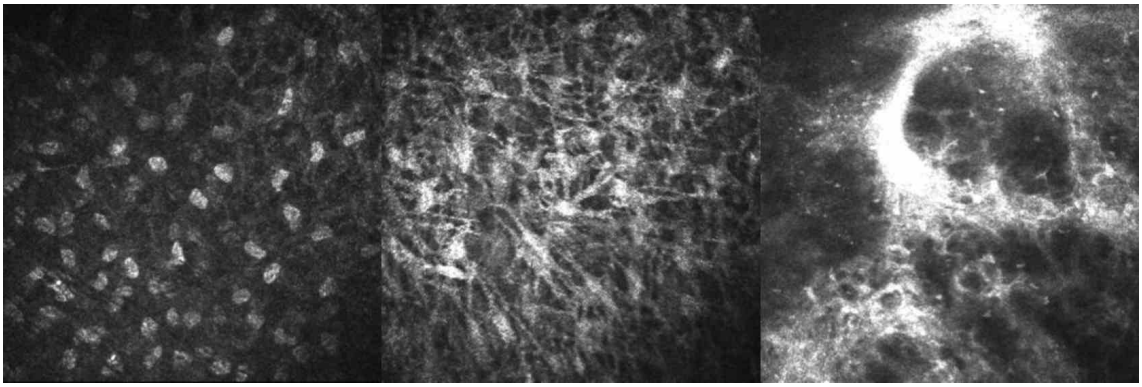

Figure 4.1: Confocal images of the subepithelial stroma of a healthy (left), post PRK (center) and hazy (right) cornea. Field of view=$400x400\mu m$

These aberrations were addressed to the deformation of the ocular optical surfaces in respect to the diffraction limited configuration. This deformation has generally a low spatial frequency and can be measured by double pass ray tracing techniques. Now if we see the scattering sources in the cornea as small perturbations of the optical media, the wavefront will undergo small local aberrations, it can be easier understood as an additional "noise" on the wavefront, additional to the aberrations of the eye's optics. The amplitude of the wave perturbation is defined by the optical path difference (OPD) caused by the scattering source. Its spatial frequency is inherent to the size of the local scatterer. An appropriate method to estimate the OPD addressed to these scattering sources is the analysis of corneal confocal images. Indeed, the contrast in confocal images is defined by variations of refractive index of the imaged structures. A set of typical confocal images (HRTII, Rostock corneal module) of healthy and haze corneas is displayed in figure 4.1. These structures, as described in the previous chapter, are more dense in the subepithelial stroma, though present all over the stroma. S ince the wave perturbation is an additive function over the entire corneal (and crystalline) thickness, it is appropriate to generate a set of simulated images representing a *corneal OPD map* addressed to the scattering structures.

There are various methods to generate an OPD map, though given the biologic nature of the present structures, we selected an algorithm creating a fractal OPD map of 10 iterations. The size distribution of the present structures can be manipulated by a weighting function in the fractal algorithm. Figure 4.2 shows three OPD maps where

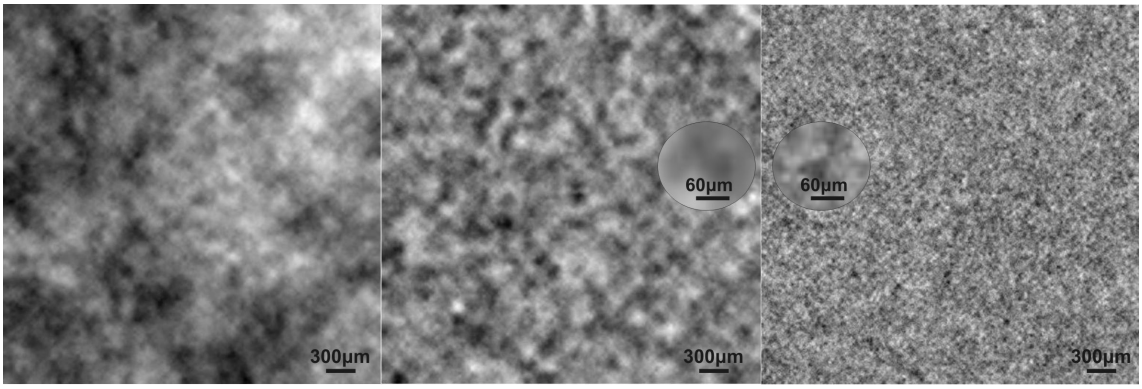

Figure 4.2: Fractal OPD simulating the corneal scattering structures. Left: large structures, Center: moderate structures, Right: small structures.

the generic particle size is controlled by different weighting functions. The fractal OPD maps are calculated to cover a 3mm pupil diameter. To simulate fine structures over the entire pupil function, the OPD maps are calculated in 1024 by 1024 pixels images. This restricts us on simulating particles smaller than $3\mu m$. Given the resolution of the confocal microscope ($1\mu m$), we have no information on the scattering properties of particles smaller than $1\mu m$. Nevertheless, the low noise level of confocal images suggests that the contribution of very small particles on the corneal scattering function is small. A second important parameter that will control the scattering distribution of the wavefront is the amplitude of the OPD map. It defines the phase lag of the plane wave traveling through the scattering particles in the cornea. Since we have not made a calibration of the corneal confocal microscope, we simulate a set of PSFs with various amplitudes in order to match with the experimentally obtained scattering distribution (see chapter 7). For each of the above OPD maps, in figure 4.3, the corresponding scattering PSF is calculated for a phase perturbation amplitude of $1\mu m$, calculated for a wavelength of 660nm. The noise periphery around the image center has a close similarity with the speckle pattern observed in the Tscherning images (further described in chapter 7) imaged with a 660nm diode laser source. Since the scattering sources in most of the natural scenes (see chapter 8) are polychromatic (white light), one could be interested on the polychromatic scattering distribution addressed to the above calculated OPD maps. We summed the (monochromatic) scattering PSF of 12 wavelengths covering the visible spectrum. A typical image is illustrated in figure 4.3. We see fine needles originating from the center, attenuating towards the periphery of

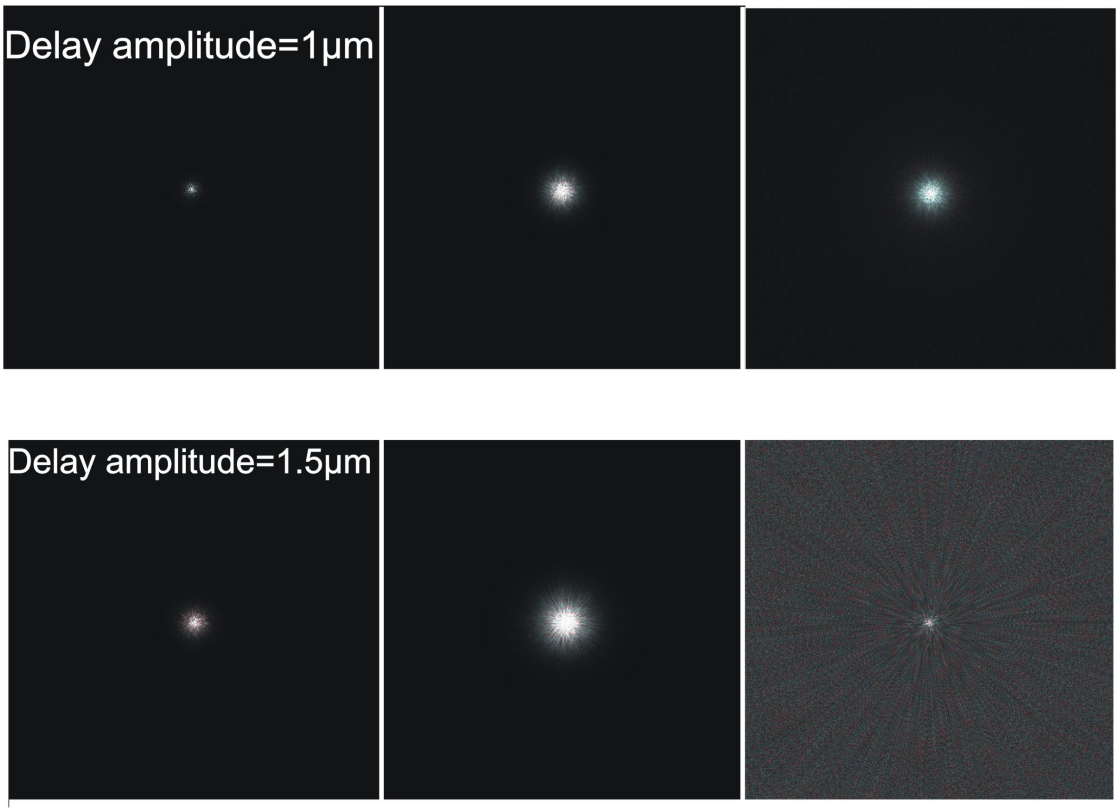

Figure 4.3: PSF of scattering light distribution obtained by wavefront propagation. FOV=7 by 7 degrees. The upper images have a wavefront distortion of $1\mu m$, the lower have a distortion of $1.5\mu m$.Left: large structures, Center: moderate structures, Right: small structures.

the image. The image is similar to the mathematical model of van den Berg et al [61], and described in more detail in section 4.3.1. The halo around the center is called the ciliary corona, and has a close similarity with the halo observed around a glare source in a natural scene.

Given the close similarity between the theoretical model and the glare naturally seen by an observer, we believe that this model is a valid approximation for the description of the corneal scattering function. Moreover, given the relation between the OPD maps and the confocal images of the cornea, we believe this method could result in an accurate model for the simulation of corneal scattering addressed to refractive surgery. Fitting of the model to experimental data would require that the amplitude of the phase perturbation and the spatial frequencies present in the fractal structure are appropriately adjusted.

4.2 Diffraction theory

The main part of the cornea consists of collagen fibers. They are well arranged structures stacked in layers with a regularly spacing and a certain orientation. Hart and Farrell described this regularly packing as a diffraction grating [24]. They modeled small cylindrical structures with size and orientation comparable to the fibers observed in the cornea. In conclusion, they observed destructive interference of the light in all directions except in the direction of the incident light. The regularly packed fibers are not the only structures observed in the cornea though. Cellular structures such as keratocytes and nerve fibers occupy spaces between the collagen layers as observed in confocal microscopy. Moreover, in addition to the organized collagen layers, transmission electron microscopy shows additional, unorganized collagen structures [8] [34]. Especially during wound healing [35], activated fibroblasts form this unorganized collagen, in this case called scar tissue. In their model, they took these imperfections into consideration and concluded that these structures are the cause of residual scattering. In this way, they achieved a point spread function comparable to the experimental measures of corneal scattering [24].

On the other hand, experiments described by chapter 5 have been conducted in a ma-

trix of unorganized collagen fibers. In the absence of the scattering microspheres, we did not observe significant light scattering in the samples, indicating that the scattering addressed to irregular collagen structures has a low contribution to the corneal light scattering compared to the scattering occurring on the keratocytes and scar tissue (see chapter 3).

4.3 Light scattering by small particles

Both models above mentioned might give us a clear qualitative idea for the optical origin of light scattering in the cornea, they are very sensitive to small variations of parameters. This makes it difficult to implement into a robust computer simulation. This paragraph presents two models based on scattering on small particles. Although the cornea does not consist of well defined particles, the theory of particle scattering is well described in the literature, giving us a tool to characterize corneal scatter with few, but physically relevant parameters. The first model has been implemented by van den Berg [61], the second model is a more basic approach allowing us to characterize scattering with just a few fundamental formulae. This model is the basic model on which calculations are based for the rest of this manuscript.

4.3.1 Coherent model

The idea of simulating the coherent wave propagation through a scattering medium was first described by van den Berg et al [61]. The light scattering was simulated by the interference of the light traveling through particles in the pupil. In this way, the interference on 1000 diffractive particles was simulated. The scope of their study was the simulation of scattering on the crystalline lens, the simulated particles had a $0.7\mu m$ diameter, corresponding to the protein aggregates observed in cataracts [60] [62]. A polychromatic simulation of their model resulted in an PSF illustrated in figure 4.4. We see a close similarity of the image with the polychromatic images simulated in the previous section, in particular with the small particle fractal OPD maps.

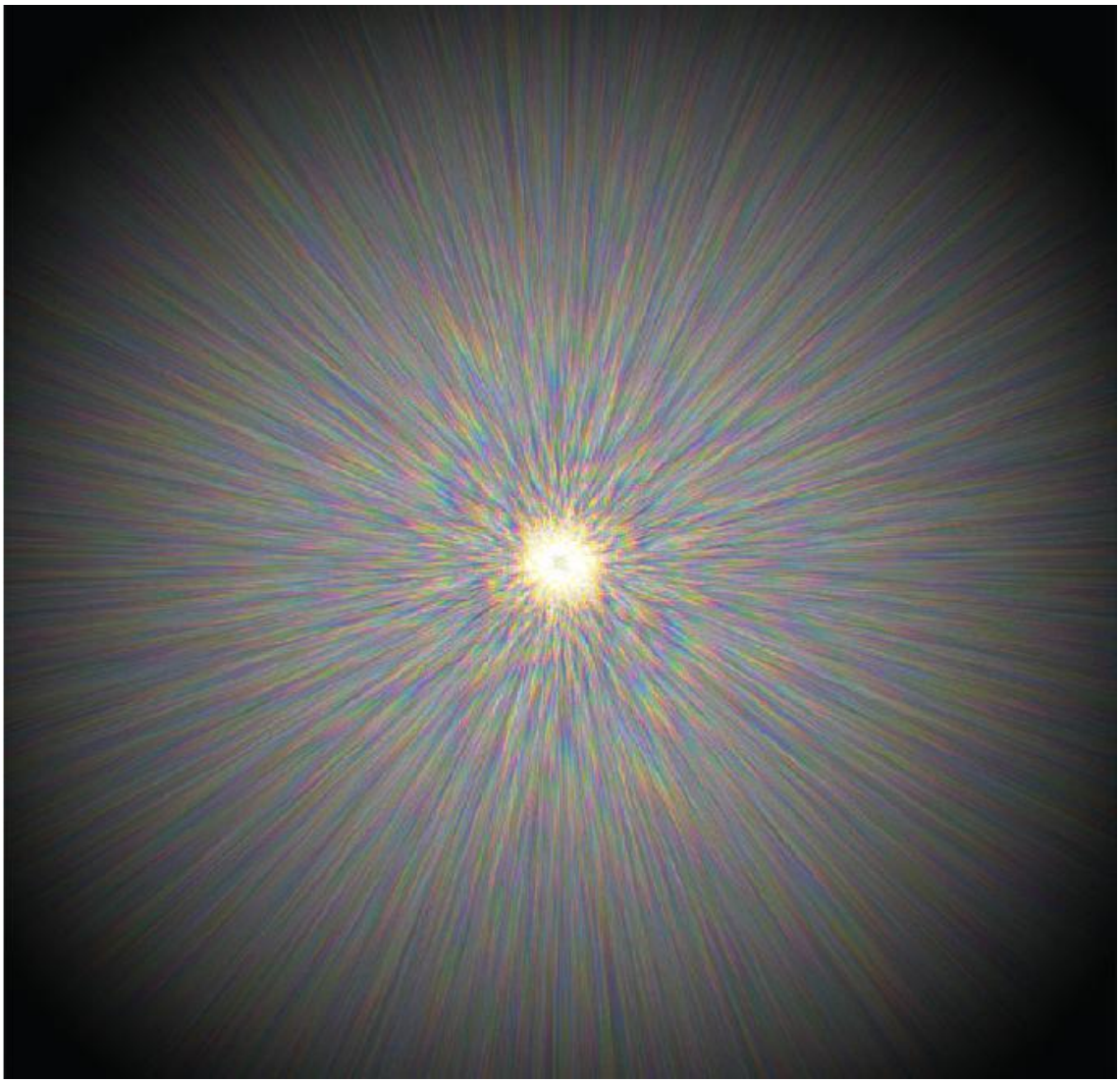

Figure 4.4: The ciliary corona. Polychromatic simulation of interference on spherical particles in the pupil.(van den Berg [61])

4.3.2 Non coherent model

Examining the stromal layer in in vivo confocal microscopy, the main reflective structures observed are keratocytes [36]. They are disk-like objects having dimensions starting from $6-8\mu m$, mainly in the anterior stroma, increasing to $15-20\mu m$ in the posterior stromal slices. The difference in reflectance between anterior and posterior keratocytes could suggest different refractive indices of the cellular structures. In conditions of corneal wounding, activated fibroblasts and newly formed collagen appear as larger, highly reflective layers.
The cells appear to form an interconnection resulting in structures that are difficult to distinguish, though characteristic sizes upto $50\mu m$ can be observed. Structures smaller than $1\mu m$ were not resolved by the resolution of the confocal microscope. In vitro microscopic techniques (light microscopy and transverse electron microscopy) reveal that irregular structures with dimensions smaller than $1\mu m$ consist of collagen fiber irregularities and intracellular structures. These sources of scattering are not taken into account in the following discussion. However, they can give rise to a source of additional (wide angle) light scattering in the cornea.

Light scattering on particles much larger than the wavelength of the incident light has been described very precisely in the literature by van de Hulst [57], the following discussion is a brief overview of the theory, focussed to the conditions appropriate to the particles observed in the cornea. We refer to the literature for a more detailed description.

Single particle light scattering

When the scattering particle has dimensions of an order bigger than the wavelength of the incoming beam, we can consider a bundle of light rays passing the scattering medium and describe the refraction and diffraction phenomena around the particle.

Refraction

Light rays entering the particle undergo Snell's law of reflection and refraction, the beam will partially be reflected and partially refracted. A refracted ray might undergo multiple reflections until it leaves the particle. Hence, the angular scattering distribution, absorption and polarization will greatly depend on the geometry and refractive index distribution in the particle. Reflection is characterized by the surfaces, and can be either specular or diffuse.

Diffraction, Babinet's Principle

A general description of diffraction on small particles can be clarified on the basis of two imaginary experiments. For this we should recall the plane wavefront traveling through the scattering particle. Due to the additive property of the (*electromagnetic*) wave nature of light, we separate the wavefront into two independent waves undergoing a different experiment.

Experiment 1 Let's replace the particle by an opaque disk with the geometric size of the scattering particle. Here we can study the 'shadow' of the wavefront behind the the disk. It describes perfectly the behavior of the *incomplete* wavefront passing along the scattering particle.

Experiment 2 In this experiment, the entire wavefront is occluded by a black surface, with a hole similar to the geometry of the scattering particle. Now we are interested in the illumination of the light traveling through the small aperture. This describes the diffraction of the partial wavefront traveling through the particle.

Finally, summing the partial wavefronts from both experiments will give us back our initial plane wavefront since none of the wavefronts have been disturbed. This result is known as *Babinet's Principle* In the case of a scattering particle, the wavefront

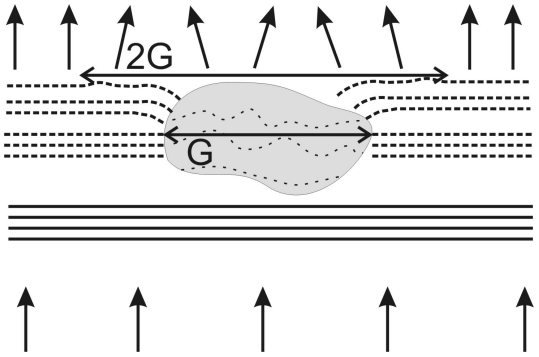

Figure 4.5: Babinet's Principle

in experiment 2 is disturbed, now the interference of the 2 partial wavefronts will can describe the scattering distribution.

The extinction paradox We are interested in the portion of the incoming light affected by diffraction on a scattering particle with a geometric cross section G. For this, it is appropriate to calculate the energy distribution of the scattered wavefront. All energy passing through the scattering particle is either scattered or absorbed, and thus removed from the traveling plane wavefront. This portion corresponds to an *effective cross section* equal to G. Besides this, we have a disturbed wavefront in the surroundings of the geometric cross section. The energy of this diffracted portion can be derived from *Babinet's Principle*. Since the diffracted patterns from experiment 1 and experiment 2 cancel out, we can conclude the the energy diffracted in experiment 1 is equal to the energy absorbed by its black disk. In the case of our scattering particle, this corresponds to a *diffraction cross section* equal to G. The total energy removed from the incoming plane wavefront corresponds to an extinction cross section

$$C_{ext} = 2G \tag{4.1}$$

i.e. an efficiency factor $Q_{ext} = 2$

In large particle scattering, the scattered portion of the incident beam is exactly twice the amount of light it intercepts. This paradox is in accordance with two assumptions: *(a)* all light removed from the plane wavefront is counted as scattered

light. This includes as well light scattering over very small angle that is experimentally hard to distinguish from the non scattered light *(b)* the observation is made at a big distance from the scattering plane, i.e. far beyond the zone where a shadow can be distinguished.

Scattering theory for spherical particles (MIE theory)

classification This section gives an overview of the theoretical description of light scattering by a spherical particle with radius a and refractive index n_{scatt} immersed in a background with refractive index n_{back}. The light is characterized by its wavelength λ (or the corresponding wavenumber $k = 2\frac{\pi}{\lambda}$). The MIE theory is based on other models such as Rayleigh scattering and more specifically on the Rayleigh-Gans scattering. A derivation of the principal equations that are used in the MIE theory is presented in the appendix A. Notations in the following discussion are depicted from the appendix. We make following substitutions:

$$x = ka, \quad m = \frac{n_{scatt}}{n_{back}}, \quad \rho = 2 * x * (mker - 1), \quad z = x * \theta \tag{4.2}$$

ρ corresponds to the optical path difference (OPD) of light traveling over a distance $2a$ (diameter of the particle) in the background matrix when it was traveling through the center of the particle. In the situation of spheres very large compared to the wavelength, the decisive parameter becomes m, when m is close to 1, the OPD can be small compared to 2π. With increasing (or decreasing, when it is less than 1) m, OPD will exceed several multiples of 2π. The scattering process appears to be fundamentally different according this 'phase shift'.

Anomalous Diffraction Based on the observation of reflective particles with a size of $10 - 20\mu m$ in in the entire stromal layer, we will limit this discussion to $x >> 1$. However many eye models document a precise refractive index of the stroma in the visible (we use Navarro *et all* ($n_{back} = 1.36$) [39]), a precise value for the refractive index of the reflective (scattering) particles is more difficult to define. Instead, we derive a formula for arbitrary value of ρ, confined to the limited case where $m \rightarrow 1$.

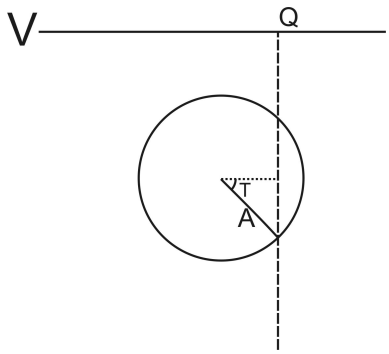

Figure 4.6: Ray passing through a sphere

The scattering diagram is the result of the interference between diffracted light and light transmitted through the particle. For a mathematical formulation, we vary $m-1$ and θ proportionally to $\frac{1}{x}$ so that:

$$\rho = 2x(m-1) \quad and \quad z = x\theta \tag{4.3}$$

are constants. In that case, the following scattering functions

$$x^{-2}S_1(x,m,\theta) \quad and \quad x^{-2}S_2(x,m,\theta) \tag{4.4}$$

approach a common limit for $x \to \infty, m \to 1$ and $\theta \to 0$, which is a function of ρ and z only. This function will be denoted by $A(\rho, z)$. A method to calculate $A(\rho, z)$ is based on the Huygens' principle. We apply the Huygens' principle on a plane V beyond the sphere illustrated in figure 4.6.

Let the ζ -axis be in the direction of propagation and ξ the axis of the projection of the scattering direction on the plane perpendicular on ζ. The phase lag at a point Q within the sphere's shadow is

$$2a\sin\tau \cdot (m-1) \cdot k = \rho\sin\tau \tag{4.5}$$

This phase lag can be included in the equation of the field at the plane V by adding a negative exponential component, $e^{-i\rho\sin\tau}$ in the forward direction. The corresponding *added* field to the incoming wave is $e^{-i\rho\sin\tau} - 1$. Integrating this *added* field over the particle's shadow, we obtain a description of the scattering function in the forward

direction ($\theta = 0$)

$$S(0) = \frac{k^2}{2\pi} \int \int (1 - e^{-i\rho \sin \tau}) d\xi d\eta \tag{4.6}$$

The corresponding phase lag when the scattered ray makes an angle θ with the ζ axis can be derived similarly and we obtain following scattering function:

$$S(\theta) = \frac{k^2}{2\pi} \int \int (1 - e^{-i\rho \sin \tau}) e^{-ik\xi\theta} d\xi d\eta \tag{4.7}$$

Integrating over the shadow of the particle with radius a; τ defined by $a^2 \cos^2 \tau = \xi^2 + \eta^2$ We change to polar coordinates by

$$\begin{aligned} \xi = &\quad a \cos \tau \cos \phi \\ \eta = &\quad a \cos \tau \sin \phi \\ d\xi d\eta = &\quad a^2 \cos \tau d\phi d(\cos \tau) \end{aligned} \tag{4.8}$$

The integration over ϕ can be performed directly by means of the integral:

$$\frac{1}{2\pi} \int_0^{2\pi} e^{-iz \cos \tau \cos \phi} d\phi = J_0(z \cos \tau) \tag{4.9}$$

where $x = ka, z = x\theta$. Thus we obtain

$$A(\rho, z) = \frac{S(\theta)}{x^2} = \int_0^{\frac{pi}{2}} (1 - e^{-i\rho \sin \tau}) J_0(z \cos \tau) \cos \tau \sin \tau d\tau \tag{4.10}$$

However the above integral is exact for complex values of m (in the limited case $m \to 1$, the expansion for the integral will be restricted to real values of m and ρ, i.e. non-absorbing particles. Let ReA and ImA denote the real and imaginary part of $A(\rho, z)$. Substitution of $\gamma = (\frac{\pi}{2} - \tau)$ gives

$$ImA = \frac{\rho}{y^2} \left(\frac{\pi y}{2} \right)^{\frac{1}{2}} J_{\frac{3}{2}}(y) \tag{4.11}$$

where $y^2 = \rho^2 + z^2$. The expansion of ReA for large values of ρ, we separate the

diffracted and the refracted light.

$$A(\rho, z) = A_{diff}(\rho, z) + A_{trans}(\rho, z) \tag{4.12}$$

The radiation diffracted by an opaque disk is found to be:

$$S_1(\theta) = S_2(\theta) = x^2 \frac{J_1}{z} \tag{4.13}$$

which gives

$$A_{diff}(\rho, z) = \frac{J_1}{z} \tag{4.14}$$

For the refracted part, we expect a term $A(\rho, z)$ which has the asymptotic form $i\rho y^{-2} e^{-iy}$ for large values of ρ and has the imaginary part earlier derived. An expression satisfying these conditions is

$$A'_{trans}(\rho, z) = \frac{i\rho}{y^2} \left(\frac{\pi y}{2}\right)^{\frac{1}{2}} H^{(2)}_{\frac{3}{2}}(y) \tag{4.15}$$

where $H^{(2)}_{\frac{3}{2}}(y)$ denotes the Hankel function. Its real part

$$\frac{\rho}{y^2} \left(\frac{\pi y}{2}\right)^{\frac{1}{2}} N_{\frac{3}{2}}(y) \tag{4.16}$$

is to be expected as a term in ReA

Expansion of equation 4.11 in powers of ρ and z leads us to additional terms for ReA to the previous two postulated terms:

$$ReA = \frac{1}{z} J_1(z) + \frac{\rho}{y^2} \left(\frac{\pi y}{2}\right)^{\frac{1}{2}} N_{\frac{3}{2}}(y) + \frac{1}{\rho^2} J_0(z) + \frac{1 \cdot 3}{\rho^4} z J_1(z) + \frac{1 \cdot 3 \cdot 5}{\rho^6} z^2 J_2(z) + \dots \tag{4.17}$$

The remainder terms should be seen as a compromise to correct the assumptions made for the geometric-optics approximation. For simplicity, we will only consider the first term of this remainder term. Adding the real and complex part of $A(\rho, z)$, we can

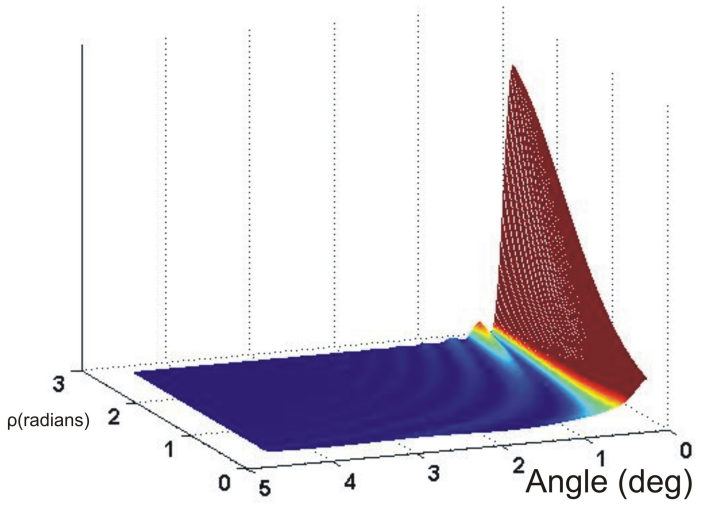

Figure 4.7: Light distribution of anomalous diffraction for different values of ρ.

formulate following expression:

$$A(\rho, z) = \frac{i\rho}{y^2}\left(\frac{\pi y}{2}\right)^{\frac{1}{2}} H^{(2)}_{\frac{3}{2}}(y) + \frac{1}{z}J_1(z) + \frac{1}{\rho^2}J_0(z) \tag{4.18}$$

Remembering that

$$S_1(\theta) = S_2(\theta) = x^2 A(\rho, z), \tag{4.19}$$

we find that the intensity scattered by a single particle under the angle θ is given by

$$I(\theta) = \frac{k^2 a^4 |A|^2}{r^2} I_0 \tag{4.20}$$

Figure 4.7 shows a surface plot of the scattering distribution over the angle θ for a wide range of values ρ.

Dependence on the wavelength

For the formulation of A, we incorporated the the wavelength in the factor $x = \frac{2\pi}{\lambda}a$, and was thus consequently coupled to the variation of the particle size. However in the above intensity equation, the wavelength factor has a power of 2, whereas the particle size term has a power of 4. Hence we conclude that the intensity scattering distribution

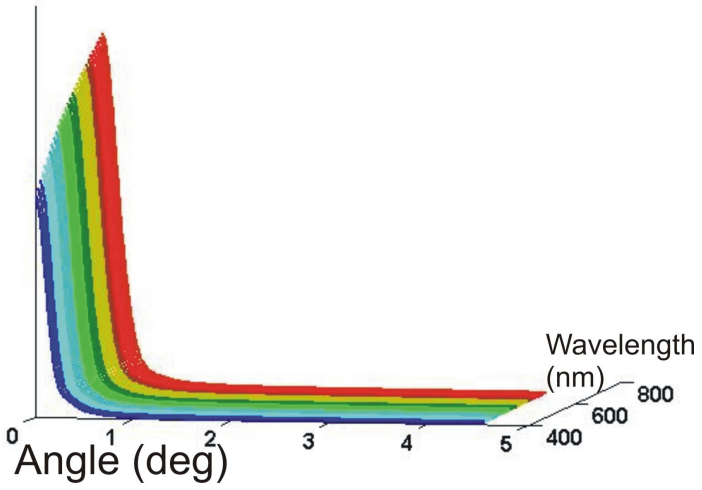

Figure 4.8: Anomalous diffraction on 30 μm particles in different wavelengths

is more sensitive to the particle size then to the wavelength. Figure 4.8 displays the scattering intensity distribution for the range in the visible (200-700nm).

Dependence on the particle size As previously described, the intensity distribution depends more on the particle size. For this we suggest to use a fixed wavelength (550nm), and vary the particle size to optimize our scattering model in the cornea.

Dependence on the refractive index Evidently, the refractive index of the particle has an important impact on the scattering distribution. The model of anomalous diffraction is based on the limit for $m \rightarrow 1$. Defining a fixed value for the refractive index of the scattering particles in the cornea is a very demanding task due to the wide range of present biologic tissues. In our single pass experiments in chapter 7, we have optimized the variation of refractive index based on the experimental measurement of the scattering PSF. We obtained a relative refractive index of 1.0024.

Multiple particle scattering

Assuming that there is no coherence between scattered rays on different particles, we could calculate a scattering intensity distribution for a 'cloud' of many particles, by imply summing the intensities. If each particle i scatters an incoming ray with intensity

I_0 following a scattering function (such as *anomalous diffraction*) $F_i(\theta, \phi)$, it is possible to write following equation:

$$I_{scatt} = \sum_i F_i(\theta, \phi) I_0 \tag{4.21}$$

For this, we can propose a scattering equation for the entire cloud of particles:

$$F(\theta, \phi) = \sum_i (\theta, \phi) \tag{4.22}$$

In this equation, we assume that the scattering medium is optically thin, i.e. either all photons are not scattered or they are scattered only once. When the medium becomes optically thicker, more photons are scattered several times before leaving the medium. This gives rise to a different scattering law, that will not be discussed here. Recalling the extinction cross section, we should sum the extinction cross section for all independent particles. We also recall the extinction cross section for a spherical particle with radius a to be $\pi a^2 \cdot 2$. Let there be $N(a)da$ particles in a volume unit with radii in the interval da, then the total extinction coefficient of the scattering medium becomes:

$$\gamma = \int_0^\infty \pi a^2 \cdot 2N(a)da \tag{4.23}$$

In this thesis, we refer more often to a parameter related the this extinction coefficient, the *ballistic ratio* (BR) as the ratio of the light *not* scattered on its way through the medium:

$$BR = \frac{I_{scatt}}{I_{noscatt} + I_{noscatt}} = \frac{I_{sca}}{I_0} = 1 - \frac{\gamma}{\Omega} \tag{4.24}$$

where Ω denotes the area covered by the scattering medium.

The total intensity distribution of a light source with intensity I_0 passing the scattering medium Ω can now be described in following equations:

$$\begin{aligned} I(\theta) &= BR \cdot I_0 + (1 - BR) \cdot I_{scatt}(0) \quad for \quad \theta = 0 \\ &= (1 - BR) \cdot I_{scatt}(\theta) \qquad\qquad for \quad \theta \neq 0 \end{aligned} \tag{4.25}$$

Chapter 5

A physical Model for Ocular Scattering

In this chapter we validate the scattering law as derived in the previous chapter to a physical model. The theoretical model was restricted to perfect spheres with a known index of refraction. As mentioned, this approximation might vary from the scattering distribution in the cornea. To compare this corneal scattering distribution to the previously described mathematical model of anomalous diffraction, we present a physical model based on a suspension of microspheres in a hydrogel material to simulate the present structures in the cornea. This model was used to make a physical simulation of corneal scattering, and therefore to justify the assumptions made in the anomalous diffraction model and, later on, to simulate the possible effect for increased light scattering following excimer laser surgery on candidate patients. The characterization of the scattering properties in the discussed physical models have been the scope of the MSc thesis of Ioannis Sgouros [50]. For a more detailed description of the models, we refer to his work.

5.1 Characteristics of Microspheres

In figure 5.1, the microspheres are shown as seen under an optical microscope. Microspheres based on SiO_2 can easily be found on the market. They are used in large quantities for applications such as grinding and polishing optical surfaces. Since their chemical constitution is precisely known, it is easy to estimate its refractive index. Moreover, the production process allows to make spheres without roughness. Using

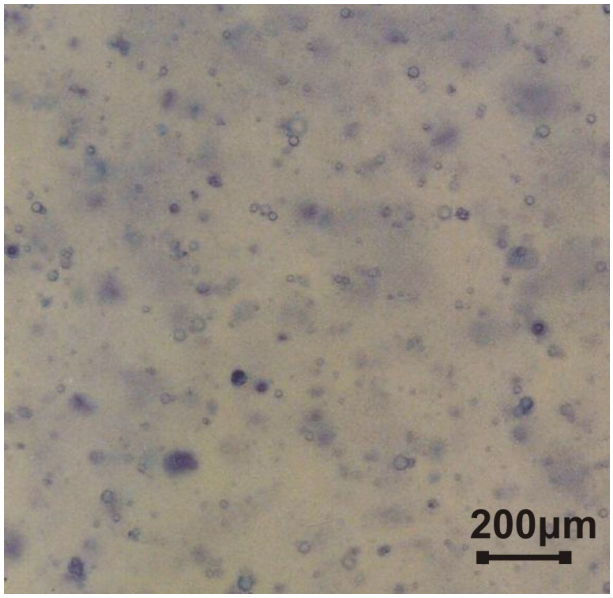

Figure 5.1: Microscopic image of the Jaygo microspheres

Component	Concentration %	Error
SiO_2	72,20%	± 0,20
Al_2O_3	0,70%	± 0,01
Fe_2O_3	0,07%	± 0,002
TiO_2	0,03%	± 0,01
K_2O	0,26%	± 0,01
Na_2O	13,10%	± 0,10
CaO	8,80%	± 0,01
MgO	3,97%	± 0,01
ZnO	0,03%	± 0,01
SiO_3	0,27%	± 0,01
B_2O_3	0,14%	± 0,01
PbO,BaO,Sb_2O_3	$< 0,01\%$	

Table 5.1: Chemical composition of Jaygo Microspheres

an easy filtration system, one can select a range of particle sizes appropriate for its application. In our study, we employ a set of microspheres of Jaygo Inc. The particles have a diameter between 1 and 20 μm. Their chemical composition is shown in table 5.1.

Considering the three main components of the microspheres, the refractive index is proposed to be of 1,45 (Considering the similarity to the silicon glass type BK7). As previously mentioned, the particles have a size ranging from 1 to 20 μm. The size distribution is illustrated in figure 5.2a. Although we see that the size distribution is peaked at $2\mu m$, this conclusion is misleading. In the previous chapter, we derived that

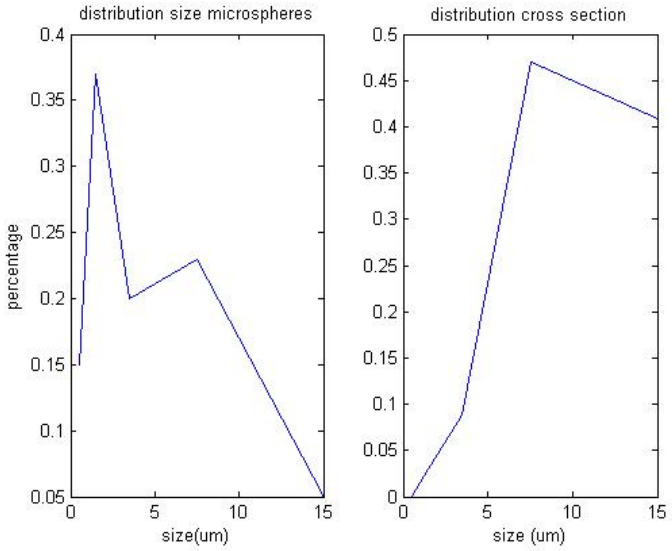

Figure 5.2: Size distribution of Jaygo microspheres. Left: absolute distribution. Right: Distribution corrected with effective cross section

the scattering cross section on a sphere with radius a equals $2 \cdot \pi a^2$. The scattering cross section of a particle increases quadratic with the radius. Therefore, in figure 5.2b we plotted the distribution of effective cross section for the corresponding diameters.

5.2 Selection of the background matrix

Since m is defined as the relative refractive index, $\frac{n_{scatt}}{n_{back}}$, the smallest variation of refractive index of the scatterer is as important as the one for the background material. In air, m remains 1,45; far above the assumption to be close to 1. The refractive index of the background matrix can more easily be varied than changing the scatterer's refractive index. Indeed, it is known that e.g. the refractive index of a salt solution varies with the salt concentration in the solution. We used a refractometer to characterize the refractive index of several available background materials. The results are given in table 5.2.

A *salt solution* is probably the most easy to produce in the lab, and has values for m suitable to proof our theory on anomalous diffraction, a major drawback is the liquid origin of the sample; it is not possible to fixate the microspheres on their background matrix. As a consequence, the spheres are subjective to gravity and a precise,

Matrix	n_{scatt}	m
Water	1.333	1.088
Salt Solution 10%	1.350	1.074
Salt Solution 20%	1.366	1.061
Collagen 10%	1.350	1.074
Collagen 20%	1.366	1.061
Carbomer gel	1.351	1.0733
HEMA	1.437∗	1.0090
RGP CL	1.465∗	0.990

Table 5.2: refractive index for different background materials ∗ refractive index obtained in literature

repeatable concentration lasts only for a very short time interval.

The *collagen* matrix is a gel of water and collagen fibers of porcine skin. Since the cornea consists primary of 20% collagen and 80% water, this background matrix is appropriate to simulate the corneal tissue. The similarity of refractive index of collagen 20% and cornea (1.3771) is notable. A major difference between the collagen solution based on porcine skin and the cornea is the degree of organization. It has been proposed that the high degree of organization in the cornea contributes to its high transparency (see 4.2). The collagen matrix consists of an irregular aggregation of small fibers. When mixing these fibers in water, the fibers get connected to each other in a random organization. This results in a relative stable background matrix that holds the microspheres in their position. On the other hand, we did not see significant light scattering due to the lack of organization between the fibers. We can conclude that this matrix is amorphous and therefore it doesn't originate to light scattering.

Carbomer gel is an ointment clinically used as artificial tear film in dry eyes. It is the equivalent of natural tears in an ointment suspension. As it is used to reinforce the most refractive layer of the eye, it is very suitable to use it as a background matrix to simulate the anterior ocular tissues. In our experiments, we often used a Carbomer gel 0.3% (Thilogel, ALCON Hellas AEBE) to attempt low refractive optical contact between corneal and lens surfaces.

HEMA or hydroxyethyl methacrylate is a material used for the production of soft contact lenses. Suspending a concentration of microspheres in a set of custom made contact lenses could be useful to simulate the effect of corneal scatter on the visual function since the scattering layer can be placed in contact with the cornea.

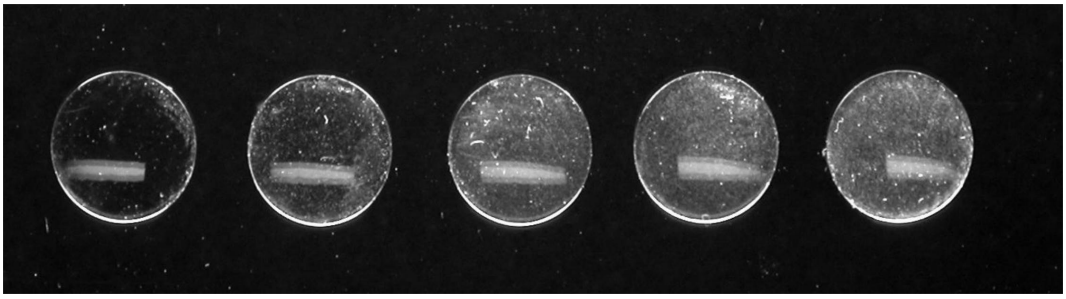

Figure 5.3: Scattering contact lenses with increasing concentration of microspheres (image taken under an angle of 15 degrees with the incident illumination)

RGP CLs or Rigid Gas Permeable Contact Lenses, better known as hard contact lenses, might be even more suitable to be used as a scattering layer since they have long lifetime and can both be characterized in a dry, lab environment and in the eye. For the scope of this thesis, we used a set of plano RGP lenses with four different concentrations of microspheres and a baseline set of non-scattering lenses The lenses were custom made by Menicon Inc. (Japan) for these experiment (figure 5.3).

5.2.1 Preparation of the scattering samples

Collagen matrix

To estimate the scattering effects of a scattering sample, we need to calculate a parameter to estimate a value for BR. This can be retrieved by formula 4.1 as derived in the previous chapter. The geometric cross section of N microspheres in a volume element dV is given by:

$$G = \sum_{i}^{N} \pi a_i^2 \tag{5.1}$$

Expanding this equation the particle size distribution N(r) gives:

$$G = K \int_0^{10\mu m} \pi r^2 N(r) \mathrm{d}r \tag{5.2}$$

Where K is proportional to the concentration of the microspheres in the suspension. The effective scattering cross section C_{scatt} can now be found integrating over the

thickness of the sample t:

$$\begin{aligned} C_{scatt} &= 2 \cdot t \cdot K \int_0^{10\mu m} \pi r^2 N(r) \mathrm{d}r \\ &\cong t \cdot \text{concentration} \end{aligned} \tag{5.3}$$

In our experiments, the scattering samples were "sandwiched" between two microscope plates. The thickness was controlled by spacers with a precise thickness ranging from 50 to 150 μm.

Scattering contact lenses

For the preparation of the scattering contact lenses (sCL), we calculated in a similar way the concentration needed to calculated different scattering levels. The achieved scattering levels seem to be lower than the ones attempted. Confocal microscopy learned us that the microspheres are concentrated at the anterior surface. This could explain migration of microspheres during the polimerisation process.

5.3 Restrictions for single pass scattering measurements

5.3.1 Range of the Solid angle for scattering measurement

Light scattered on a particle can be redirected in every direction. When we measure the light distribution over a certain solid angle on a sphere, we can characterize only a small portion of the scattered light. Especially over wide angles, where the scattered intensity can be up to 4 orders of magnitude smaller than the small angle scattering, assumptions made for the theoretic model are no more valid and the extrapolation of the distribution can give us unreliable results.

5.3.2 Distinction of optical PSF and scattering PSF

To distinguish whether a photon measured on a detector has been scattered is not straight forward. The PSF of a point source at any plane imaged through a scattering

medium can be expressed as follows:

$$PFS_{image} = (1 - BR) \cdot PSF_{optical} \bigotimes PSF_{scattering} + BR \cdot PSF_{optical} \tag{5.4}$$

Since the optical PSF decreases faster than the scattering PSF with increasing angle, for a certain angular range, the intensity of the scattered light has the same order of magnitude as the amplitude of the optical PSF. Especially for highly aberrated eyes, where the tails of the optical PSF are more wide, it is not possible to distinguish whether a photon was scattered or not in a specific angular range. To overcome this restriction, the depolarization effects of light scattering can be used to quarantine scattered light from the PSF [4]. This technique exceeds the scope of this thesis and it is not further discussed.

5.3.3 Relative position of the scattering plane on the optical path

The size of the halo around a PSF on an image is not only dependent on the scattering light distribution, but also on the position of the scattering plane in the optical system. When the scattering plane is a focal plane such as the object or image plane, the scattered light will be imaged on the same position as the non scattered light. To visualize the scattering distribution, the scattering plane should be close to the principle plane of the optical setup. This phenomenon has been described in astronomy and is better known under the *shower curtain effect* [16]. When the scattering plane is on a principle plane far from the entrance pupil of the imaging system, the maximum angular distribution that can be imaged Θ_{max} is limited by the pupil size of the camera. We validated the shower curtain effect by creating an intermediate focus on an imaging system. Some images where the scattering plane was placed in various positions in respect to the intermediate focus are shown in figure 5.5.

When increasing the complexity of the optical setup to measure the scattered light, one should be conscious not to occlude the scattered light by a diaphragm or lens edges on the optical path. This diaphragm would remove the light scattered under an angle wider the angle under which it sees the scattering plane.

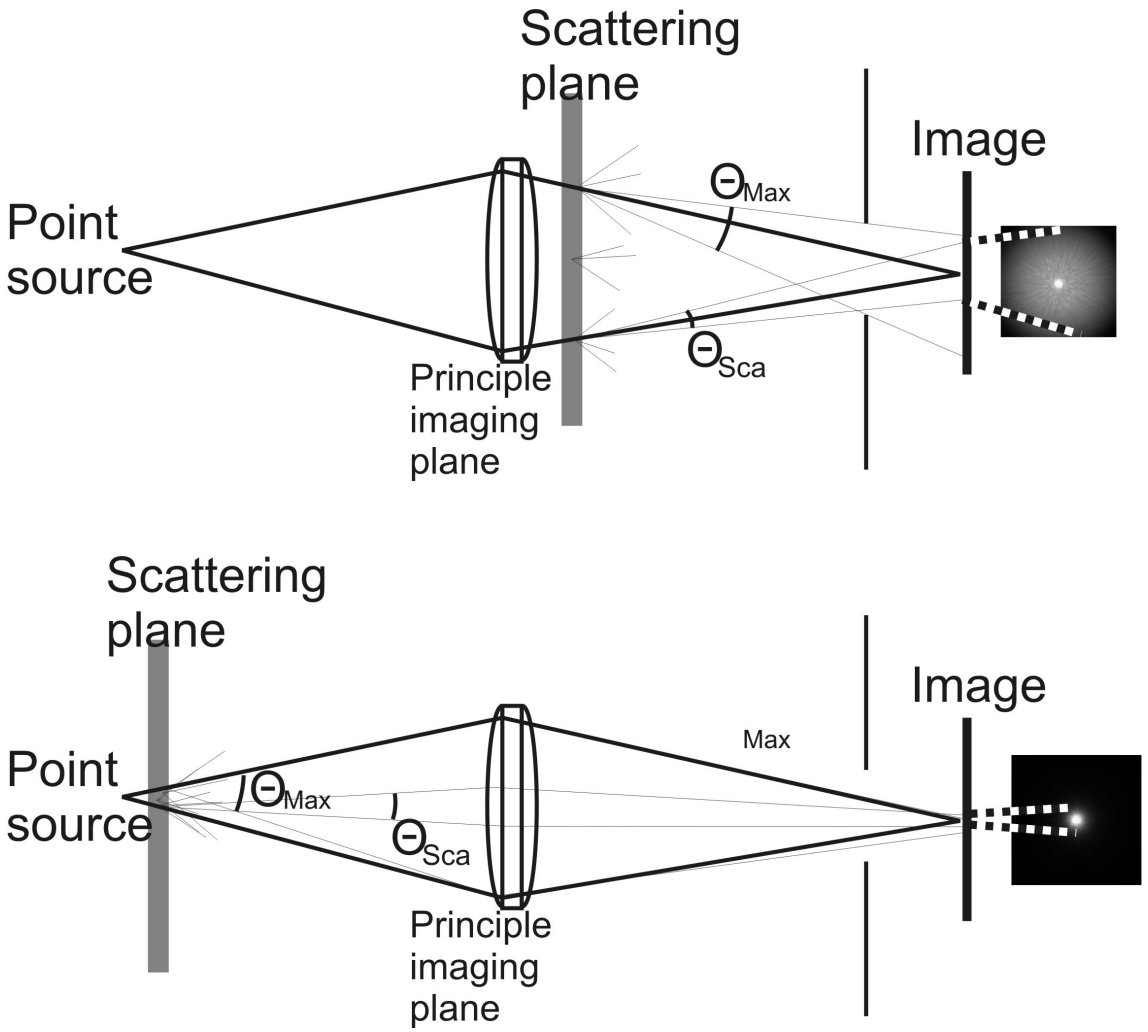

Figure 5.4: Effect of the position of the scattering plane on the scattered image. Up:Scattering plane close to principle plane, Down: scattering plane close to focal plane. Θ_{max} is the maximum scattered angle that can be imaged in each setup, Θ_{sca} compares the magnification of the scattering distribution on the image plane.

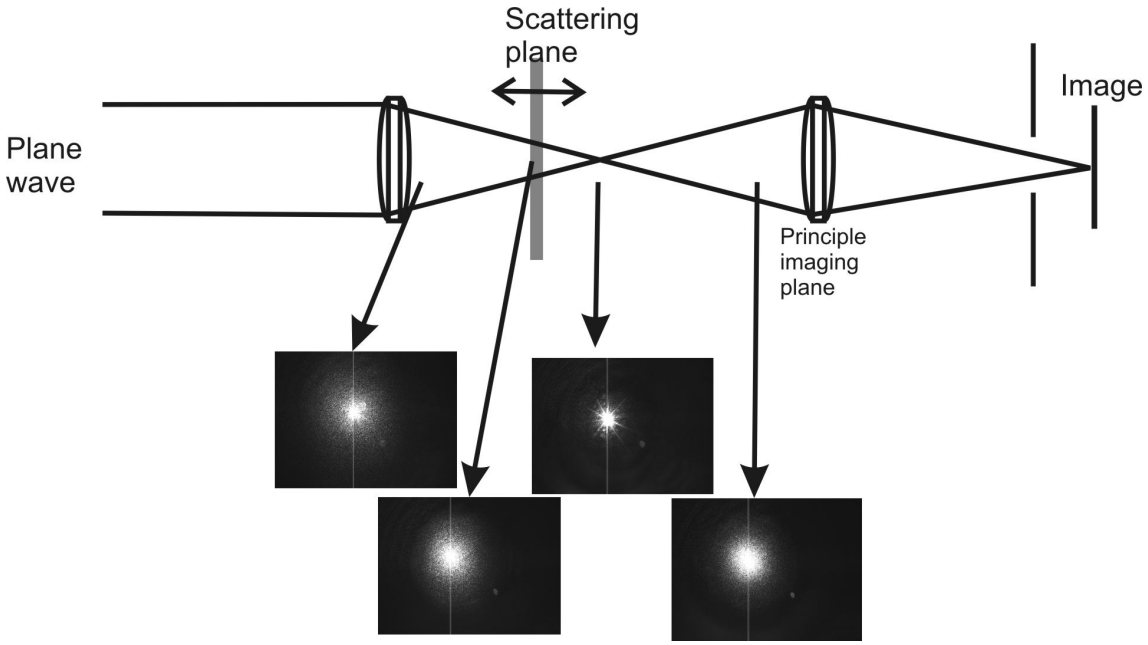

Figure 5.5: Experimental validation of the shower curtain effect by moving the scattering plane through an intermediate focus.

5.4 Characterization of the models

Here, we present a range of methods used to characterize the scattering in the physical models previously described. The methods shown are developed to objectively characterize the forward light scattering in a lab environment. For the scattering characterization, we are interested in two parameters, first the amount of scattered light generated in the scattering sample (defined by its BR), and second we try to derive the forward scattering distribution of the samples.

5.4.1 Scattering measurements by means of a goniometer

The most basic setup for measuring the angular distribution of scattered light is done by mounting a photodiode on a goniometer. The setup used is illustrated in figure 5.6. We used a chopper to periodically illuminate and darken the photodiode. A differential signal on the oscilloscope is generated by the imaging system. The photodiode mounted on the goniometer has an entrance aperture of 2mm, corresponding to an angle of 30 minutes of arc . We measured several scattering samples over angles from 0 to 14 degrees in steps of 1 degree. Figure 5.7a shows the similarity of the measured scattering

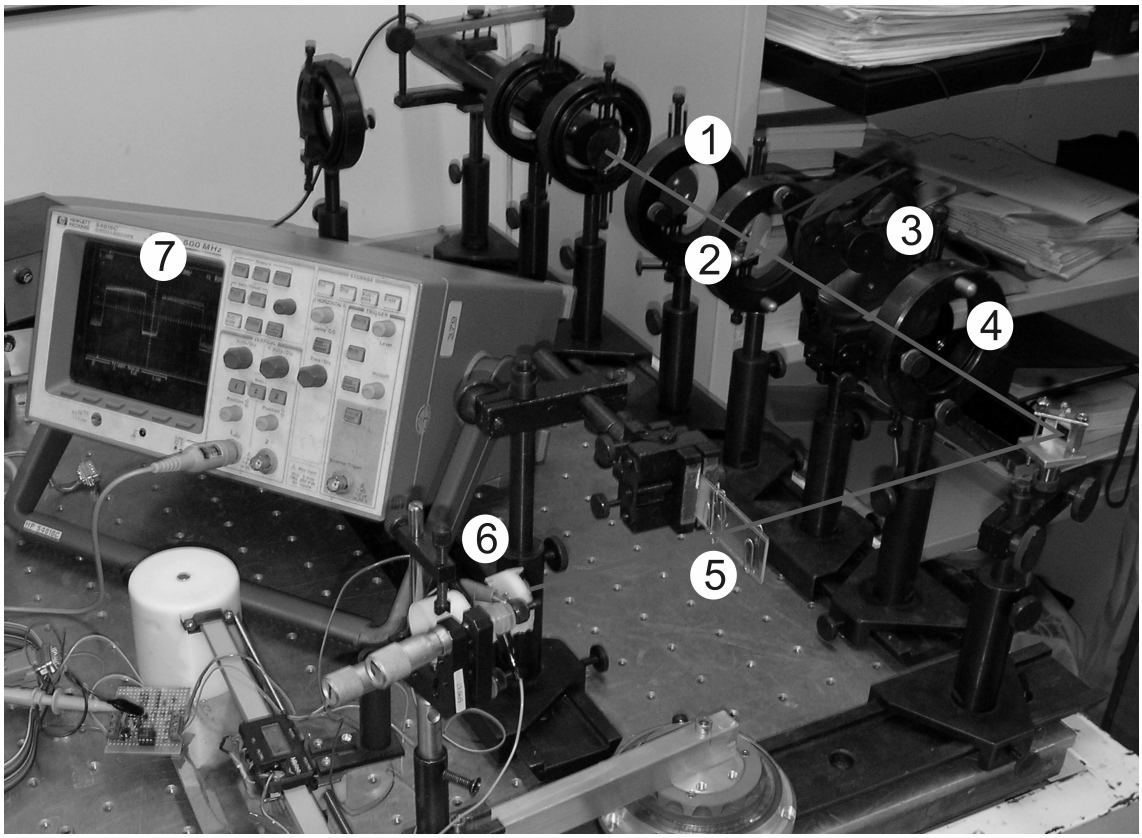

Figure 5.6: optical setup of the goniometer. 1: Point Source, 2: Objective, 3: Chopper, 4: Neutral Density Filter, 5: Scattering Sample, 6: Photodiode, 7: Readout Oscilloscope.

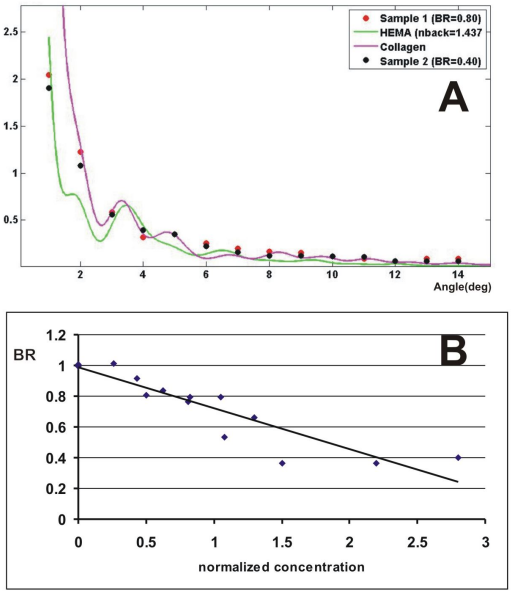

Figure 5.7: upper: Angular scattering distribution of two samples (dotted) compared wih the values predicted by anomalous diffraction (solid lines), lower: Relation between normalized concentration and BR

profiles for 2 different samples and the theoretic predicted value.

Collagen gel background

The background matrix of the microspheres in the experiment was a 20% collagen solution. The error over small angles can be explained by the limited resolution of the goniometer to the relative big aperture of the photodiode. A value for BR can be calculated as the decrease of the signal in the forward direction compared to the level measured when clear, non scattering sample is inserted. Fifteen samples with different concentrations and thickness have been measured in this way. In figure 5.7b, we compare the values for BR to a normalized concentration, as the concentration divided by the sample thickness. We can observe a linear decay of BR by increasing normalized concentration until a certain level around 0.3, where BR tends to decrease slower. This effect can be explained by the multiple scattering events happening in highly scattering media (also called "diffuse light").

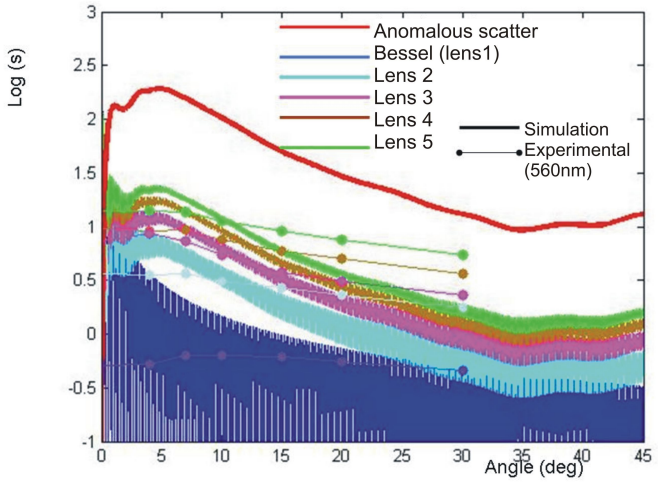

Figure 5.8: Wide angle characterization of scattering CLs.

Scattering Contact Lenses

In a similar setup, the scattering CLs have been characterized over a wide angle ranging from 4 to 35 degrees. This characterization has been conducted in the Netherlands Ophthalmic Research Institute by Tom van den Berg. The large variations of intensity in wide angles make it more appropriate to display the results in terms of $\log(s)$ parameters as described in a further section of this thesis (section 6.1). The results of the wide angle characterization are shown by figure 5.8

5.4.2 Scatter measurements by beam profiling on a chopping knife edge

A first attempt to measure light scattering in a sample is illustrated in figure 5.9.

A light source is focussed on a rotating chopper. The PSF of the light source is affected by scattering properties of the sample inserted between the light source and the chopper. Behind the chopper, there is a 10mm aperture that leads the light into an integrating sphere. The integrating sphere consists of a diffuse cavity coupled with a photodiode. This way, the light level at the photodiode is proportional to the level entering the cavity through the aperture.

As the chopper passes the shadow of the integrating sphere with a speed v, the amount of light in the cavity increases over time as the integral of the PSF over the cavity's

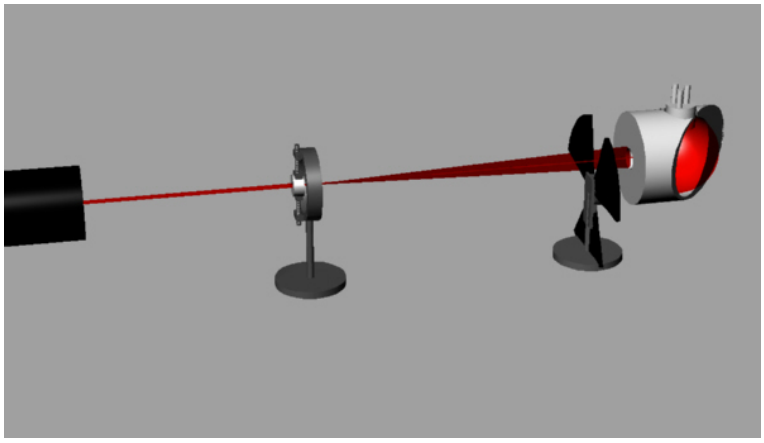

Figure 5.9: Optical setup of the beam profiling experiment

aperture not covered by the chopper:

$$I_{cavity}(t) = \int_0^{vt} \int_0^d PSF(\theta(x,y), \phi(x,y))\mathrm{d}x\mathrm{d}y \tag{5.5}$$

As the chopper covers the cavity with a frequency ν, we can analyze the photodiode signal by the response of the block pulse generated by the chopper and so extract the light distribution on the chopper plane. The entrance pupil of the integrating sphere limits profiling of scattered light up to 1 degree. Lock-in frequency was about 50Hz. Readout-noise of the photodiode amplifier gave us unreliable values for the small angle PSF profiling. The experiment leads us to quantify the amount of scattered light outside the entrance pupil of the integrating sphere by dividing the differential signals for full occlusion/full illumination of the integrating sphere by the chopping knife edge.

5.4.3 Analysis of point source images with enhanced dynamic range

Imaging analysis of a point source imaged on a CCD is an easy technique to quantify the intensity of the scattered light in the periphery of the optical PSF. However, some restriction related to the behavior of a CCD should be taken in consideration:

Limited dynamic range of the CCD

A CCD camera is a device that "translates" the light intensity projected on each pixel into a digital signal. The main restriction of this analog to digital conversion is the

amount of bits available to sample the light signal. When only one bit is available, the intensity can only be quantified in 2 light levels. The amount of bits available for each sampling is called the dynamic range. For all experiments in this thesis, we used the SONY XCD-V700, with a dynamic range of 8bits, corresponding to 256 graynscale levels.

When the image of a point source in the absence of light scattering corresponds to one pixel, the highest possible intensity is 255. The scattered light will fill the pixels of the CCD in the periphery on the image center. When the scattering sample scatters only a portion of the light, this portion is taken from the forward intensity level. Consequently, the scattered light will fill the peripheral pixels with an intensity up to several orders of magnitude lower than the intensity of the non-scattered PSF. Even in highly scattering media, the intensity of scattered light does not exceed the noise level.

A method to enhance the dynamic range of a CCD is to register a set of identical images captured under different intensities. The saturated pixels in highly exposed images are replaced by non-saturated pixels from images captured under lower intensity conditions multiplied by the ratio of the camera's sensitivity in both conditions. These intensities can either be enhanced by reducing the light level (by placing a neutral density filter (NDF)) in front of the camera or by changing the gain of the camera's readout (like varying the exposure time of one image).

Linearity of the CCD's response curve

When making quantitative measurements of the light level on an image with a CCD, we need to know its response curve. The response curve is the relation of light intensity on a pixel and the corresponding digital number in the readout of the CCD. Ideally, this response curve is a linear curve clipped at the saturation level. We measured the response curve of the SONY XCD-V700 by capturing identical images captured under the same camera settings with a set of NDFs. It is displayed by figure 5.10

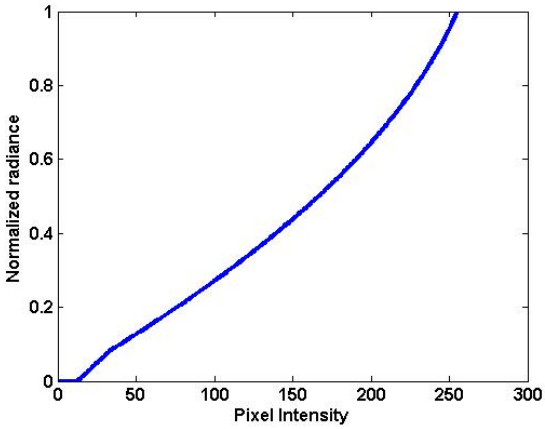

Figure 5.10: Linearity curve of SONY XCD-V700

5.4.4 Measuring scattered light by using an extended source

The imaging of an extended source (such as the semi-disk) is justified when the following considerations are taken into account: light distribution of a point imaged through the scattering surface is a weighted sum of 2 distributions. A part, proportional to BR follows the light distribution according to diffraction and wavefront errors of the optical system. The other part of the light (proportional to 1-BR) distributes the light according to the angular distribution of scatter:

$$PSF_{total} = BR \cdot PSF_{optical} + (1 - BR) \cdot PSF_{scatter} * PSF_{optical} \tag{5.6}$$

Assuming that the $PSF_{optical}$ has significantly smaller dimensions than the $PSF_{scatter}$ the equation above becomes:

$$PSF_{total} \simeq BR \cdot PSF_{optical} + (1 - BR) \cdot PSF_{scatter} \tag{5.7}$$

When an extended source is imaged, the resulting image is a weighted superposition of the original image (blurred with the optical PSF) and the convolution of the blurred image with a function as described in equation 5.7. Typically, in the case of point source imaging, the intensity of scattered light on the image plane is several orders of magnitude smaller (typically 5) than the intensity of the directional light. Thus, it is difficult to observe and accurately quantify the amount of scattered light in an image

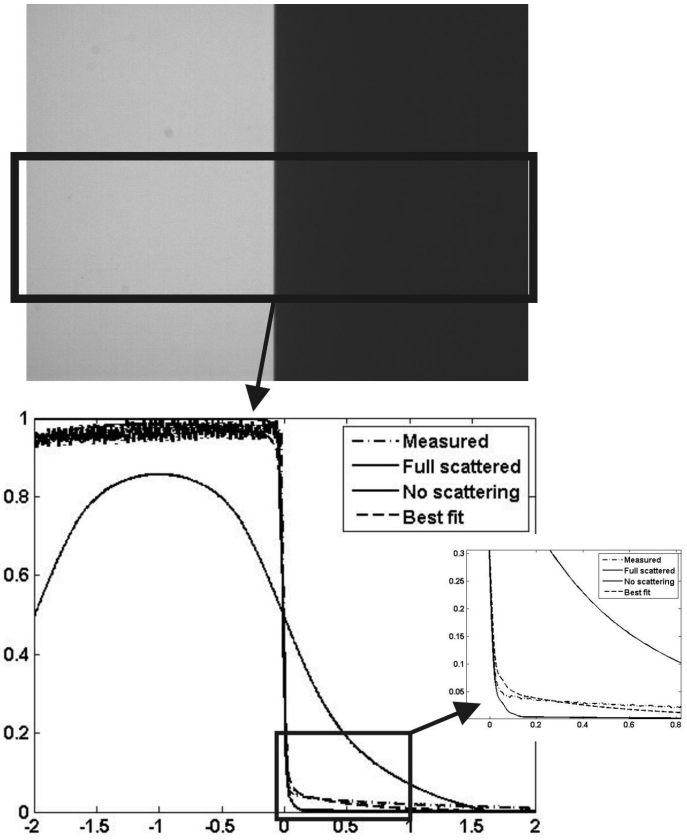

Figure 5.11: Scattering characterization of CLs based on the image transfer of a equally illuminated half field object

of a point source. Utilizing extended sources may result in an image of lower dynamic range, with intensities of scattered light that are relatively higher and therefore easier to measure.

We imaged an object from which the half of the field imaged by the CCD consisted had a uniform illumination and the other half of the field of the field on the CCD was occluded. This allowed us to analyze the light distribution of the scattered light on the step response on the interface between the bright and dark field (see figure 5.11). The method is identical to the method described in section 7.1 for the single pass measurement of corneal scattering.

	Literature	Estimated
Size distribution	10000± 5000	10000± 10000
Refractive index microspheres	1.45	1.455

Table 5.3: Evaluation of scattering parameters in the model of scattering microspheres in RGP contact lenses

5.5 Results

5.5.1 Small angle characterization of scattering contact lenses

For the characterization of the scattering properties of the microspheres in the contact lenses over angles below 2 degrees, the method of the scattering estimation by calculation of the image transfer of a half field object previously described is the most repeatable technique.

First, we validated the assumptions made on the dimensions of the particles. This was done by minimizing the an root mean square (RMS) difference between experimental half field images imaged through the highest scattering CL (lens 5) and a set of simulated images where both BR, refractive index of the microspheres and size distribution of the scattering particles was varied. A comparison between the proposed parameters from the literature and the estimated parameters of the RMS algorithm is given in table 5.5.1. The results are in close accordance with the data obtained in the literature, suggesting the validity of the used method.

Further, using the previously defined parameters, we estimated a value for BR of each contact lens. The results are given in table 5.5.1. There is a large difference between the measured values for BR and the values calculated from the microsphere concentration. This difference can be attributed to the production process. Possibly a migration of microspheres during the polymerization process of the CLs changed the concentration of the microspheres in the lenses. Confocal microscopy revealed that all the microspheres were localized at the anterior lens surface.

Lens	Concentration ($\frac{g}{\mu l}$)	$BR_{attempted}$	$BR_{measured}$
Lens 1	0	1	0.98
Lens 2	0.273	0.8	0.97
Lens 3	0.545	0.6	0.965
Lens 4	0.8189	0.4	0.94
Lens 5	1.0919	0.2	0.91

Table 5.4: BR characterisation of Menicon scattering contact lenses

5.5.2 Wide angle characterization of scattering contact lenses

Characterization of the scattering contact lenses over an angular range from 5 to 45 degrees has been evaluated in the Netherlands Ophthalmic Research Institute by Tom van den Berg. The results are shown previously in figure 5.8. The $\log(s)$ values obtained are in close accordance with values psychophysically obtained in the ageing eye, as described in the next chapter.

5.5.3 Conclusion

We presented a physical model based on glass microspheres suspended in several background matrices. The percentage of scattered light (1-BR) can be controlled by varying the concentration of microspheres. A proposed physical model of scattering contact lenses can be used either for phsychophysical measurements or as a reference scatterer for the calibration of devices (chapters 6 and 7). Comparing the small angle scattering distribution of the microspheres in rigid contact lenses with the experimental verified scattering distribution of hazy rabbit corneas (section 7.1) suggests a rather wide angle scattering distribution of this physical model. This is in accordance with the low scattering values over small angles and normal scattering values in the wide angle characterization.

Chapter 6

Psychophysical Methods for Measurement of Intraocular Scatter

The light scattering in the anterior ocular media has been studied widely in the past. Most investigators have modeled the forward light scattering in the eye with of psychophysical methods [51][58][54]. In these techniques, the light level at the retina due to scatter around a "glare" source is quantified by the *equivalent veiling luminance*. This is the luminance of a corresponding *virtual* light source with the same brightness as the glare is observed around its source. This chapter gives an overview of the history of the psychophysical measurement of forward light scattering and the characterization of the equivalent veiling luminance.

6.1 The glare spread function

6.1.1 Mathematical description of the psychophysical glare spread function

Several methods for psychophysical measurements of scattered light have been proposed [58][25]. Currently, the most common techniques are based on the direct compensation method [58]: while a flickering glare source is projected on the retina, in the opposite phase, a "compensation" target with varying intensity is projected under a given angle with the glare source (which is switched off when this compensation target is projected). The subject is asked to set the intensity of the compensation target until it matches the luminance of the glare at the compensation target. A glare spread

Equation	Angular range	Investigators
$L_v(\theta) = \frac{9.2E}{\theta^2}$	$2.5° < \theta < 25°$	Holladay (1927)
$L_v(\theta) = \frac{4.16E}{\theta^{1.5}}$	$1° < \theta < 10°$	Stiles (1929)
$L_v(\theta) = \frac{29E}{\theta^{2.8}}$	$1° < \theta < 8°$	Vos and Bouman (1959)
$L_v(\theta) = \frac{29E}{(\theta+0.13)^{2.8}}$	$0.15° < \theta < 8°$	Walraven (1973)

Table 6.1: Equations describing the equivalent veiling luminance. $Lv(\theta)$ in cd/m^2, E in lux and θ is in degrees [51]

function can be fitted by the equivalent veiling luminance over a set of angles around the glare source. Initially, the equivalent veiling luminance L_V was calculated by an equation of the form

$$L_V(\theta) = \frac{KE}{\theta^n} \tag{6.1}$$

where E is the illuminance at the plane of the eye of the glare source, θ is the off-axis angle (in degrees) of the glare source, and K and n are constants depending upon the particular investigation and the range of θ. Setting n to 2, this equation is well known as the Stiles-Holliday relationship [54][51]. Some specific equations are given in table 6.1.1.

Analogue to what is suggested in the introduction of this thesis, it is commonly accepted that the scattering function in the eye varies from one subject to another. The direct comparison technique made it possible to study stray light for a wide population resulting in a more accurate mathematical model describing the equivalent veiling luminance. Based on on their experimental findings and on earlier models concerning the glare spread function over small angles, Vos and van den Berg proposed a PSF describing the equivalent veiling luminance as the "glare spread function" [63] [28], which has later been adopted by the Commission Internationalle d'Eclairage (CIE), compromising a general angular description of the 'disability glare" depending on age

and retinal pigmentation. It reads:

$$
\begin{aligned}
PSF = \frac{L_{eq}}{E_{gl}} &= [1 - 0.08\frac{A}{80}^4] \cdot [\frac{9.2 \cdot 10^6}{[1 + \frac{\theta}{0.0046}^2]^{1.5}} + \frac{1.5 \cdot 10^5}{[1 + \frac{\theta}{0.045}^2]^{1.5}}] \\
&+ [1 + 1.6\frac{A}{70}^4] \cdot [\frac{400}{1 + \frac{\theta}{0.1}^2} + 3 \cdot 10^{-8} \cdot \theta^2] + p \cdot [\frac{1300}{[1 + \frac{\theta}{0.1}^2]^{1.5}} + \frac{0.8}{[1 + \frac{\theta}{0.1}^2]^{0.5}}] \\
&+ 2.5 \cdot 10^{-3} \cdot p \\
&[sr^{-1}]
\end{aligned}
\tag{6.2}
$$

where θ is the glare angle in degrees, A the age in years and p a pigmentation factor ($p = 0$ for very dark eyes, $p = 0.5$ for brown eyes, and $p = 1.0$ for blue-green Caucasians) [63][59].

The above equation describes a PSF as it is observed using a psychophysical approach. The first term of the equation describes the small angle part (angle smaller that 1 degree) of the PSF. The function is based on interferometric data from Campbell and Green [6] (1956), a method which is discussed in more detail in section 6.2.2 . The term contains more information on the optical PSF defined by the optical aberrations of the human eye (on a pupil diameter of 4mm) rather than light scattering on the lens and the cornea and is therefore not and important term when evaluating the light distribution of the scattered light, the disability glare. The large angle part of the glare spread function (angles wider than 1 degree) is described in the second and the third term. The second term of the equation describes corneal and lens scattering and the third term, depending on pigmentation, describes the diffused light on the retina. The pigmentation factor suggests more light scattering for blue-green eyes than for very dark eyes. The shape of the PSF was optimized to extrapolate the data from the direct compensation method in a large population.

The last term in the function describes a small portion of the light on the retina entering through the iris and the sclera, but it is several orders of magnitude smaller than the first two terms.

The different terms constructing the glare spread function are plotted in figure 6.1. Given the wide range of angles covering the glare spread function and the high variation

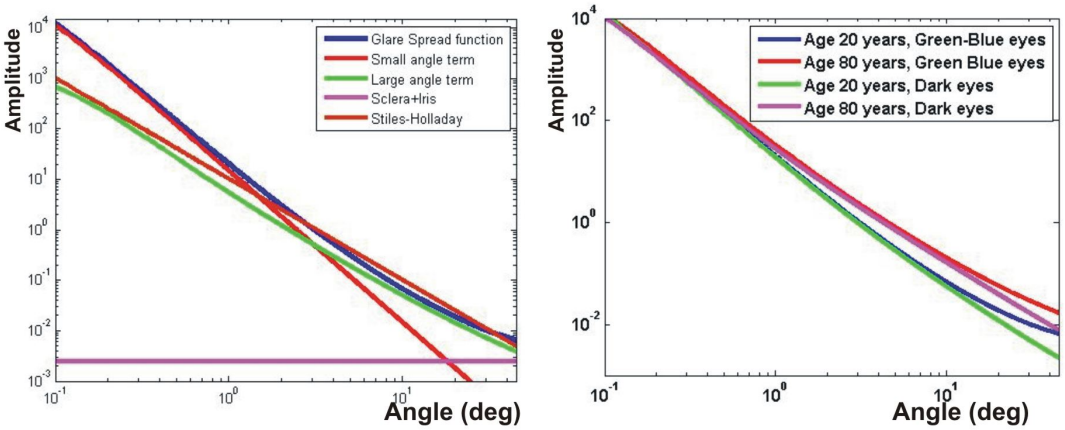

Figure 6.1: Left: Decomposition of the different terms contributing to the Glare Spread Function. Right: Glare Spread function for different age and pigmentation parameters.

of amplitude, the data are plotted in a log-log diagram.

The validity of the glare spread function has been validated using a large database of subjects with different age and pigmentation [28] for an angular range of 5 to 10 degrees. The validity of the function for small angles is based on a dataset of 2 subjects derived from a psychophysical method [6]. Given the low contrast sensitivity for high spatial frequencies on the retina and the limited cone sampling, a more accurate PSF of the eye's optical system could be derived by evaluation of the PSF of the abberated eye, as derived in section 2.1.2 in combination with the forward scattering properties of in vitro samples as suggested in section 7.1 [15][3].

6.1.2 Comparison of the glare spread function and ballistic scattering model

Equation 6.2 describes a general PSF of the image transfer to the retina obtained by psychophysical data. To compare this function with the PSF obtained by the optical scattering model described in chapter 4, we need to take the following approximations into consideration:

PSF of the not-scattered light

The angular distribution in the glare spread function for angles smaller than 10 minutes of arc are strongly affected by ocular aberrations, and is therefore dependent on pupil size. In the glare spread function, a pupil diameter of 4 mm is assumed. The not scattered light results in a PSF taking into account the aberrations over this 4mm pupil (see section 2.1.2). Moreover, when using a polychromatic light source, the chromatic aberrations of the eye will further spread the PSF. To compromise the effect of aberrations over 4mm in a normal eye, we propose the PSF of a polychromatic light source (400-700nm) through a diffraction limited system with a pupil size of 2mm. As this PSF is just valid for very small angles in the PSF on the retina, smaller than the area where light scattering is measured, it should not be put too much attention on the accuracy of this approximation. In the following figures, the angular axis will not show data for angles smaller than 6 minutes of arc.

PSF of the scattered light

In chapter 4, several methods have been proposed to obtain the scattering distribution in the cornea. In the course of this manuscript, the anomalous diffraction model has been proposed to describe the ocular scattering. The model is optimized and validated by optical means in the following chapter. The model is optimized over an angular range from 0 to 2 degrees, which is considered to be the small angle portion of the scattering distribution (see section 7.1). The approximations in the model, and additionally the presence of very small scattering particles in the ocular media will reduce the validity of the scattering model over wider angles. Thus we do not compare both models for values over 10 degrees.

Separation of scattering components in the glare spread function

The glare spread function describes the stray light as observed in the retina. This includes light scattering on the cornea, crystalline lens and retinal diffusion. The ballistic scattering model takes only into consideration the scattering on the cornea and the crystalline lens. To minimize the effect of retinal diffusion in the glare spread

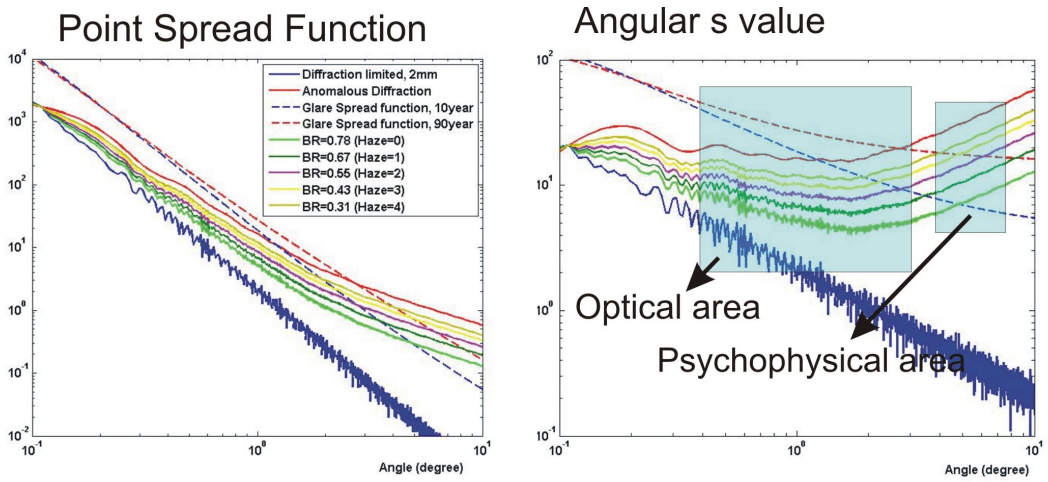

Figure 6.2: Comparison of psychophysical and optical scattering model. Left:PSF, Right: derived s-function. Both plots are displayed in log-log diagram. Legend applies for both plots.

function, we consistently used a pigmentation factor 0 (very dark eyes). The age factor in the glare spread function can be directly correlated to the increasing amount scattering particles (mainly) present in the crystalline lens. Several investigators in the field of lenticular scattering applied the same model of anomalous diffraction and suggested similar parameters for the scattering in the crystalline lens as we observed in the cornea [59][10]. For this reason, we extend the validity for our scattering model to the light scattering in the crystalline lens in this section.

In figure 6.2, the PSF of both models is compared with various parameters in each model. Given the analogue behavior of the glare spread function to the (Stiles-Holladay) $\frac{1}{\theta^2}$ equation, it is often suggested to compare the profile of the light distribution using the s function, where:

$$s(\theta) = \theta^2 \cdot PSF(\theta) \tag{6.3}$$

The s-functions corresponding to the PSF displayed in the diagram on the left of figure 6.2 are shown in the diagram on the right. The dashed lines correspond to the glare spread function, where the age was varied from 10 years to 80 years. The solid lines correspond to simulations obtained from the ballistic model. The amount of scattering was varied in different steps corresponding to the different values of corneal (backscattered) haze rating as clinically observed in a slit lamp exam.

Haze grade	BR	log(s)	Age
0	1 to 0.78	< 1	0 to 63
1	0.67	1.1745	76
2	0.55	1.3069	86
3	0.43	1.408	93
4	0.31	1.49	100

Table 6.2: Comparison of values obtained in psychophysical model and ballistic simulation for clinically relevant values

As mentioned, both methods are focussed on different angular regions. We observe a close relationship between the variation of the age factor in the glare spread function and the variation of BR in the ballistic model in the psychophysical area. The significant difference between the two models in the optical area could be explained by the approximations made in the diffraction limited PSF used for the non scattered light in the ballistic model.

Given the high similarity in the psychophysical area, we can give a corresponding age value for each value of BR, as introduced in chapter 4. Given the small variations in the psychophysical model for young subjects and the high variations for very low scattering media in the ballistic model, we only compare the results for log(s) values higher than 1. When the log(s) value is lower than 1, it is reasonable to assume that the cornea is clinically clear in a slit lamp exam. Moreover, note that the haze grading is a subjective estimation and the relation between haze grade and BR can vary depending on the clinician who assessed the eye. In our data, all haze data were assessed by the same clinician. Table 6.2 gives an overview of significant values based on the different models. This table can be useful when interpreting the values for BR, i.e. addressing an age estimation to a specific value of BR or haze grade.
The data shown result from in vitro measurements obtained with rabbit corneas extrapolated to the ballistic scattering model described in section 7.1. The validity of the approximations in this model should be proved by making straylight measurements with subjects expressing specific corneal pathologies. So far, there are not made studies yet on straylight measurements in a large population of subjects with corneal pathologies. It would be of use to compare outcomes from such studies in optical models describing corneal light scattering.

6.2 Contrast sensitivity function

A common psychophysical method for the assessment of ocular scattering is to measure the contrast sensitivity for a set of sinusoidal gratings with various spatial frequencies. The contrast sensitivity function (CSF) describes the threshold contrast that the observer can distinguish at each spatial frequency. The CSF is generally measured over a range of 0.2 (corresponding to the foveal field) to 60 (corresponding to the sampling resolution of the photoreceptors) cycles per degree. The contrast C for each spatial frequency is calculated by following equation, according to Michelson [32]:

$$C = \frac{I_{max} - I_{min}}{I_{max} + I_{min}} \tag{6.4}$$

Where I_{max} and I_{min} are respectively the maximum and minimum intensity in the sinusoidal grating.

6.2.1 Conventional contrast sensitivity measurement

In a conventional assessment of the contrast sensitivity function, the observer is asked to distinguish a set of sinusoidal gratings on a screen with varying spatial frequency and contrast. For each spatial frequency, a threshold contrast c_{th} is addressed to the contrast on which the observer can just distinguish the gratings. Since a high contrast sensitivity is achieved when c_{th} is low, the constrast sensitivity is expressed as follows:

$$CS(\nu) = \frac{1}{c_{th}(\nu)} \tag{6.5}$$

Where ν corresponds to the specific spatial frequency of the grating. As in figure 6.3, the CSF is usually expressed on a logarithmic scale.

The CSF is not only the result of the image quality on the retina, the CSF is also affected by neural factors, like the response of the photoreceptors. Thereafter, when comparing different CSFs, all measurements should be conducted in the same illumination conditions. As figure 6.3 shows, the CSF tends to decrease for spatial

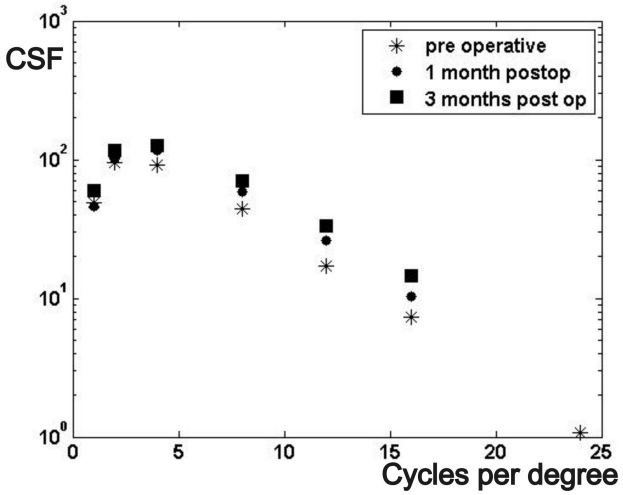

Figure 6.3: Contrast sensitivity of an average population of refractive surgery subjects. Measurements were held with a luminance of $60cd/mm^2$ and a 3 mm pupil diameter[22].

frequencies lower than 4 cycles per degree. This phenomenon cannot be explained by the image quality on the retina. It is due to neural processing in the human visual system. Since the contrast of the gratings of the stimulus (screen) is reduced on the retina by the optical limitations of the eye (aberrations and light scattering, see 2), one could be interested in the actual contrast sensitivity on the retina (bypassing the ocular optics). To do this, we need to divide the CSF with the MTF of the optical system in the eye as described in chapter 2. In our (simplified) model, we consider an orientation symmetric PSF.

$$CSF_{retina} = \frac{CSF_{eye}}{MTF_{aberrations} \cdot MTF_{scattering}} \tag{6.6}$$

Where CSF_{retina} corresponds to the absolute contrast sensitivity on the retina and CSF_{eye} represents the CSF modulated with the optical characteristics of the eye. Considering a healthy eye, where 15% of the incoming light is scattered following the anomalous diffraction (see chapter 4), the CSF is corrected by the scattering MTF and the optical MTF in figure 6.4

Evaluating the post-operative CSF of refractive surgery patients, this method could allow us to measure the increased amount of light scattering after laser treatment. Indeed, assuming that the CSF_{retina} is not affected by laser treatment, $MTF_{scatter}$ could be extracted since we have accurate data on the $MTF_{aberrations}$ from a wavefront

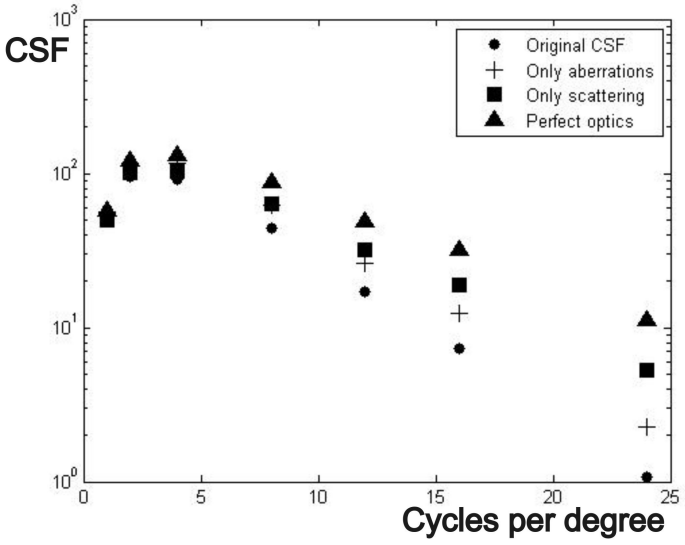

Figure 6.4: CSF as simulated under different conditions on the retina

exam:

$$CSF_{retina} = \frac{CSF_{eyepreop}}{MTF_{aberrationspreop} \cdot MTF_{scatteringpreop}}$$

$$CSF_{retina} = \frac{CSF_{eyepostop}}{MTF_{aberrationspostop} \cdot MTF_{scatteringpostop}} \tag{6.7}$$

$$\frac{MTF_{scatteringpostop}}{MTF_{scatteringpreop}} = \frac{CSF_{eyepreop}}{MTF_{aberrationspreop}} \cdot \frac{MTF_{aberrationspostop}}{CSF_{eyepostop}}$$

The above algorithm has been tested on the CSF of my eye in the follow up of a PRK treatment. All CSF curves and aberrations were analyzed for a 3mm pupil, CSF was assessed under an illumination condition of $60cd/mm^2$. The result is shown in figure 6.5. We see in the 3 months post operative exam a MTF with values higher than 1, that could correspond to a reduced amount of scattering. Given the low MTF of the eye's optical system for high spatial frequencies, the method is more sensitive for small variations of the contrast threshold reducing the stability of the method.

In an analogue way, we could estimate the MTF addressed to the increased light scattering of the ageing eye. We used data on the CSF of a population with three age groups, subjects younger than 30 years, an age group between 50 and 60 years and a

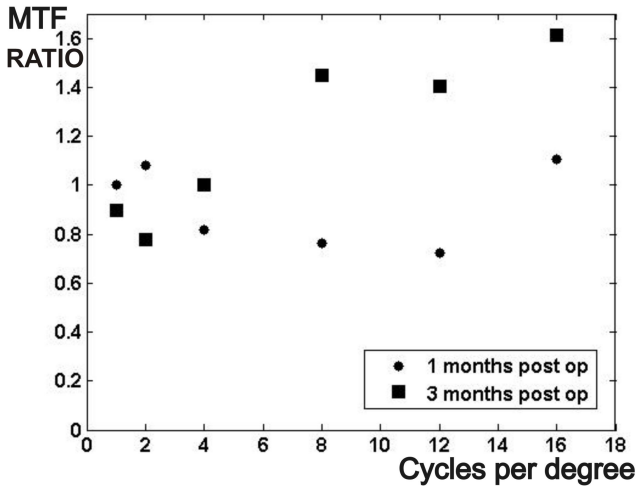

Figure 6.5: Estimated MTF of the increased amount of scatter after PRK

group of subjects older than 60 years. The data are depicted from Hohberger et al. [27]. However we have no data on the ocular aberrations of the subjects, we consider the MTF addressed to the aberrations to be constant [47]. The results are shown in figure 6.6. On the left, the different CSF curves are shown, whereas on the right diagram, the MTF is extracted as the ratio of the CSF of the second and third age group to the CSF of the first (youngest) age group. The very low values in the MTF of the oldest age group could give us a wrong idea of the intraocular light scattering in the ageing eye though. In the above methodology, we ignored the variations of the retinal sensitivity in the eye. A degeneration of the neural pathways on the macula will also result in a reduced CSF, especially in low frequencies [17]. Therefore, comparing the CSF of the eye in different age groups is not appropriate to estimate the scattering properties related to the ageing eye.

6.2.2 Contrast sensitivity by interferometry

To avoid the effect of the ocular aberrations on the CSF , we propose in this paragraph an alternative method for the measurement of the CSF in the absence of refractive errors. The method is based on interferometry and has previously been described by Campbell and Green and has been the scope of the MSc thesis of Anastasios Papadiamantis. For a more detailed description of the technique, we refer to his thesis[44].

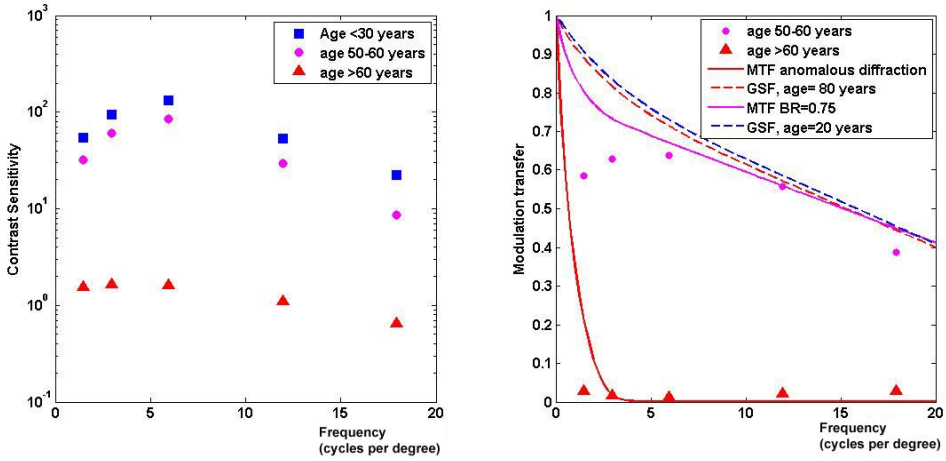

Figure 6.6: Left: Contrast sensitivity function for 3 different age groups. Right: Estimated MTF addressed to the scattering in the ageing eye, compared with MTF of the glare spread function and the anomalous diffraction theory.

Interferometry

The difference between conventional and interferometry based contrast sensitivity tests is that with the interferometry technique, the gratings on the retina are generated by interference. A coherent light source is separated in two beams with two small apertures. The propagation of the two coherent beams result in an interference pattern on a plane behind the apertures where the two beams overlap. In the case of the eye, this plane is the retina and ideally, the two apertures are on the pupil plane. The intensity of the fringes can be described by following equation:

$$I(\theta) = 2 \cdot I_0(1 + \cos\delta(\theta)) = 4 \cdot I_0 \cos^2 \frac{\delta(\theta)}{2} \tag{6.8}$$

Where δ corresponds to the phase lag between the two beams observed under an angle θ:

$$\delta(\theta) = \frac{2\pi}{n_{eye}\lambda} \cdot d \cdot \theta \tag{6.9}$$

Where n_{eye} is the refractive index of the vitreous, λ represents the wavelength and d represents the distance between the two apertures. The spatial frequency can now be directly calculated by the distance between the two apertures:

$$Spatial frequency = \frac{d}{n_{eye}\lambda} \tag{6.10}$$

The image of the gratings projected on the retina in the conventional method is affected by the optical quality of the eye. This includes both light scattering and aberrations on the optical surfaces of the eye. On the other hand, the interference fringes are not affected by the abberations of the eye, the fringes are not projected on the retina by image transfer *through* the pupil plane, but as an interference pattern of two point sources *in* the pupil plane. This omits the reduction of the retinal image quality due to aberrations and so it is only affected by light scattering in the lens and the cornea.

6.2.3 Extracting scattering information

The scattering MTF addressed to the increased light scattering after refractive surgery can be evaluated in a similar way as described in section 6.2 by comparing the change of the CSF before and after laser treatment. Again, we do not consider a significant change of the neural response at the retina after laser treatment. We than can propose following equation:

$$\begin{aligned} \frac{1}{CSF_{conventional}} &\simeq MTF_{neuralprocessing} \cdot MTF_{aberrations} \cdot MTF_{scattering} \\ \frac{1}{CSF_{interferometry}} &\simeq MTF_{neuralprocessing} \cdot MTF_{scattering} \end{aligned} \tag{6.11}$$

Figure 6.4 shows the effect of the different contributions of the visual function on the CSF. The figure illustrates that, whereas the scattering MTF affects a wide span of the CSF, ocular aberrations mainly affect the CSF at high spatial frequencies.

6.2.4 Validity of the method

This method takes into account that scattered light destroys its coherent properties, resulting in a contrast reduction of the interference fringes formed on the retina. The validity of this phenomenon should be tested with a a scattering eye model using a CCD camera on the retinal plane. We have no experimental data of the setup developed and described below. However, several theoretical considerations should be taken into

account:

Theoretical model

In chapter 4, several theoretical models describing ocular light scattering have been presented. The model generally used in this thesis, based on the small particles scattering, assumes no coherence between the light scattered on different particles. Taking this assumption into consideration, the scattered light would reduce the contrast of the interference fringes projected on the retina, in accordance with the hypothesis.
Another theoretic approach proposed in chapter 4 is based on the image formation through a scattering medium considering the local optical path difference of the scattering medium. In this approach, the scattering medium gives rise to a speckle noise pattern, which would also affect the interference fringes. This would not necessarily reduce the contrast of the fringes, however, given the very local dependency of the position of the beam on the scattering object, the speckle pattern would be averaged due to the high frequency of eye movements compared to the integration time of the photoreceptors. This would again result in a contrast reduction of the interference fringes on the retina.

MTF associated with the neural processing

As previously mentioned and illustrated in figure 6.4, the neural response of the ganglion cells in the macula is not the same for each spatial frequency. To model this response, it would be of use to address an MTF to the neural response as we did to model the optical image transfer to the retina (section 6.2). Since the spatial response of the photoreceptors exceeds the scope of this thesis, we only focus on interindividual measurements of contrast sensitivity (like before and after refractive surgery), where the neural processing is assumed to be identical in both conditions.

6.2.5 Experimental setup

Although we have no experimental results on the effect of ocular scattering using the interferometry based CSF, the interferometry setup we have developed in order to

evaluate the CSF based on interference will be briefly discussed. For a more elaborate description and working of the setup, refer to the higher mentioned masters thesis. It is based on the Michaelson scheme, as shown in figure 6.8. A collimated coherent light beam is separated on a first beamsplitter, one part used as reference beam gets reflected through a fixed mirror, the other portion is reflected by a mirror mounted on a double wedge. When rotating the one wedge around the other, the light gets reflected under a different angle. This gives rise to a optical path difference of $\sin(2\theta) \cdot d$, where θ denotes the angle created by the wedge and d is the distance between the mirror and the beamsplitter. This allows us to vary the position of the second virtual point source on the eye's pupil and thus varying the spatial frequency of the fringes on the retina. For the particular configuration of our setup, we can calculate the spatial frequency based on the wedge angle θ as follows:

$$f_{spatial} = 25.859 \cdot \theta \tag{6.12}$$

where θ is the wedge angle in degrees.

A diaphragm between both beamsplitters was inserted to avoid the contribution of secondary reflections from the first beamsplitter on the interference pattern. A consequence of this diaphragm is that the maximum spatial frequency of the interference fringes is limited. All measurements were conducted in a range between 2 and 10 cycles per degree. Behind the wedge, a rotation wheel was mounted to vary the orientation of the fringes on the retina. Finally, the contrast was modulated by the polarization of the coherent and incoherent light source. Beamsplitter 1 is a polarizing beamsplitter that only passes the vertical polarization to the second beamsplitter. A horizontal polarizer is mounted in front of the incoherent light source. When both coherent and incoherent light sources are mixed, behind beamsplitter 2, a second polarizer is inserted to select the portion of coherent (vertical polarization) and incoherent (horizontal polarization) light. A photograph of the setup is shown in figure 6.7 A set of representative interference fringes with varying spatial frequency and contrast, acquired with the reference CCD is shown on figures 6.10 and 6.9. Finally, we used the instrument to measure the contrast sensitivity on the retina (beyond the ocular optics) of one subject (two eyes). The result is given in figure 6.11.

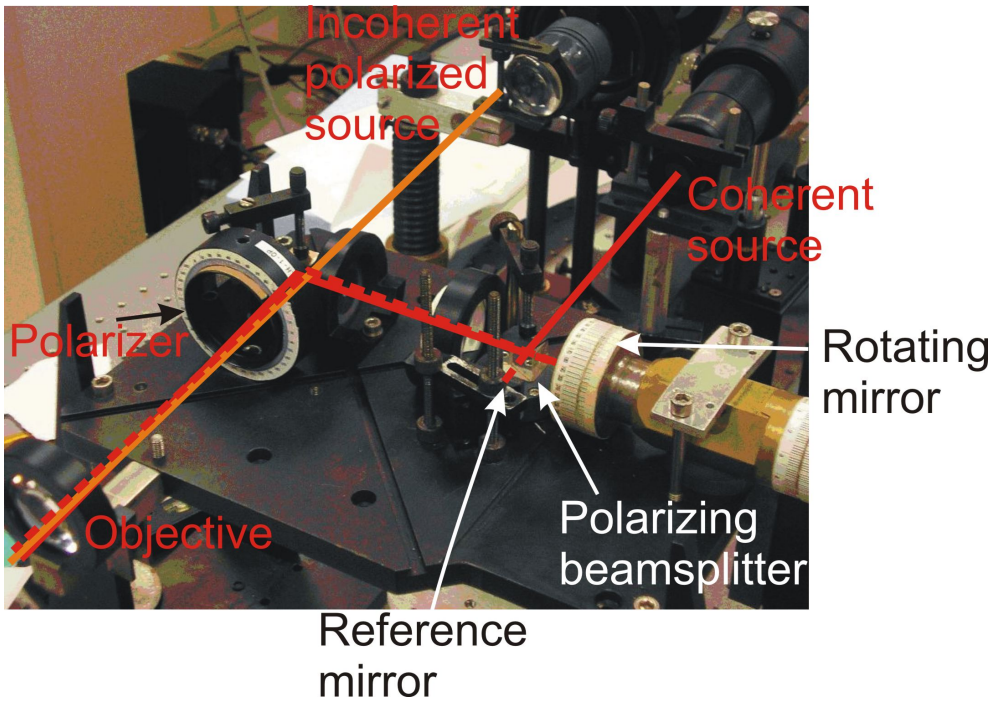

Figure 6.7: Laboratory setup of the Michealson interferometer

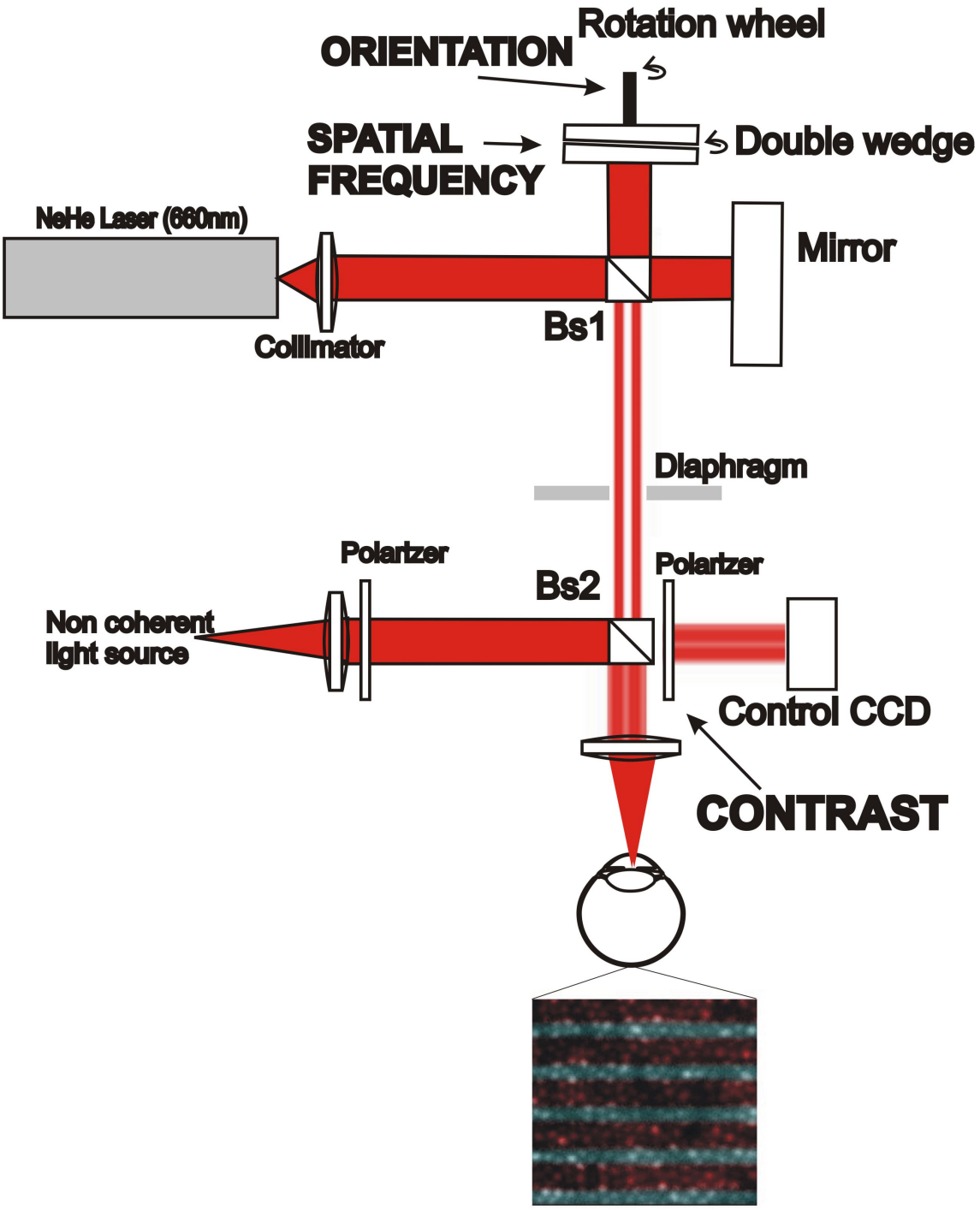

Figure 6.8: Optical setup of the Michaelson interferometer

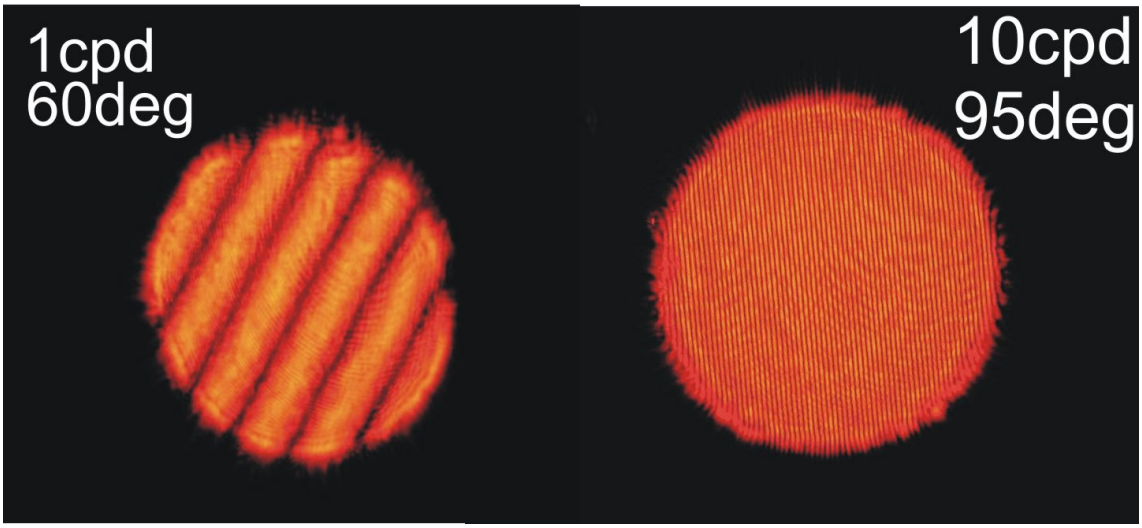

Figure 6.9: Interference fringes acquired by a reference CCD with different orientation and spatial frequency

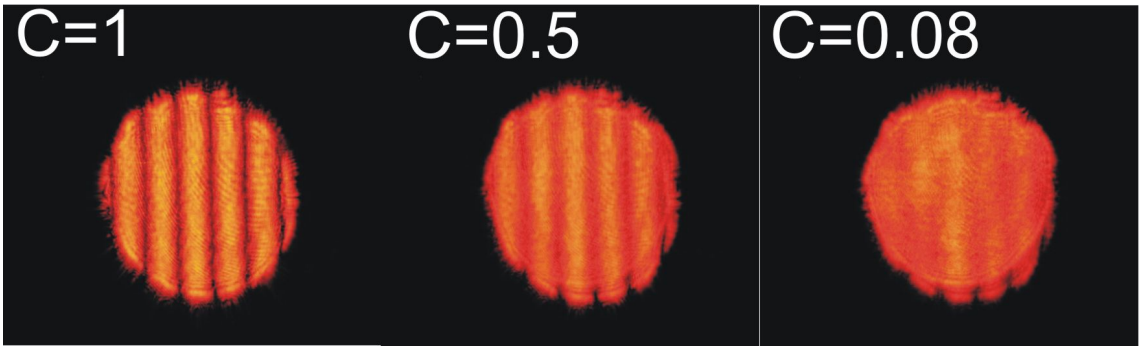

Figure 6.10: Interference fringes modulated with the incoherent source for contrast variation

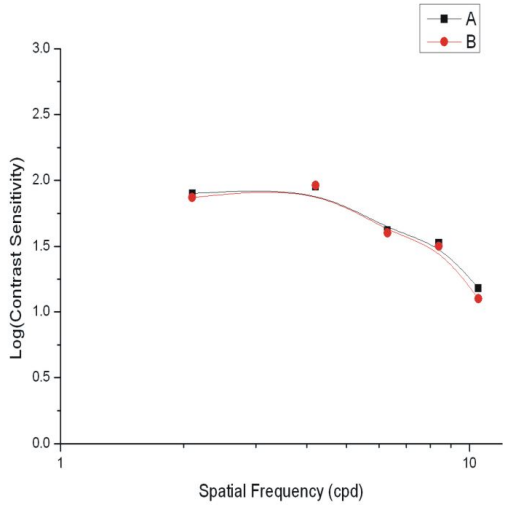

Figure 6.11: Contrast sensitivity function as measured with the interferometer setup

6.3 Straylight measurement

As mentioned, currently the most common method for psychophysical measurement of intraocular light scattering is the direct compensation method. We used the C-quant straylight meter developed by van den Berg and Coppens [19]. A flickering annulus covering the visual field from 5 to 10 degrees is used as a glare source. While the glare source is flickering, the subject is asked to look in the center of the annulus where a semi-disk is used as compensation target and flickers in the opposite phase as the glare source. The straylight is measured in the opposite semi-disk of the compensation target. The subject is asked which of the semi-disks is most intense (or which one of the semi-disks flickers). When the glare source is illuminated, the luminance in the center is the equivalent veiling luminance of the glare source. When the glare source is turned off, one of the semi-disks has the luminance of the compensation target. By using a range of luminances, a psychometric function can be interpolated on the data of the subjects' decision resulting in an accurate value for the equivalent veiling luminance. The measurement of the CSF, affected by the neural processing of the retinal image, is a subjective measurement, the compensation comparison method is an objective psychophysical method since the flickering compensation target is, in the opposite phase, adjusted to the luminance of the straylight originating from the glare source. Thus, the decision of the observer is directly affected by retinal image quality. The resulting equivalent veiling luminance is expressed in a logarithmic straylight parameter:

$$\log s(\theta) = \log(\theta^2 \frac{L_{eq}}{E_{gl}}) \tag{6.13}$$

Where θ is expressed in degrees. Given that the straylight in the C-quant originates from an extended source, the equivalent veiling luminance in the center of the annulus in an integration of the equivalent veiling luminance is obtained from equation 6.2, corresponding to the equivalent veiling luminance of the point source. Integration is

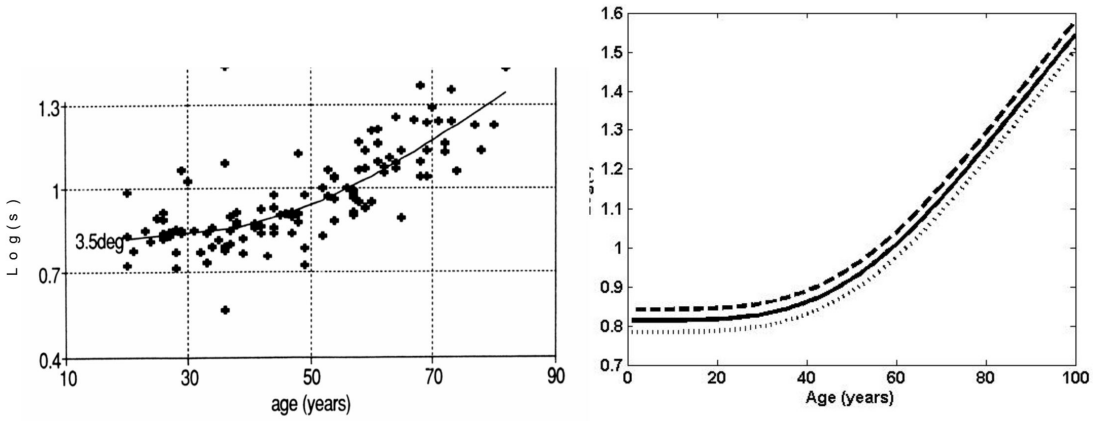

Figure 6.12: General outcome of the C-quant oculus straylight meter. Left: data set of an average population (source: Tom van den Berg) Right: Log(s) at 7 degrees obtained from the glare spread function (dotted: p=0; solid:p=0.5; dashed:p=1)

done as follows:

$$\begin{aligned} L_{eq} &= \int_{annulus} \theta^{-2} s(\theta) \cdot L_{annulus} d\omega \\ &= L_{annulus} \cdot \int_{\theta_{inn}}^{\theta_{out}} \theta^{-2} s(\theta) \cdot 2\pi \cdot \sin(\theta) \cdot d(\frac{\theta\pi}{180} \\ &= 0.0044 L_{annulus} \cdot \int_{\theta_{inn}}^{\theta_{out}} s(\theta) d\log(\theta) \end{aligned} \tag{6.14}$$

The above equation gives a direct relation between the equivalent veiling luminance in the center of the annulus and the integral $\int_{\theta_{inn}}^{\theta_{out}} s(\theta) d\log(\theta)$. This allows us to calculate the s-parameter and compare the results to an average population. A set of results is shown in figure 6.12.

6.4 Straylight measurements of calibrated scattering contact lenses

6.4.1 Straylight of scattering contact lenses

We used the C-quant oculus straylight meter to measure the scattered light on the scattering contact lenses as described in the previous chapter by a psychophysical method. The scattering on the microspheres in the contact lenses cause an additional

amount of scattering in the eye. Given the single scattering approximation used in the ballistic model, the resulting value for the scattering ratio SR, calculated as $1 - BR$ is proposed as follows:

$$\begin{aligned} SR_{eye+Contactlens} &= \frac{scatteredlight}{totallight} \\ &= \frac{intraocularscattering \cdot contactlensscattering}{totallight} \\ &= [intraocularscattering]\frac{contactlensscattering}{totallight} \\ &= [intraocularscattering] \cdot SR_{contactlens} \\ &= [intraocularscattering] \cdot (n-1)SR_{step} \end{aligned} \tag{6.15}$$

Where n indicates the contact lens number. Since we varied the concentrations of microspheres in the contact lenses proportional to the lens number, we propose a proportional variation of SR with increasing lens number. Ignoring the contribution of the non-scattered light over measured area (5-10 degrees), the corresponding $\log(s)$ value measured by the C-quant can be calculated as follows:

$$\begin{aligned} \log(s_{total}) \quad &= \log(s_{intraocularscattering} \cdot s_{lensscattering}) \\ &= \log(s_{intraocularscattering}) + \log(n-1) \end{aligned} \tag{6.16}$$

Six eyes from three subjects were examined by the C-quant, wearing the set of different contact lenses. To avoid a contribution of tear-film breakdown during the measurement, the contact lenses were selected randomly and a baseline exam was repeated after examining all contacts. We did not observe a significant increase of straylight before and after wearing the lenses. Figure 6.13 shows the $\log(s)$ values for each subject using the different contact lenses. Comparing these results with the $\log(s)$ values derived from the (age related) glare spread function shown in figure 6.12, we can conclude that objective psychophysical measurements of healthy young subjects wearing the scattering contact lenses reveal that the amount of increased light scattered over angles ranging from 5 to 10 degrees in the calibrated scattering contact lenses is similar to the amount of increased light scattering addressed to the ageing eye.

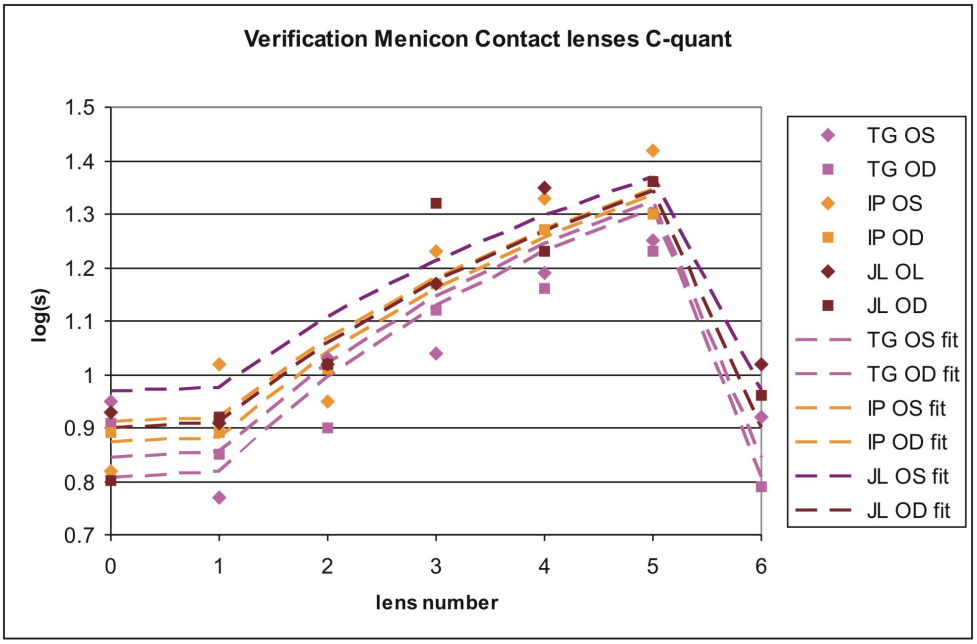

Figure 6.13: Log(s) parameter for use of different contact lenses

Chapter 7

Optical Methods for Measuring Light Scattering in the Cornea

The previous chapter gave an overview of a range of optical methods for measuring light scattering through a scattering medium. All the described methods were based on the *single pass* principle, scattered light was measured when it passed a scattering plane exactly once. This principle is not valid for scattering measurements in the living eye. To make such measurements, we should be able to place a camera or a light source inside the eye. Therefore, it is more appropriate to use *double pass* techniques for measuring scattered light in the eye. In such a setup, the light passes the scattering plane twice on its optical path. In this chapter, we present three techniques for measuring light scattering in the cornea.

7.1 Single pass scattering measurements in excised rabbit corneas

The most fundamental method for optical measurement of corneal scattering is to design an optical device looking *through* the cornea. This setup, where an object is directly imaged through a scattering medium without any reflective surfaces, is called a single pass method. Since it is not possible to insert a light source or an objective detector behind the cornea, this is an in vitro measurement of scattering on excised corneas. In our study [3][1], we used the rabbit eye model, which has similar properties as the human cornea (see chapter 3) to evaluate the scattering properties of corneal haze following photorefractive treatments (PRK).

[1] March 2008, Accepted for publication, Journal of Optometry and Vision Science

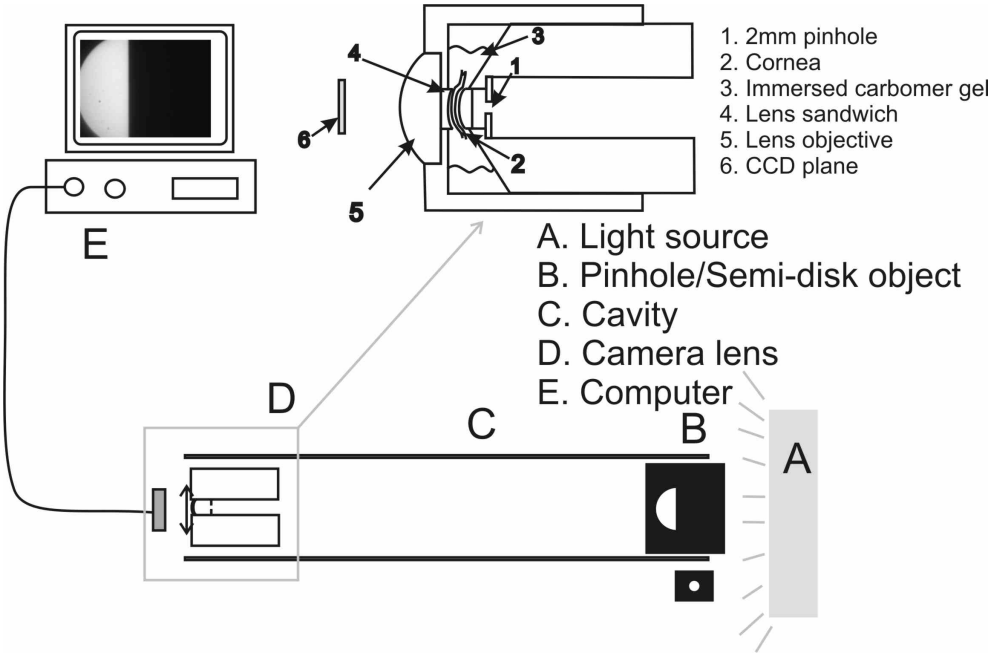

Figure 7.1: Schematic of the optical setup used in the single pass experiment. Down: entire optical system used. Upper right corner: Detail of the camera lens with the excised cornea

7.1.1 Experimental Procedure

Optical setup

Regarding the findings of the single pass measurements obtained in chapter 5, we image a uniform illuminated half field object through a camera objective where the excised corneas are sandwiched.

A purposely- constructed optical setup was employed for the evaluation of narrow-angle forward scattering. The setup is illustrated in figure 7.1. It was composed by a CCD camera (sony XCD-X700) using a custom-made camera lens and two different light sources serving as objects. The camera lens consisted of one plano-convex and one plano-concave element. The refractive surfaces of the lenses had curvatures similar to the anterior and posterior curvatures of the rabbit cornea respectively. The excised cornea occupied the space between the lenses. Carbomer gel 0.3% (Thilogel, ALCON Hellas AEBE) was used to facilitate optical contact between these three elements. An additional plano-convex lens (also optically coupled with carbomer gel) was used to adjust the total dioptric power of the camera lens to approximately 35 diopters.

All lenses were aligned using a custom-made lens mount that ensured that the optical elements were properly centered. Although optical aberrations were not measured, ZEMAX simulations (ZEMAX Development Corporation Bellevue, WA) predicted that the objective would be relatively sensitive on tilt. In order to minimize the impact of aberrations a 2mm diaphragm was introduced in front of the lens. For each cornea, a point source (back - illuminated $500\mu m$ pinhole) at a distance of 25cm was imaged through the camera objective. Each image was constructed by adding two separate images acquired using two different exposure times. The first image, (short exposure) was used to image the intensity of the point source itself while the second (long exposure) was used to image the scattered light. Each image was corrected according to the camera's calibration curve (figure 5.10 (determined section 5.3), and finally the two separate images were registered and the saturated pixels of the long exposure image were substituted by the corresponding pixels in the short exposure image (multiplied by the ratio of the exposure times). This technique allowed us to effectively extend the dynamic range of the camera by two orders of magnitude. The compound image for each cornea was used to estimate the angular distribution of scattered light (see section 7.1.2) Additionally, a uniform illumination semi-disk was imaged using each cornea. The exposure time was controlled in order to utilize the full dynamic range of the camera. The images acquired using the semi-disk were used to calculate the power ratio of scattered light as the ballistic ratio introduced in section 4.3.2.

Image acquisition and processing

A semi-disk was formed by a translucent disk with a radius of 2.7 degrees occluded by a knife-edge through the center of the disk. The object was back-illuminated with a uniform white light source. Initially, a simulated image was generated, convolving the semi-disk with the 2mm diffraction limited point spread function. This simulated image corresponds to the image on the CCD in absence of scatter. Further, it was convolved with the scattering PSF experimentally determined (see further in section 7.1.2). This simulated image corresponds to the image on the CCD if each photon was scattered exactly once. Following equation 5.7, a set of 100 calculated images was generated as a weighted sum of the above-mentioned scattered and not-scattered

simulated images for varying BR from 0.01 to 1. The experimentally acquired semi-disk images (through each cornea) were cropped to a rectangle in the occluded field starting at the knife-edge border and averaged across the direction perpendicular to the edge. Like this, 2-degree step response was calculated starting from the knife-edge towards the periphery of the occluded field. This response was compared to the response of the simulated images previously described. The value of BR used in the simulated image that best matched the experimental image (minimum RMS difference) was used to characterize each cornea. All analysis and simulation was done in Matlab (The Mathworks, Inc.)

Animal treatment

Twelve eyes of six pigmented adult male rabbits, weighting 2.5-3.5 kg were used in the study. The animals were treated in accordance to the guidelines of the Association for Research and Vision in Ophthalmology Statement for the Use of Animals in Ophthalmic and Vision Research. For surgery (PRK), the animals were anesthetized by an intramuscular injection of a mixture of xylazin hydrochloride (5mg/kg) and ketamine hydrochloride (50mg/kg). An eyelid speculum was introduced and two drops of topical anesthesia (sodium chloride proxymetacain, Alcaine, ALCON Lab, Hellas) were instilled. Two minutes after topical corneal anesthesia, mechanical epithelium debridement of the central 6 mm of the cornea (previously marked with a 6 mm trephine) was performed with a brush followed by a myopic photoablation performed using a 193nm Excimer laser (Wavelight Allegretto 400 Erlangen, Germany) operating at an average fluence of 180 mJ/cm2 per pulse and a repetition rate of 400 Hz. The ablation pattern delivered to all eyes was programmed for -4 diopters (D) at an optical zone of 6 mm, removing approximately 49 mm of stromal tissue in the centre of the ablation zone. Antibiotic ointment (Tobramycin 0.3%) was administered to all eye four times daily until re-epithelialization was complete. As the purpose of this study was to evaluate corneal haze, no topical steroids were applied since their action would minimize haze formation.

Seven weeks after treatment, all eyes were evaluated for haze by means of slit lamp examination by a refractive surgeon (GDK). All corneas were evaluated by HRTII (Heidelberg Engineering, Germany) CFM prior to surgery, and at weeks 1, 2, 3 and 7 after surgery. Immediately after the CFM imaging on week 7, all animals were sacrificed and eyes were enucleated. In order to maintain normal hydration conditions, corneas were excised along with a 2 mm scleral rim. Forward scattering was assessed using a single-pass device presented in the previous paragraph. Finally, all corneas were prepared for histologic examination (light microscopy) by trichrom staining. Histological fixation of all specimens (with glutaric aldehyde) was made within 5 minutes after enucleation

7.1.2 Results

Estimation of Scattering Distribution

Figure 7.2a shows the image of the point source through four different corneas with different amounts of scatter. The central portion of the image (involving the directional light) is saturated. In all images, exposure was identical and adjusted to visualize the glare and the fine needles originating from the center and gradually fading towards the periphery. These needles correspond closely to the ciliary corona as described in chapter 4. This model was based on the wavefront analysis through a scattering medium involving the conservation of the coherent properties of the scattered light. In our study, we applied a simplified model of non-coherent light scattering from small particles as described in section 4.3.2. In this approximation, all scatterers are modeled as perfect spheres with a given radius and refractive index. As the variation of particle sizes has a much bigger impact on the scattering distribution than the wavelength, we simulated the scattering PSF using a wavelength of 600nm. The scattering model takes into account the ratio of the refractive index of the spheres to the refractive index of the background matrix and the particle size. These parameters were initially set based on the corneal stroma irregularities (fibroblasts, and other reflective structures) that were observed using confocal microscopy. Following an initial estimation of the forward scatter distribution based on images of point sources (figure 7.2), the average

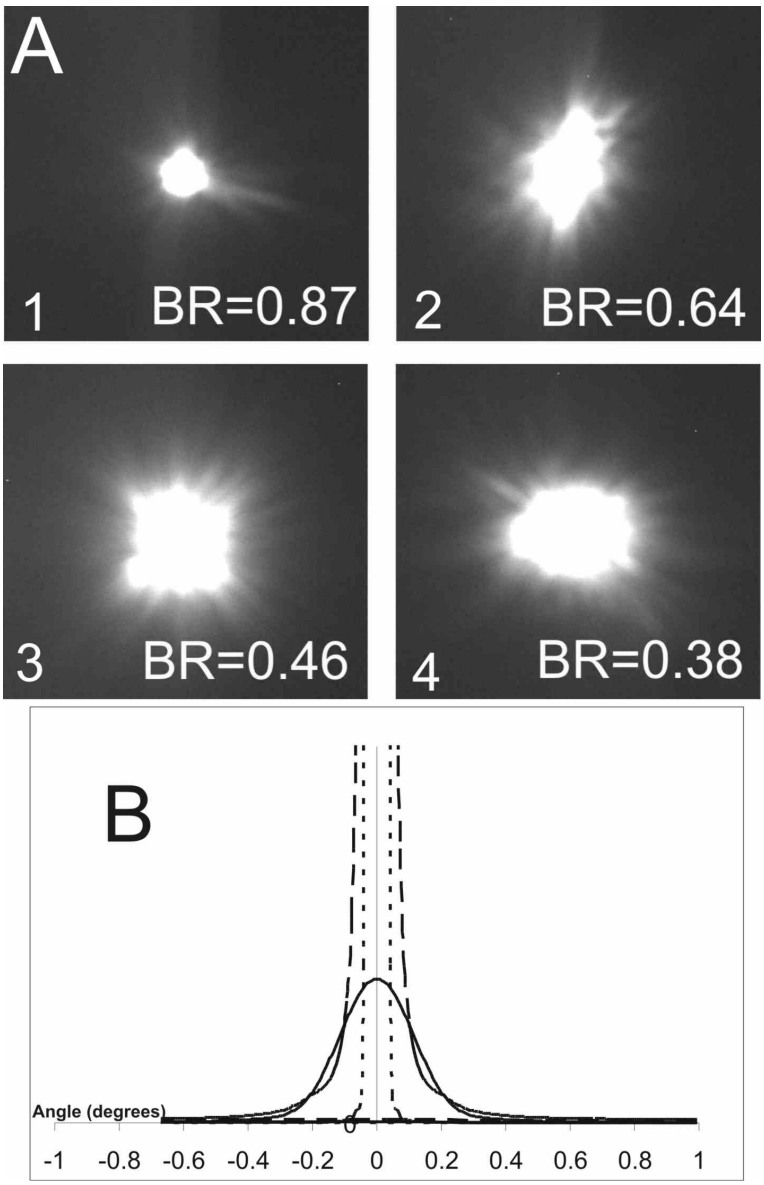

Figure 7.2: Images of scattering PSF for different levels of scattering (BR). Field: 2X2 degrees (a). Radial averaged profile of computed and measured PSF. Dashed line: average of all measured images, Dotted line: Radial profile for diffraction limited PSF (directional light), full line: Radial profile of Scattering Distribution (all scattered light) (b) Horizontal axis is degrees.

size, BR and refractive index of the particles were optimized in order to reproduce the scatter function obtained experimentally from the semi-disk images (see section 7.1.2). Optimization was performed by minimizing the RMS difference between the model and the experimental semi-disk images in a field of 2 degrees around the edge of the disk. Optimal fit was obtained for a particle size distribution of $36.7 \pm 15\mu m$ and a relative refractive index of 1.0024. The fit obtained is shown in Figure 7.2b.

Accuracy and repeatability of the method

Preparation of the samples When measuring excised corneas, the optical quality of the sample decreases over time due to edema. The preparation of the samples is a detrimental step for repeatable measurements. Applying too much strain on the sample can lead to deformation of the sample causing visible striae. Therefore, mounting of the sample is a process that cannot be easily tested for repeatability as each positioning would lead to accumulated defects.

Repeatability of the optical setup To get an idea of the resolution and repeatability of the optical setup, we evaluated the optical (and image processing) part of the technique by means of a series of ten consecutive measurements estimating light scattering on a -previously characterized- calibrated scattering contact lens (we connected two samples of lens 5, see chapter 5). As a result, we obtained a BR of 0.75 and a standard deviation of 0.04.

Accuracy of the algorithm The analysis is based on an algorithm that searches the similarity of a measured scattering profile of a cornea with a set of simulated profiles based on their RMS difference. The accuracy can be estimated by the residual RMS of the best fit. On the exception of one eye, this residual RMS was average 0.040 with a standard deviation of 0.035. We calculated that the residual RMS is not dependent on the BR, which certifies the validity of the scattering model. Moreover, we evaluated the RMS minimization algorithm with a simulated scattering profile (instead of an acquired profile from a cornea). Evidently, the minimum residual RMS was 0. The residual RMS reached the value 0.040 for values BR+0.06 and BR-0.06. Therefore, we

can quantify the accuracy level 0.06 (see 'accuracy span', figure 7.3), which is in the same order of magnitude as the repeatability. Below, we inserted a figure to illustrate the accuracy model we applied.

Correlation of BR with clinical haze

Corneal haze (see section 2.2) was assessed by the same investigator immediately before the animals were sacrificed. The calculated BR for each cornea is plotted against the subjective haze grade in figure 7.4. A negative correlation between these parameters (Pearson's Coefficient = -0.23) was found suggesting the relation between increased forward and backward (clinically observed) light scatter (haze). This finding suggests that corneas characterized by increased forward scatter tend to express higher clinical haze.

Additionally, the single pass method has been applied and correlated with clinical haze in another protocol. Corneal haze was evaluated by another refractive surgeon (DB). An interesting finding is shown in figure 7.5. The values of BR we obtained were very similar in both protocols, however the haze was assessed to be more clear by one clinician (DB). This could be the result of the subjective origin of the haze grade suggesting variations of the parameter between different clinicians.

Correlation of BR with Histological evaluation

Histology was performed on all eyes at week 7. Representative structures observed on the stained samples are shown in figure 7.6. The main histological finding in all eyes was subepithelial scar tissue which had also observed in confocal microscopy. However, histology sections allowed the examination of larger areas on the cornea. The scar tissue consisting of both newly formed and unorganized collagen and activated keratocytes seems critical for the development of corneal scatter postoperatively.

Based on approximately ten pictures for each corneal sample, the relative thickness of the scar tissue layer was measured. The relative thickness of the scar tissue was correlated (Pearson's coefficient =-0.79) to the ballistic ratio previously estimated for each sample (figure 7.7). This finding suggests that a thicker scar tissue layer results

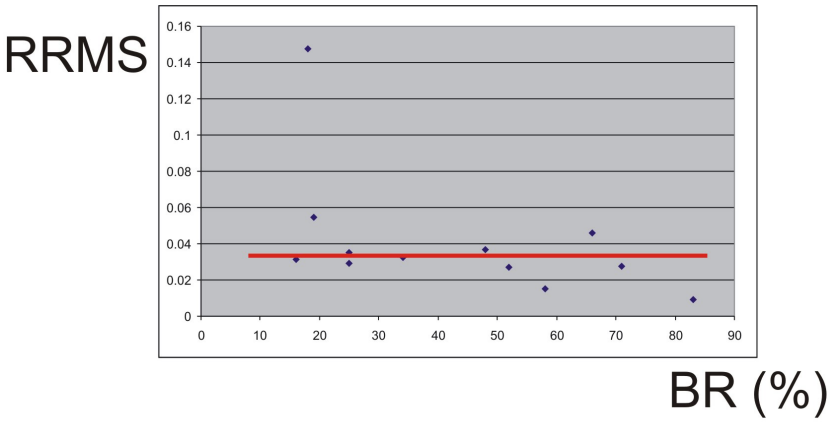

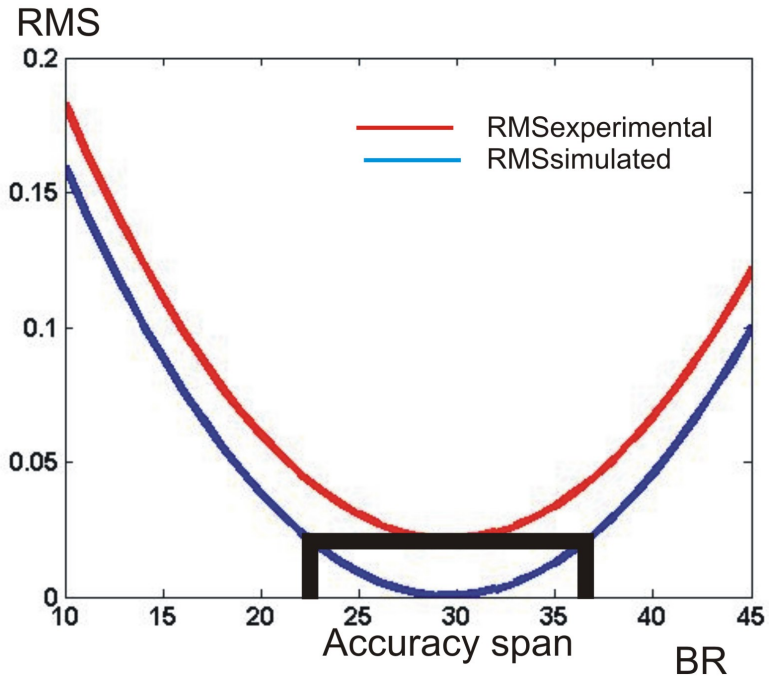

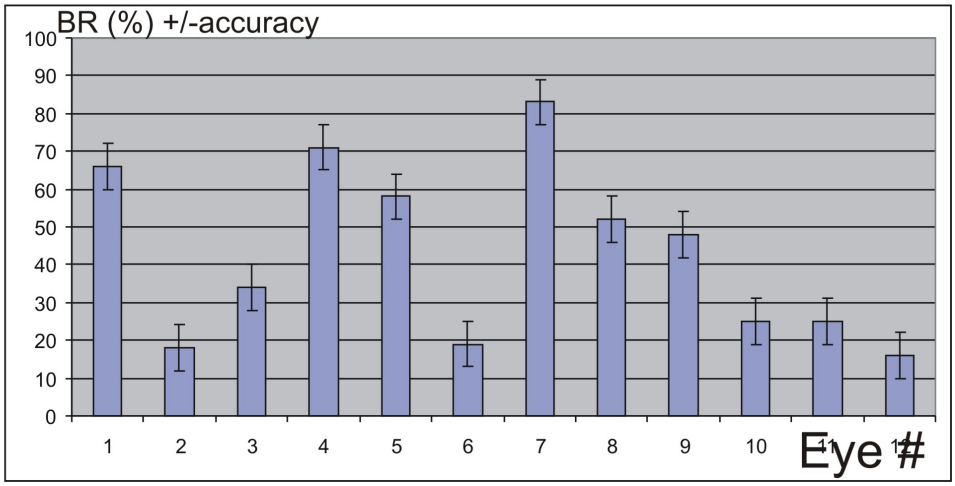

Figure 7.3: Accuracy of the RMS algorithm

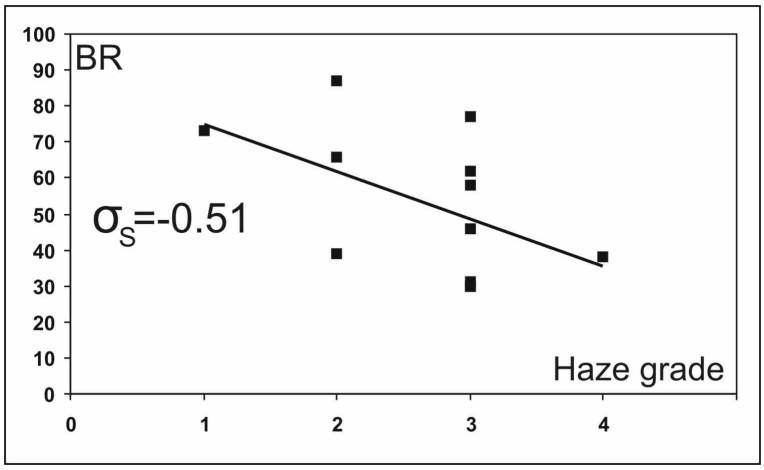

Figure 7.4: Comparison of BR with haze grade. Note that all eyes had a high haze grade.

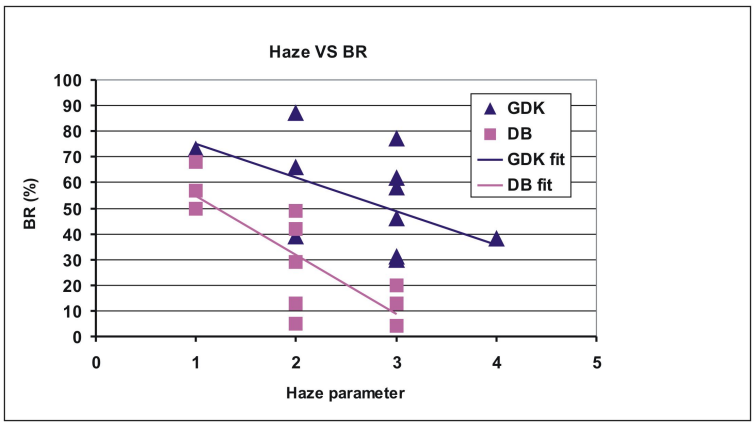

Figure 7.5: Comparison of BR with haze grade. Outcomes of two protocols where haze was assessed by a different clinician

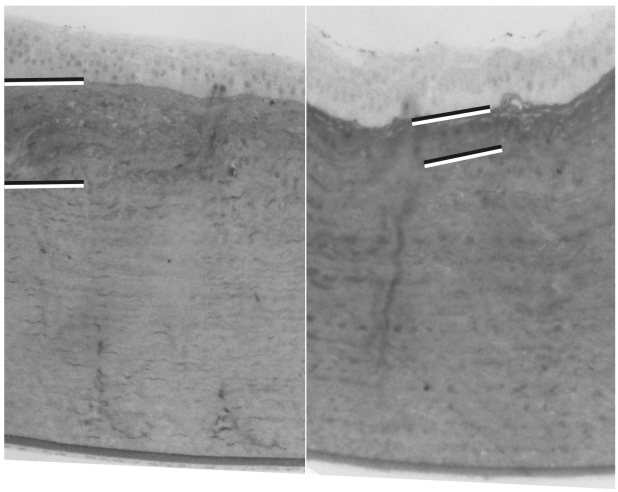

Figure 7.6: Representative images of histological analysis. Different thicknesses of the scar tissue are indicated.

in increased forward light scattering (lower BR).

Two corneas were excluded from this analysis as no suitable histological photographs could be obtained.

7.1.3 Discussion

Our results suggest that the intensity distribution of scattered light on the cornea is characterized by a narrow forward distribution. Several scattering models can be applied to approach the obtained experimental distribution. We optimized a model based on scattering on small spherical particles, varying the size distribution of the scattering spheres to match the scattering distribution with our experimental findings. Since we were interested in quantitative measurements of forward light scattering, optimization of other free parameters in the model, such as relative refractive index and spectral distribution, were out of the scope for this study. However, the characteristic size of the scatterers in our model ($36.7 \pm 15 \mu m$) reproducing the experimental scatter distribution for polychromatic light, suggests that the main cause of scattering in the post- ablation cornea is the subepithelial region, characterized also by irregularities of that scale. The irregularities in this region (typically 50 microns deep) are extracellular

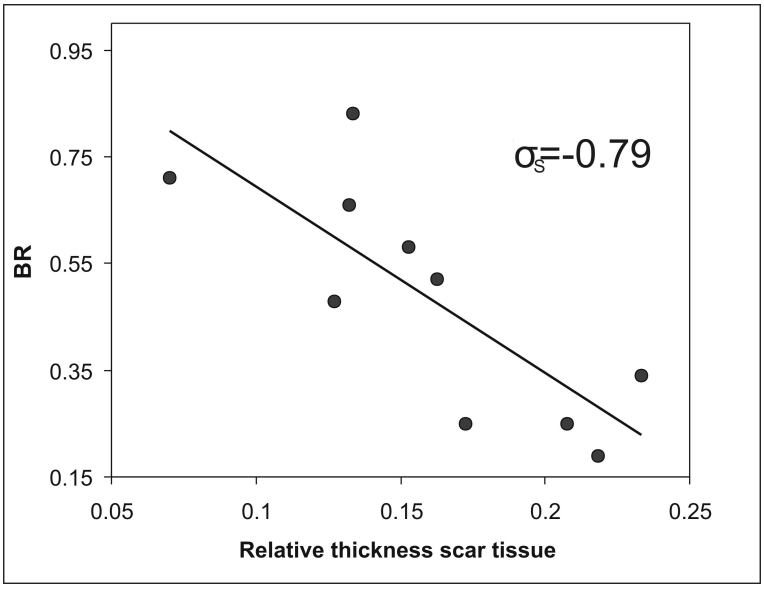

Figure 7.7: Comparison between BR and relative thickness of scar tissue. σ_s: Pearson's correlation coefficient.

reflective structures characteristic of scar tissue. The hypothesis that this layer is the main cause of scatter is further supported by the strong correlation of it's thickness with the calculated BR and subjective haze.

7.2 Double pass measurements by analysis of Tscherning images

When measuring light scattering in a double pass technique, the light needs to be reflected by a surface inside the eye. The most trivial reflective layer is the retina. Especially for older subjects, light scattering on the cornea and the crystalline lens give rise to a significant reduction of the image quality when imaging a light pattern projected on the retina. The goal of the double pass technique is to quantify the image quality of a light pattern projected on the retina, imaged on an intensified CCD camera.

7.2.1 From aberrometry to scatterometry

In the previous section 2.2.3, we pointed out the close relationship between ocular scattering and ocular aberrations. We proposed to model light scattering as a case of very high aberrations, with spatial frequencies of the order of the scattering particles. Moreover, ocular scattering and aberrations are documented as two significant sources for loss of the retinal image quality. Therefore, it could be of use to implement a method for measuring ocular scattering in an aberrometer.

The ray tracing wavefront sensing techniques have the goal of imaging one or more point sources on the retina. The image quality of each spot depends of the amount of light scattered on the lens and the cornea. Whereas optical aberrations can be derived from the *positions* of these points on the image, analysis of the *shape* of each PSF can give us information on the amount of light scattering in the eye.

7.2.2 Restrictions for scattering analysis on double pass images

To decide which of the above-mentioned aberrometers is best suited for quantification of scattering in the eye, we should take following restrictions in consideration:

The effect of aberrations on the PSF

Since we are ideally imaging point sources, the image of these points are characterized by the PSF. When taking scattering into account, the PSF is a partial convolution of the optical PSF and the scattering PSF:

$$PSF_{total} = BR \cdot PSF_{Optical} + (1 - BR) \cdot PSF_{Optical} \bigotimes PSF_{Scattering} \tag{7.1}$$

The optical PSF is both affected by the aberrations of the eye and the diffraction limited PSF of the optical system. The effect of aberrations can be minimized when imaging through a small diaphragm, optimizing the eye's optics to a diffraction limited system. This is not necessarily impossible when we want parallel measurements of the eye's aberrations. The Hartmann-Shack system can be optimized by illuminating the

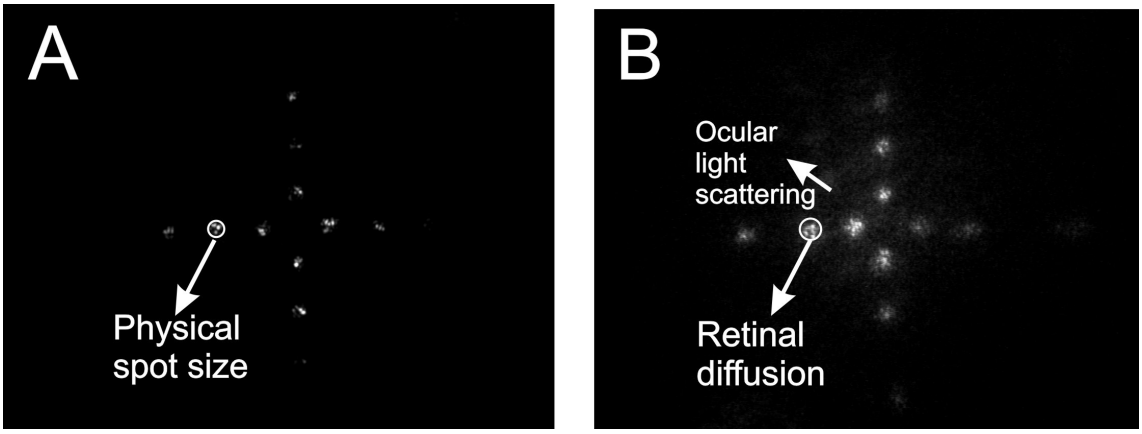

Figure 7.8: Left: Tscherning image of a (not scattering) model eye, no retinal diffusion. Right: Tscherning image of a PRK subject, 3months after treatment

retina through a small pupil, whereas the Tscherning and Ray-Tracing system can image the retina through a small pupil. In the Hartmann-Shack setup however, the optical PSF is affected by the diffraction limited PSF of the microlenses (section 2.1.2. Bueno et al. [4] described a double pass setup where the depolarization effects of light scattering are used to separate the scattered light on the CCD.

Corneal and lens reflexes

A part of the light used to illuminate the retina is refracted on the refractive surfaces of the eye. These reflections give rise to the so called *purkinje images*, which are described in more detail in the next section. When the propagation of these purkinje images coincides with the optics of the imaging system, the purkinje images give rise to significant artifacts on the CCD image.
To avoid these unwanted reflections, the illumination of the retina is usually partially occluded on the apex. In the Tscherning aberrometer e.g., the center of the mask does not have a subaperture to avoid a ray passing through the apex.

Retinal diffusion

Figure 7.8 compares on the left a Tscherning image recorded with an artificial, no scattering model eye. On the right is shown a Tscherning image of the eye of a PRK subject, 3 months after treatment. Considering the central broadening of the spots

in the human eye to be scattered light on the cornea or the crystalline, the values for BR would be unreasonable low. Therefore, we assume this central broadening should be addressed to retinal diffusion as previously described in section 2.2.1. Since it is suggested that the retinal diffusion can depend interindividually on factors like pigmentation, corneal light scattering should be measured in a follow-up study, including the preoperative date to be valid as an objective measurement of increased corneal light scattering after refractive surgery.

The Stiles-Crawford effect

The cone photoreceptors in the fundus have a directional selectivity for the light traveling through the cones. Stiles and Crawford [33] were the first to report a higher sensitivity of the cones for light entering the eye through the center of the pupil than for light entering the eye in the periphery of the pupil. This effect, the *Stiles-Crawford effect* is addressed to the directionality of the cones towards the center of the pupil. It also leads to a reduced retinal reflectance for light passing through the periphery in the pupil. For the Tscherning setup, this effect is minimized in the imaging arm by conjugating a small diaphragm to the eye's pupil ensuring that all light on the CCD has been directed through the center of the pupil. In the aberrometer arm of the setup, the different spots enter the pupil through different positions. Figure 7.9 illustrates the stiles-crawford effect for Tscherning images using a cross-like mask.

Cross-scattering: The relative position of the spots on the CCD

The spots projected from the cross mask on the retina are separated for about $110\mu m$ on the retina, corresponding to approximately 30 minutes of arc in the visual field. The observations from the single pass setup described in the previous section suggest the with of the scattering distribution to be approximately 40 minutes of arc (FWHM). The light scattered from one beam will also affect the periphery of the neighboring spots on the Tscherning image.

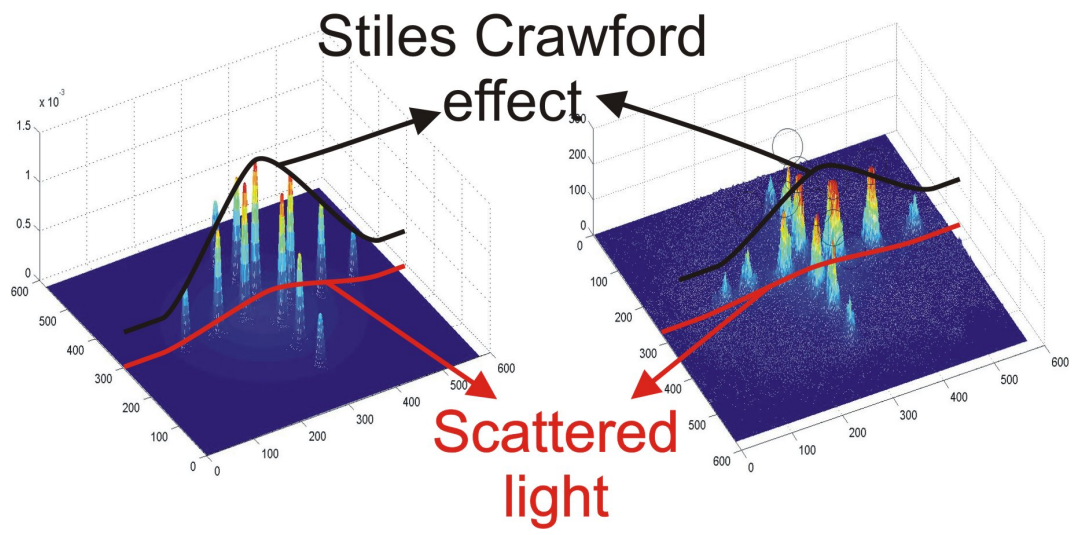

Figure 7.9: The impact of the Stiles Crawford effect on Tscherning images. Left: Simulated data, Right: Experimental images

Speckle noise

When using a coherent light source, retinal images are strongly affected by speckle noise. This noise is associated with interference of the light reflected on a rough surface, such as the retina. Speckle noise can be eliminated when using a non coherent source or *breaking* the coherence using a fast moving diffusor so the speckle variations are integrated during the exposure of one image. Another method to reduce the effect of speckle noise is to average a set of separate images. Moreover, this allows us to enhance the dynamic range of the images. Averaging a set of 4 images taken with an 8-bit CCD will give us 1024 grayscale levels instead of 256. Given the complexity of the first two methods, we decided to average a set of four images.

7.2.3 Optical Setup

We modified a Wavelight Allegretto Tscherning aberrometer by replacing the aberrometer mask. The setup is illustrated in figure 7.10. A parallel beam is created from a 660nm diode laser collimated through a telescope lens. A mask with multiple aperture selects a set of parallel beams. All apertures in the mask have a $500\mu m$ diameter. Two different masks have been selected, a cross-like mask with 12 spots and a mask where 8 apertures are spaced on a ring. All points are equally separated. To reject the corneal

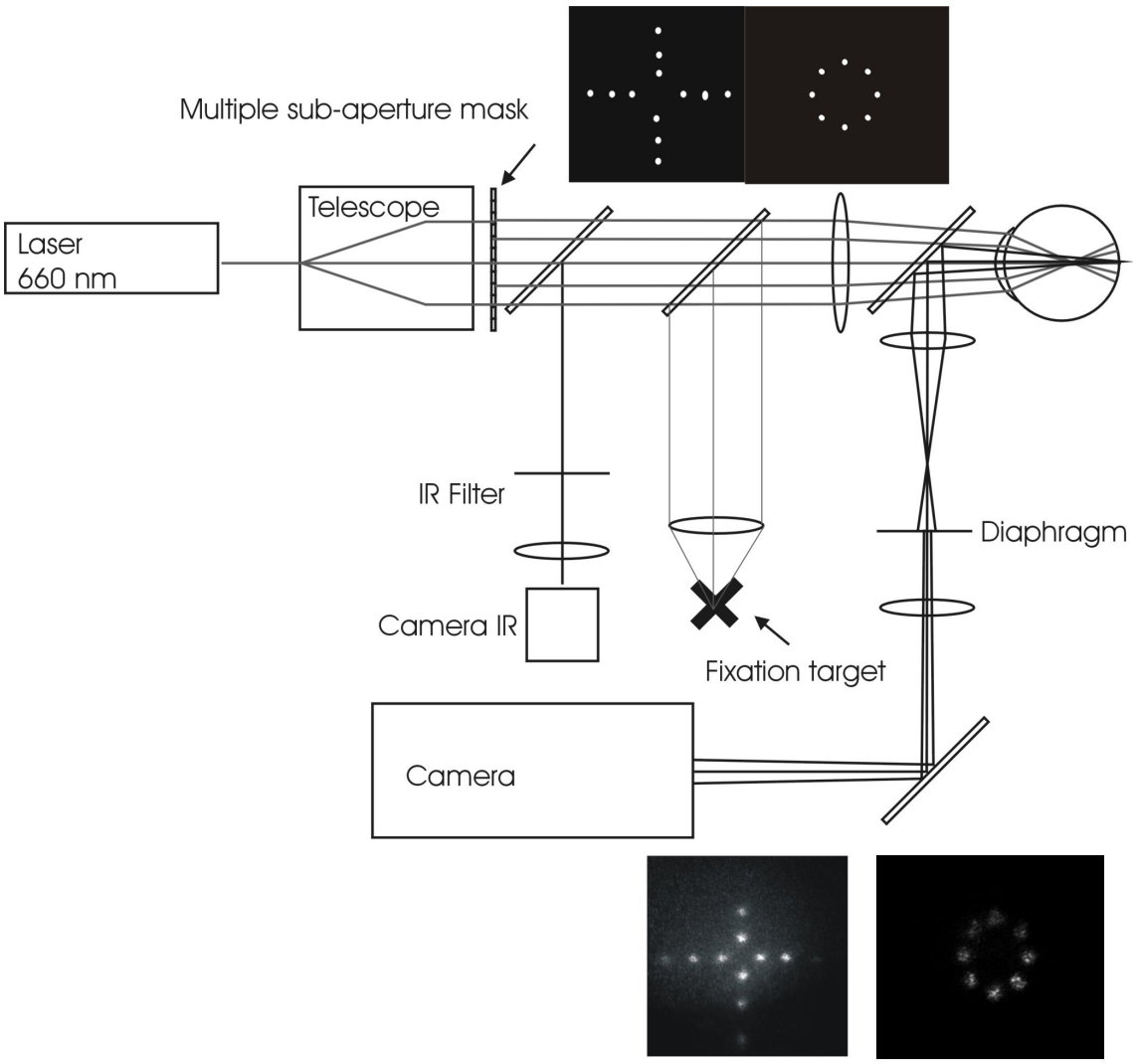

Figure 7.10: Schematic diagram of the used Tscherning device

reflex, the center of the mask is occluded. The beams pass through a converging lens system of +10D and cross before the retina to form a diffraction limited spot pattern similar to the mask. A fixation target and pupil monitor permit alignment of the eye along the optical axis. The retinal spots are imaged on an intensified 8-bit CCD camera through a 1.5 mm aperture which is conjugated to the corneal plane. This allows us an approximation of diffraction limited imaging even in the presence of any aberrations. The image recorded on the CCD corresponds to a 4 by 5.5 degrees field on the retina. The gain of the CCD was fixed for all images and selected that no pixels in the images were saturated. This allowed us to make quantitative measurements of scattering. A set of four separate images is averaged to reduce the effect of speckle noise.

7.2.4 Image processing

After averaging, the images were processed to extract the scattering information in the image. A Matlab algorithm was written for both the cross-pattern images and the ring images.

Centroiding algorithm

In a first step, the center of the spots was calculated. Even though the averaging of four images significantly reduced the effect of speckle noise, it was still affecting the center of the spots. Consequently, the pixel with the maximum intensity in the image does not necessarily correspond to the centroid of the spot. For this reason, we employed a centroiding algorithm that searched for the "center of mass" in the spot to estimate the centroids. The center of the spot was calculated with the following equation:

$$\vec{r_{center}} = \frac{\sum I(\vec{r}) \cdot \vec{r}}{\sum I(\vec{r})} \tag{7.2}$$

Where $I(\vec{r})$ corresponds to the intensity of pixel $\vec{r}$.
After centroiding, a radial profile was calculated for each spot by integrating the radial cross section around the centroid. To reduce contribution from neighboring spots in the periphery of the profile, profiles were cropped to 21 minutes of arc around the

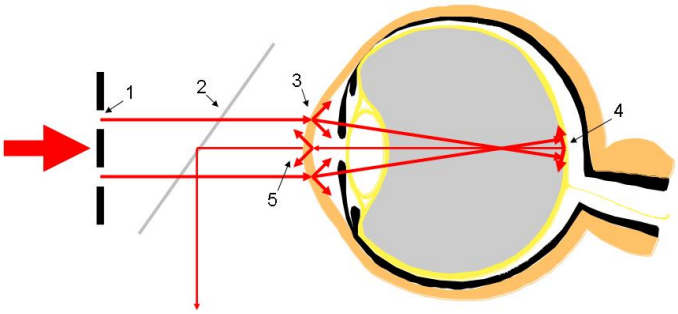

Figure 7.11: Broadening of the spots in Tscherning images. 1. Diffraction on the mask 2. Diffraction limit of the optical setup 3. First pass light scattering on the cornea and crystalline lens 4. Light diffusion on the retina 5. Second pass light scattering on the lens and cornea.

center.

scattering analysis

Figure 7.11 gives an overview of the optical effects that affect the profile of the spots on the CCD. Each effect is characterized by its PFS on the CCD. The final image on the camera is a convolution of all the PSFs described:

$$\begin{aligned} PSF_{CCD} = & PSF_{mask} \bigotimes PSF_{optics} \bigotimes PSF_{Scatter1stpass} \\ & \bigotimes PSF_{retinaldiffusion} \bigotimes PSF_{Scatter2ndpass} \end{aligned} \tag{7.3}$$

PSF_{mask} is the result of the projection of the subapertures from the mask on the retina through perfect optics. It is a convolution of circular disk with a 500 microns diameter and the corresponding diffraction on the aperture. The magnification of the system projects a 500 microns disk on a disk with a diameter of 47 microns on the retina, corresponding to a visual angle of 10 minutes of arc. The diffraction PSF can

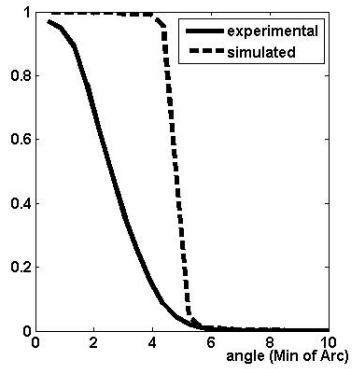

Figure 7.12: Experimental and calculated PSF of the projection of the mask apertures on the retina.

be described by the following equation:

$$PSF_{mask} \simeq [\frac{J_1(\frac{kl\theta}{2})}{\frac{kl\theta}{2}}]^2 \tag{7.4}$$

Where J_1 corresponds to a first order Bessel function. In the given configurations, the function should have a first minimum at 5.5 minutes of arc.
PSF_{optics} describe the optics of the Tscherning setup. The setup is optimized for imaging through a 2mm diaphragm (conjugated to the eye's pupil). Therefore, PSF_{optics} can be ignored compared to PSF_{mask} A model eye was used to experimentally verify the contribution of PSF_{mask} and PSF_{optics} on the final image. Both profiles are compared in figure 7.12. In the further processing, the experimental PSF will be employed.

PSF_{retina} is addressed on the retinal diffusion of the light. As discussed in section 7.2.2, the broadening of the spots due to the retinal diffusion can vary due to the pigmentation of the eye. A standard PSF was calculated based on a model described by Hodgkinson et al.[26]

The scattering information in the image is encoded in the $PSF_{Scatter1stpass}$ and $PSF_{Scatter2ndpass}$. Light scattering in the first pass is localized, each spot represents the scattering in the position where the beam enters the cornea and crystalline lens. Figure 7.11 shows that scattering from the second pass occurs in the center of the lens and cornea. Indeed, in the imaging system, a diaphragm is conjugated to the pupil

selecting only the central portion of the light coming through the lens and the cornea. Characterization of scattering is analogue to the algorithm described in section 4.3.2.

Cross pattern A set of 100 profiles was calculated corresponding to the PSF corresponding to a BR ranging from 1 tot 100 %. To reduce the complexity of the algorithm, BR was set identically for the first and the second pass.
After normalization of the profile from each spot in the Tscherning image, it was compared to the set of simulated profiles for different amounts of scattering. BR was calculated for each spot in the image searching the optimal match between measured and simulated profile using and RMS difference minimisation algorithm. The values for BR of the different spots were plotted on the corresponding positions in a corneal map. Finally, an interpolation algorithm created a scattering map visualizing the localized scattering on the cornea. The different steps in the scattering algorithm are visualized in figure 7.13

Ring pattern In the analysis with a cross mask, we only take into consideration the light scattered in an angle between 10 and 21 minutes of arc. However the single pass findings in section 7.1 reveal that a significant portion of the light is scattered over this arc, the relative intensity of the scattered light on the corresponding pixels of the CCD is very low compared to the intensity in the center of the spot. Moreover, speckle noise, scattered light from the neighboring spots and retinal diffusion have a significant effect on the accuracy of the technique. Also, the Stiles Crawford effect reduces the intensity of the peripheral spots resulting into unreliable data for in the periphery of the scattermaps.
To bypass the previous counterparts, we changed the pattern of the mask placing 8 subapertures on a ring. The apertures have the same diameter as the previous mask and the ring has a radius corresponding to a radius of 25 minutes of arc in the visual field. Scattering analysis with the ring mask is more straight forward. After the centroiding algorithm, an interpolated ring connects the spots to each other. The ring

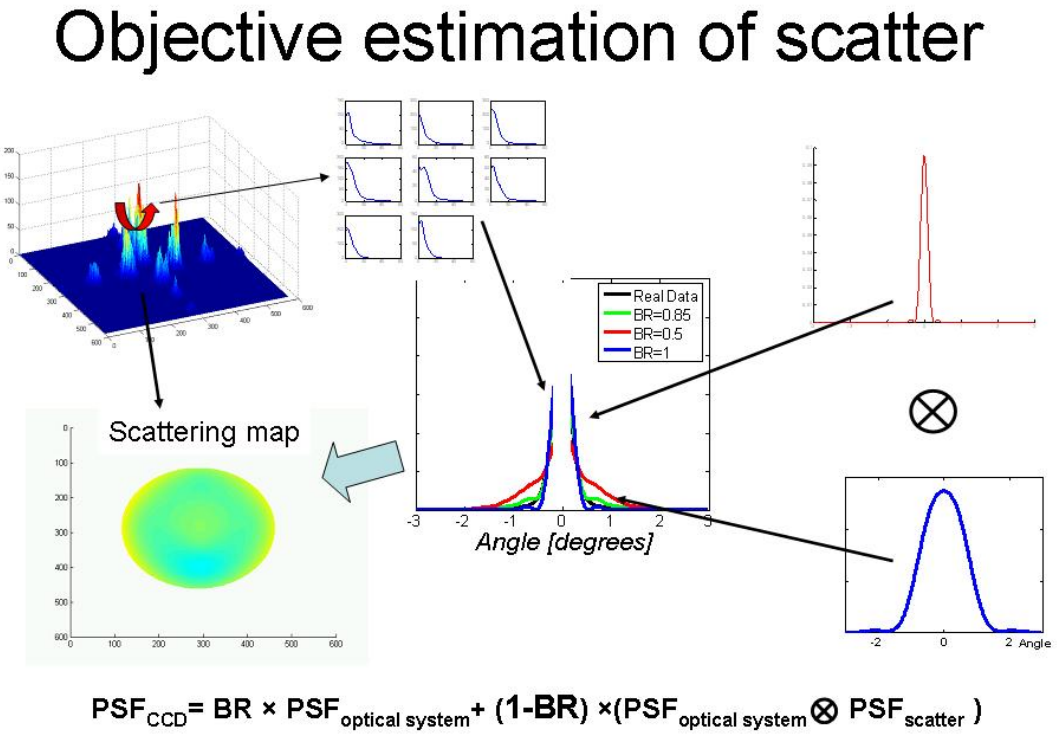

Figure 7.13: Visualization of the algorithm for estimation of scattering using Tscherning images.

has a thickness of 5.5 minutes of arc. Scattering Ratio (SR) is calculated as follows:

$$SR = \frac{1}{2}\frac{I_{center}}{I_{ring} + I_{center}} \tag{7.5}$$

Where I_{center} and I_{ring} correspond respectively to the total pixel intensity in the center of the ring and the pixel intensity in the ring. A factor $\frac{1}{2}$ is added since we have a double pass scattering experiment. The scattering ratio is converted to ballistic ratio as previously introduced:

$$BR = 1 - SR \tag{7.6}$$

The algorithm is illustrated in figure 7.14

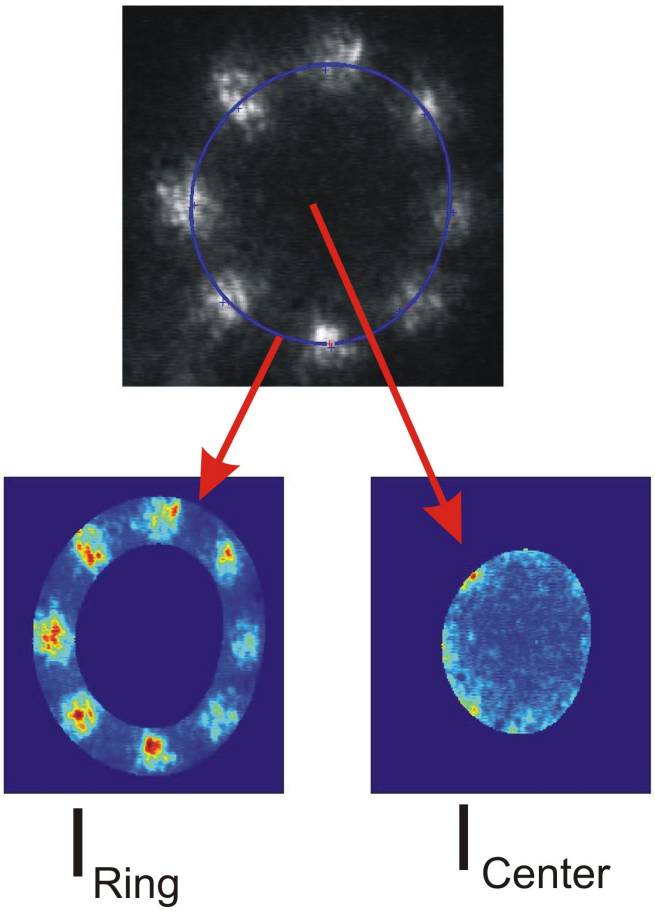

Figure 7.14: Scattering analysis based on the ring images

7.2.5 Patient protocol

Cross mask

Eighty six eyes of forty three patients that underwent refractive surgery for the correction of moderate (-1.75D to -8.25 D, Mean: 4.27 D) myopia were initially enrolled in this study. Laser photoablation was performed using the Wavelight Allegretto 4000 with a fluency of 180 mJ/cm2 per pulse at 400 Hz. 16 eyes underwent PRK, 21 epi-LASIK and 49 underwent a LASIK treatment. All patients received standard post-operative medication including Diclofenac sodium (0.1% four times daily) eye drops, a combination of topical dexamethasone and tobramycin (four times daily) eye drops for 2 weeks, and tear supplements for 8 weeks. Measurement of corneal scatter was performed preoperatively as well as at the one day, one week, 1 month, 3 months and six months postoperative intervals. The 1 day and 1 week exam of Epi-LASIK and PRK subjects was excluded from the study because of the re-epithelization. All eyes that were followed were free of complications with corneas appearing clear in standard slitlamp examination.

Ring mask

To verify the repeatability of the setup with the ring mask, three subjects (6 eyes) who used the previously described scattering contact lenses (see chapter 5) were measured with the instrument. To minimize the possible contribution of increased scatter due to the morphologic response addressed to the application of the contact lenses, the subjects used the lenses in a randomized order. A baseline measurement no contact lens) was taken in the beginning and at the end of the procedure.

7.2.6 Results

cross mask

For each eye, and at each stage of the healing process and preoperatively, we created a scattermap. This lead to a follow up chart visualizing the increased corneal scattering

addressed to the healing process following refractive surgery. A representative follow-up chart is shown on figure 7.15. Typically, the peripheral data points expressed a higher amount of scattering. As the localized variation of light scattering has never been reported, we believe that these findings can be related to artifacts addressed to the Stiles Crawford effect. Thereafter, the specific characterization of light scattering in each eye was done by averaging the value for BR in the central four spots. Figure 7.17 shows the results for the six-months follow up of our study. The high amount of scattering in the 1 day and 1 week post-op exam can be associated with edema caused by the laser ablation. The increased amount of scattering at one month after treatment can be associated with the highly reflective particles found in confocal microscopy associated with activated fibroblasts (keratocytes). It has indeed been reported that, one month after refractive surgery, the density of these activated fibroblasts reaches a maximum [45]. Figure 7.16 illustrates this possible correlation. Moreover, an interesting finding is illustrated in figure 7.18. If we plot 1-BR (a parameter proportional to the amount of forward scattering) in a graph, we see a correlation between the keratocyte density and 1-BR excluding the 1 day and 1 month data. The structural changes of the stromal tissue generated by the fibroblasts, generally described as scar tissue, decrease the degree of organization in the subepithelial layer and could cause a remanent amount of increased light scattering as observed in the 3 and 6 months post operative exams.

Ring mask

Figure 7.19 shows the results of the protocol of 6 eyes wearing a set of scattering contact lenses. We observe a significant decrement of BR in higher scattering lenses. The wide variability of the measurement can be associated with the propagation of tear film inhomogeneities around the contact lens. Moreover, a small reduction of BR between lens no.1 and lens no.5 was expected, the Tscherning device is able to detect scattering over small angles (approximately 6 to 50 minutes of arc). The single pass calibration of the contact lenses revealed similar values for light scattering in this angular range.

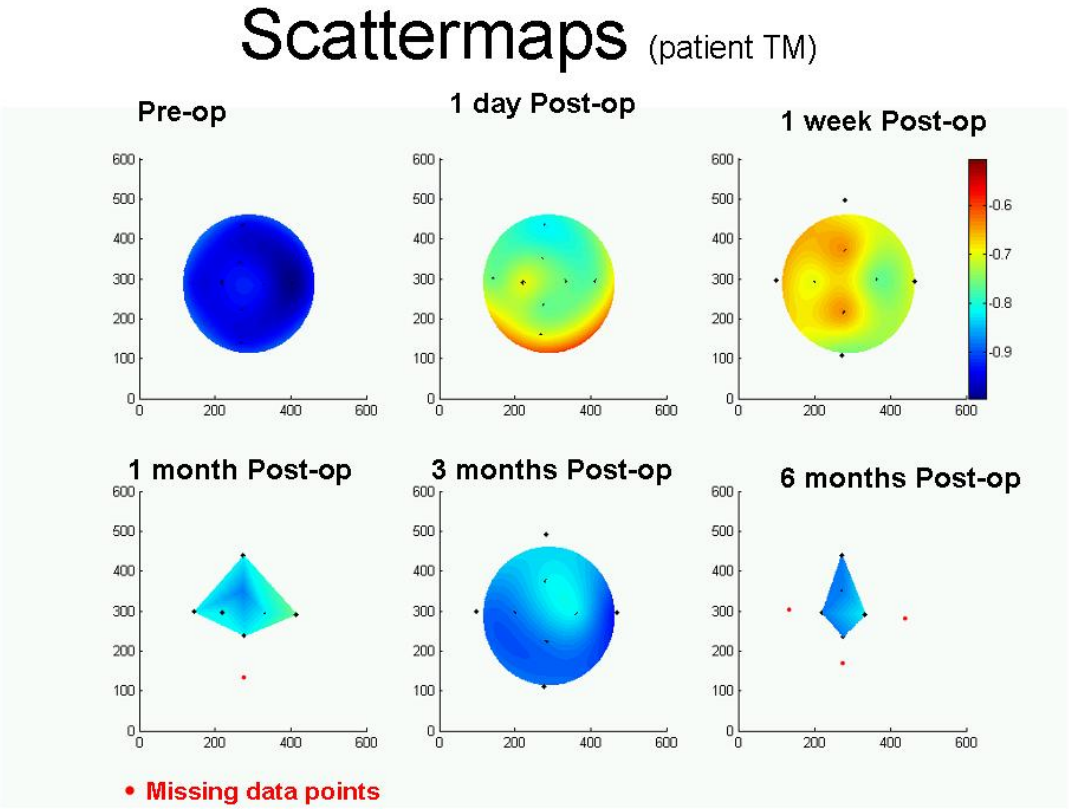

Figure 7.15: Representative scattermaps of a 6 months follow up after Epi-LASIK. Scattermaps were cropped to the central portion of the pupil when peripheral data where unavailable

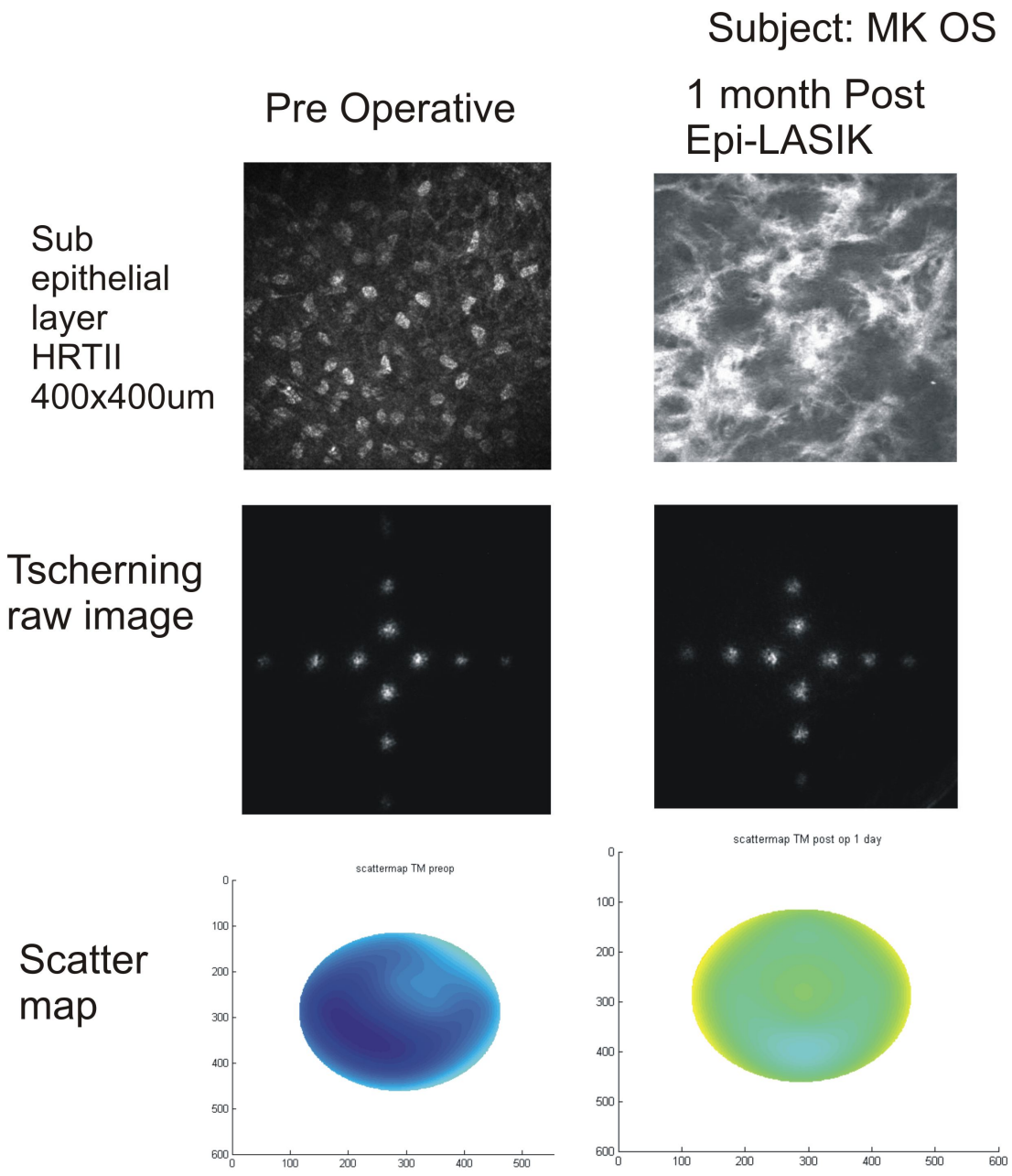

Figure 7.16: Comparison of preoperative and postoperative examinations of scattering analysis and confocal imaging of the subepithelial stroma. Note that in the preoperative and postoperative confocal images are taken under different gain settings. We observed higher reflectivity in the postoperative examination.

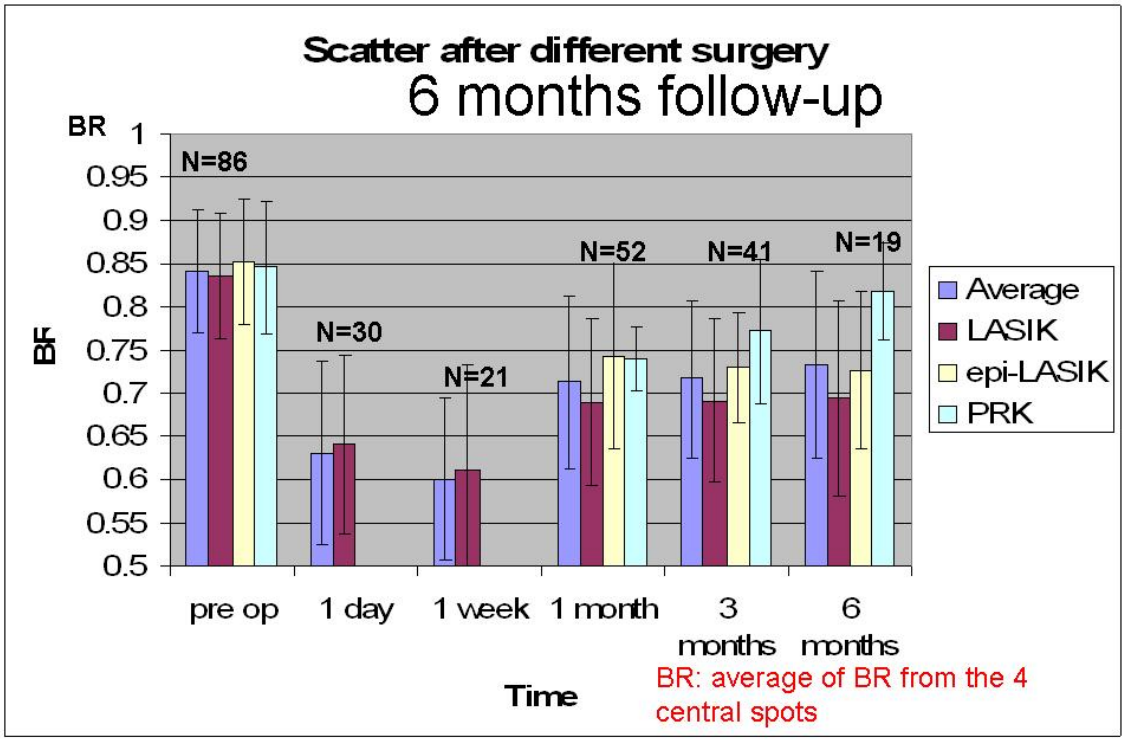

Figure 7.17: Statistical data of follow-up of 86 eyes undergoing refractive surgery. The number of eyes in each follow-up stage is indicated above each stage. The BR indicated the average of the BR for the central four spots in the tscherning image.

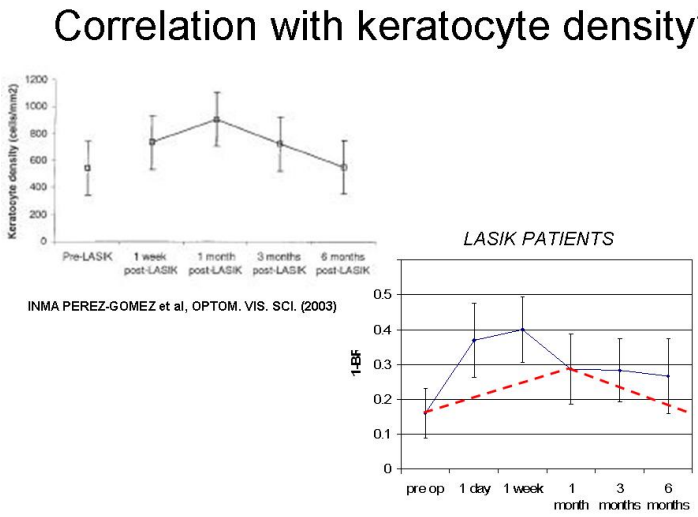

Figure 7.18: Comparison of scatter ratio (1-BR) and keratocyte density as reported by Perez-Gomez et al.

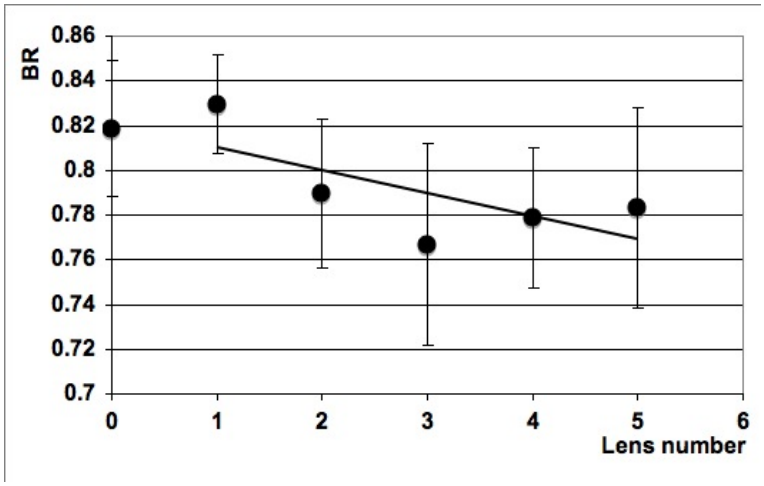

Figure 7.19: Double pass Tscherning scattering analysis using a ring mask. Average results of 6 eyes wearing the calibrated scattering contact lenses number 1(no scattering) to number 5 (strongly scattering).

7.2.7 Conclusion

In this section, we evaluated the measurement of light scattering by means of double pass Tscherning images. Both setups (ring mask and cross mask) allowed us to visualize the increased light scattering associated with either calibrated scattering contact lenses or corneal morphologic changes after refractive laser treatments. A significant shortcoming of the technique is the contribution of variable retinal reflectivity between different pigmented subjects. Limited access to control the (commercial) instrument obstructed us to make a profound study of contribution addressed to these interindividual variations (camera settings).

7.3 Double pass measurements by analysis of Purkinje Images

A third optical method for the measurement of light scattering in the anterior part of the eye we evaluated is based on image analysis of the fourth Purkinje image[2]. The fourth Purkinje (P_{IV}) image is the image formed by the reflection of the wavefront on the posterior lens surface. The method was first tested in an artificial eye and later in normal young eyes wearing customized contact lenses that induced different amounts of scatter. The research has been done in collaboration with Juanma Bueno

[2]Published in Optics Letters, December 2007

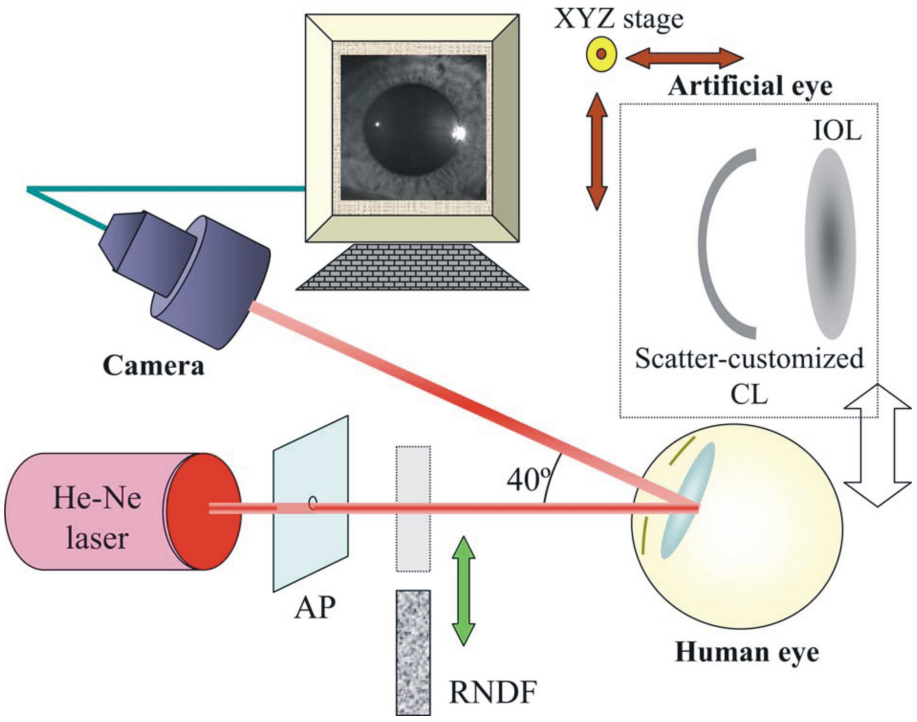

Figure 7.20: (Color online) Schematic of the Purkinje imaging system. AP, aperture to set the size of the beam reaching the eye (this filled the entire pupil). Other abbreviations defined in text. The artificial eye was mounted on translation stages to facilitate its alignment

[5] (University of Murcia, Spain).

7.3.1 Optical Setup

Figure 7.20 shows a schematic of the setup used to image P_{IV} in both artificial and human eyes. A 633 nm collimated $HeNe$ laser beam passes an artificial pupil (AP) and goes through a removable neutral density filter (RNDF, with an optical density of 1) used to modify the intensity of the incoming beam according to two different experimental conditions. In the registration pathway, a photographic objective conjugates P_{IV} with the plane of a CCD video camera. P_{IV} was slightly defocused on purpose to increase the dynamic range. During image acquisition, subjects were asked to fixate using their non tested eye to a target positioned in a manner to direct the measured eye towards the camera axis. This made the illumination and the recording pathways approximately 40 degrees apart in the horizontal plane and ensured P_{IV} to be distant enough from both the (much brighter) first Purkinje image (reflex on the anterior surface of the cornea) and the pupil edge (see figure 7.22).

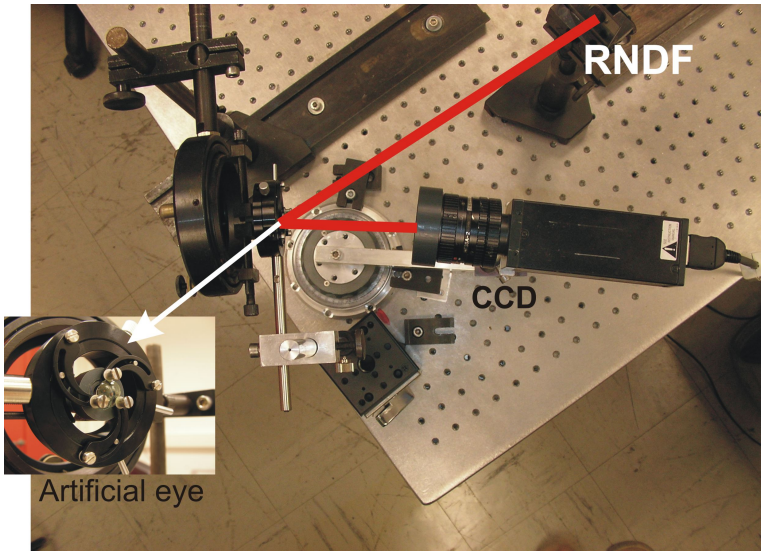

Figure 7.21: Laboratory setup of the Purkinje imaging system configured for the analysis of light scattering on the artificial eye consisting of a scattering contact lens and an IOL

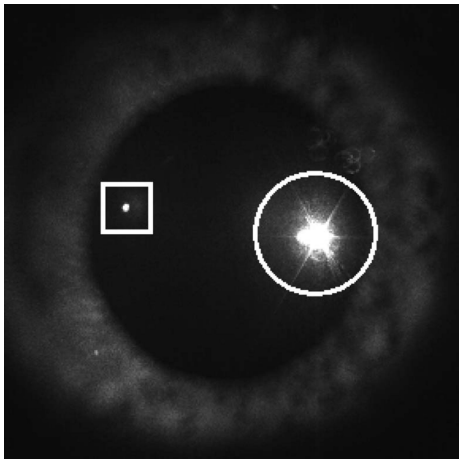

Figure 7.22: Registered image for the human living eye showing the first (circled) and the fourth (squared) Purkinje images. The image size is 4.5 mm by 4.5 mm.

7.3.2 Image acquisition and processing

Laboratory setup

The exposure time was the same for all subjects and experimental conditions. Series of P_{IV} were consecutively recorded for two different experimental conditions: with and without the RNDF. For the former condition P_{IV} was not saturated and was thought to capture the directional light. Its intensity was large enough to be well different from light coming from the surroundings. When the RNDF was removed from the illumination pathway, P_{IV} was saturated. This enhanced the information of the tails of P_{IV}, where the scattered portion of the light is located. All calculations were done using a purposely developed MATLAB (Mathworks, Inc.) script. For each acquired image a square area centered on P_{IV} was extracted (Figure 7.22). The averaged intensity radial profile centered on this Purkinje image was computed and normalized to 1. Once the radial profiles are known, the areas under the profiles are computed and named as k_{nonsat} and k_{sat} for the nonsaturated and saturated images, respectively. In particular, k_{nonsat} corresponded to the area under the radial profile of the image between 0 and 0.24 mm. For k_{sat} the range was the same, but excluding the saturated central pixels (i.e., those with a value of 1 in the normalized profile). BR was finally computed as:

$$BR = \frac{k_{sat}}{k_{sat} + k_{nonsat}} \tag{7.7}$$

To estimate the sensitivity of our instrument, the procedure was first tested in an artificial eye (see figure 7.21). This consisted of a scattering contact lens (CL, see chapter 5) acting as the cornea, placed in front of a polymethyl methacrylate biconvex intraocular lens (IOL), acting as the lens.

Clinical setup

In a clinical setup, we used a 660nm red LED placed at 10cm and under an incident angle of 40 degrees from the cornea. Also, the RNDF was removed. In order to enhance the dynamic range, the CCD took a series of 100 consecutive images (see figure 7.23).

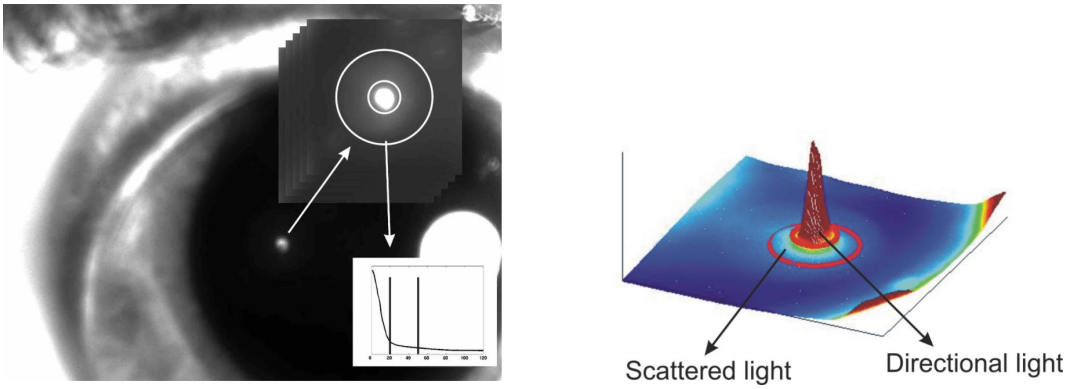

Figure 7.23: Image registration and analysis of P_{IV} in a clinical environment.

Images were registered on the fourth Purkinje image and scattering analysis was done on the registered image in a as previously described.

7.3.3 Restrictions of the method

Surface irregularities on the posterior lens surface

The lens consists of well organized crystalline fibers. This fiber packing leads to surface irregularities at the posterior and anterior lens surface. Given the small variation of the refractive index between the crystalline and vitreous and aqueous humor, this is believed to cause only a minor light scattering in retinal image formation. When imaging through the reflection of an irregular surface however, image degradation is more significant. We did not study the image degradation due to this surface irregularities. However, since that the reflection is done on the endothelial layer (the *lens capsule*, which is a cellular layer), this surface is considered to be more smooth than the anterior lens surface and therefore give rise to a better quality of the fourth Purkinje image.

Magnification of the scattering distribution

Another restriction of the analysis of the P_{IV} was suggested earlier in section 5.4.3. Figure 7.24 shows the position of the P_{IV} in respect to the posterior lens surface. The propagation of the scattered light entering and exiting the eye is also shown. We see that the position of the scattering surface is close to P_{IV}. When imaging P_{IV} on the CCD, the focal plane of the two scattering layers is slightly behind the CCD plane.

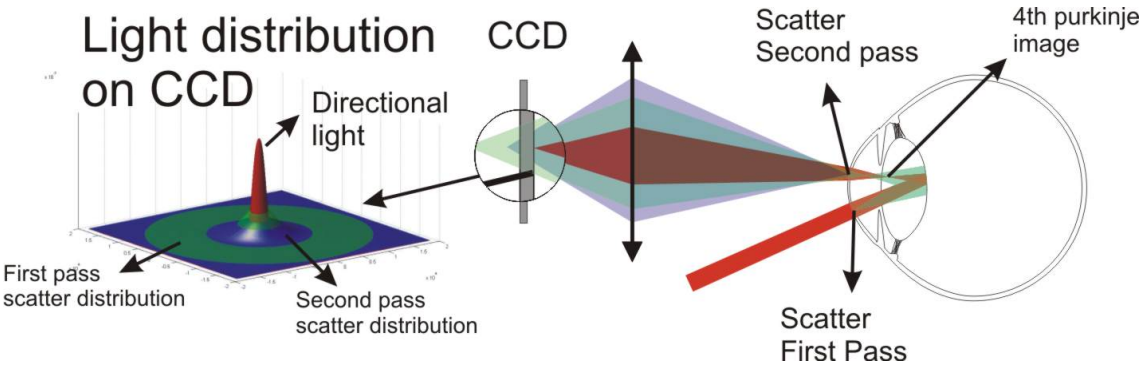

Figure 7.24: Light propagation of P_{IV}

Therefore, the defocused image of the scattering layers will make a halo around P_{IV} proportional to the scattering distribution of the scattering layers. The closer the focal plane of the scattering layers gets to the CCD plane, the more the scattering distribution will be concentrated close to P_{IV}. In the extreme case, the scattered light cannot be distinguished from the non scattered light. To minimize this effect, in the clinical setup, we optimized the experiment by placing the LED and CCD close to the eye. The scattering distribution of the first and the second pass in respect to the light distribution of P_{IV} on the CCD plane is simulated on the left of figure 7.24. ZEMAX simulations showed that the analyzed scattered light k_{nonsat} corresponds to light scattered over 3.33 to 4.17 degrees in the first pass and 2.1 to 2.7 degrees in the second pass.

7.3.4 Results of the Laboratory and Clinical setup

Laboratory setup

Eight normal young eyes from different subjects were involved in the study and used as a control group. In a subgroup of 2 eyes (eye 7 and eye 8) the complete procedure was carried out. That is, nonsaturated and saturated P_{IV} were acquired for those eyes wearing the two CLs. Since the unique difference is the amount of scatter introduced at the corneal plane by the CLs, this will allow us to determine that any significant change detected in the light intensity distribution of the image is due to the isolated effect of a variation in light scattering.

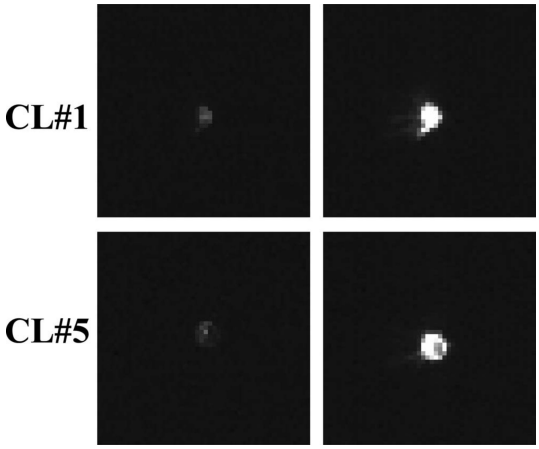

Figure 7.25: Images of the fourth Purkinje image in eye 7 for nonsaturated (left) and saturated (right) conditions with both CLs. Each image subtends 0.8 mm.

As an example figure 7.25 shows four images corresponding to the two experimental conditions and the two CLs. In figure 7.26A the values of BR for the 8 (naked) control eyes are depicted. We have also included the BR for the artificial eye with CL 1 as a reference. This plot shows that in normal control young eyes, the amount of scatter (measured as 1-BR) at the anterior chamber is similar for all subjects. Finally, in figure 7.26B we have plotted the results for eyes 7 and 8 and the artificial eye.

As a comparison we have also included the mean BR for the control eyes in figure 7.26A. Results show that in eyes wearing CL 5 the values of BR increase significantly: 16% and 23% for eye 7 and eye 8, respectively. In these experimental conditions, the amount of corneal haze is the only difference, which means these changes found in the measured BR are strictly due to the contribution of this induced scatter. For all eyes and within a CL, the values of k_{sat} were always larger that those of k_{nonsat}. However, when comparing both CLs, the values of k for nonsaturated images were similar. On the other hand, for saturated images there are noticeable differences between both CLs. The halo around P_{IV} contains contributions of the scattering due to roughness of the posterior lens surface and the bulk scattering in both the cornea and the crystalline lens. Light scattered from structures near the P_{IV} plane will contribute less to the peripheral halo around the image, as the scattered light will be almost in focus, coinciding with the directional image. For this reason, light scattered in the cornea results in a more peripheral halo than light scattered in the crystalline lens.

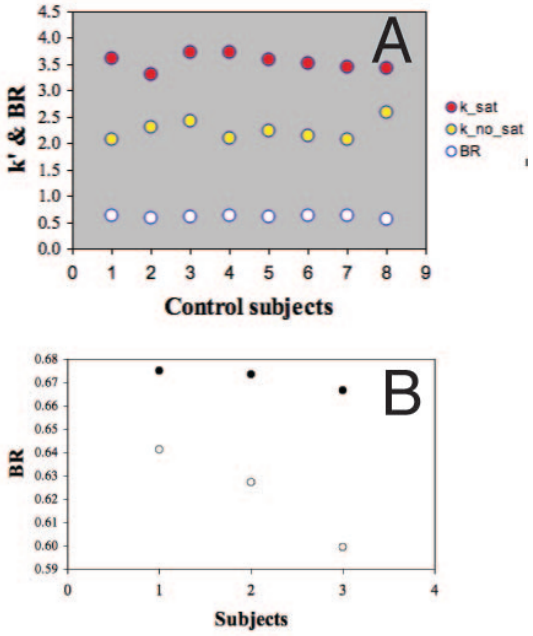

Figure 7.26: A:BR values for 8 control naked eyes and the artificial eye with CL 1. B:Values of BR for eyes 7,8 and the artificial eye, wearing the two scatter-customized CLs. The average BR for the (naked) control eyes has also been included as a comparison.

In summary, we have reported a technique to objectively extract the contribution of the ocular scattering coming from the cornea and the lens. This is based on a Purkinje imaging instrument. The procedure has successfully been tested in an artificial eye and in normal healthy eyes wearing scattercustomized CLs. Results show that the core of the image hardly changes when increasing scattering, but the intensity at the halos increases with the amount of induced scattering. The computed BR was sensitives enough to discriminate different induced levels of scattering at the anterior chamber.

Clinical setup

In the clinical setup, we measured in six eyes the BR for each subject wearing the five different scattering contact lenses. Over a set of 100 consecutively recorded images, we extracted a value of BR for each of the lenses applied on the subjects. The results are shown in figure 7.27. The same restrictions as described in the previous section should be taken into consideration.

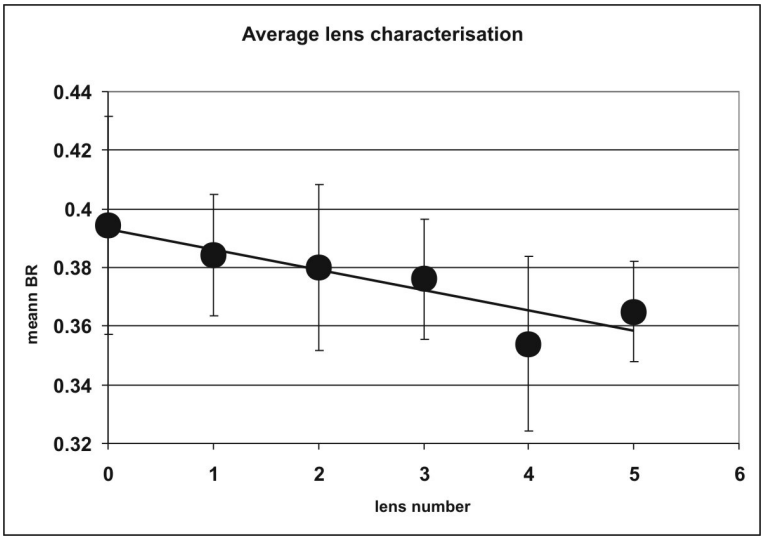

Figure 7.27: Results of the scattering analysis of the fourth purkinje image in 6 subjects wearing different contact lenses (results are averaged of the 6 subjects. The error bars show the standard deviation between the subjects).

7.3.5 Conclusion

Unlike the scattering analysis on Tscherning images, this method is not affected by interindividually varying retinal reflection. This allows us to compare light scattering in different eyes, comparing hazy corneas from clear corneas, etc. We have demonstrated that this method is able to detect small variations in small angle corneal light scattering. The low intensity of the fourth purkinje image forced us to maintain relatively long exposure times, in which eye movements could blur the fourth purkinje image. Increasing the size or luminance of the glare source (illumination LED), for instance by means of a ring-shaped LED array, could increase the amount of scattered light on the CCD and therefore reduce the extended exposure time.

Chapter 8

Light Scattering and Vision

In the previous chapters, we discussed the morphologic structures in the cornea that could explain light scattering. We have proposed some theoretical models describing the light scattering in the anterior part of the eye, further, a physical model to simulate the effect of increased light scattering has been proposed and finally, we have developed and described a number of (optical and psychophysical) methods to evaluate the amount of light scattering and its angular distribution of the light projected on the retina. In this chapter, we illustrate the effect of light scattering on the visual quality of the eye, specifically in respect to some natural scenes where light scattering can lead to significant reduction of information the scene perceived by the eye.

8.1 Assumptions

The small angle scattering distribution has not been evaluated in a large population. Moreover, the results obtained in this thesis are based on data from ten excised rabbit corneas. Given the different dimensions of the scattering structures in the cornea between healthy and hazy corneas, it is reasonable to suppose that the scattering distribution could not only have small intersubject variations, but also a different distribution of scattered light between low and high scattering corneas. Given the good similarity of wide angle scattering as estimated by psychophysical means (evaluated in a large population) and the wide angle distribution of the model described in section 4.3.2 (illustrated in figure 6.2), we will simulate the light scattering using the parameters obtained in section 7.1. Moreover, the good similarity on the wide angle data, evaluated

Haze grade	BR	log(s)	Age
0	1 to 0.78	< 1	0 to 63
1	0.67	1.1745	76
2	0.55	1.3069	86
3	0.43	1.408	93
4	0.31	1.49	100

Table 8.1: Comparison of values obtained in psychophysical model and ballistic simulation for clinically relevant values

for a population with a varying age, we can assume the same scattering distribution for light scattered in the cornea as the light scattered in the (ageing) crystalline lens. In table 8.1, we repeat the comparison between the amount in light scattering of the ageing eye and the hazy cornea to the interpolated values of BR as obtained from section 6.1.

In the following sections, we will simulate the effect of light scattering on the retinal image using these parameters.

8.2 Light scattering versus optical aberrations

In chapter 2, we have discussed that both the optical aberrations and the light scattering are detrimental for the retinal image quality. Moreover, based on the analysis of wavefront propagation in the anterior eye segment, in section 4.1, we pointed out the subtle relationship between aberrations and scattering, where scattering could be seen as a form of *very* high aberrations.

Principally, there are major differences between light scattering and aberrations though. It has previously been pointed out that the effect optical aberrations depends on the pupil size, whereas light scattering does not change by this. Also, regarding the *ballistic* model of scattering (section 4.3.2), only a portion of the incoming light gets scattered following the earlier defined scattering distribution. Optical aberrations on the other hand affect *all* the light entering the pupil by the *pupil function*.

It has also been discussed that the light distribution of PSF addressed to the optical aberrations is generally concentrated within the central 1 minute of arc (diffraction limited) op to 5 minutes of arc in a normal condition (-0.75 diopters, 4mm pupil).

Only 5% of the light scattered by the anomalous diffraction is scattered over and angle lower than 5 minutes of arc. Approximately 50% of the scattered light is scattered over an angle wider than 5 degrees.

8.3 Daylight scenes

8.3.1 Visual acuity

Clinically, the most common parameter to describe the optical quality of the eye is the visual acuity (VA). A patient is asked to read or distinguish a set of shapes (or letters) from a chart. VA is defined by the size of the smallest shapes the subject can still distinguish. A typical VA chart is shown on figure 8.1. The retinal image quality is simulated for different conditions of light scattering and aberrations. We see that whereas high aberrations can drastically reduce the visual acuity, even in the situation of very strong scattering, the retinal image of the visual acuity chart is not significantly reduced.

In figure 8.2, the VA chart is simulated for different amounts of light scattering (in the absence of aberrations). It is advisable however to recall the limitations of the scattering model used (section 4.3.2). In the model, we separated the image of the scattered light and the image of the non-scattered light. We did not consider different scattering distributions for low and highly scattering conditions. In section 4.1, we modeled scattering as a local wavefront distortion. Given the preliminary results of this study, it is reasonable to conclude that the scattering distribution will vary along the severity of the light scattering. Consequently, it is possible that severe (pathologic) light scattering eventually will affect the retinal image quality of the VA chart.

8.3.2 Contrast sensitivity function

In chapter 6, we proposed a method to extract the scattering information from the contrast sensitivity function. In figure 8.3, we simulated the effect of corneal scattering on the CSF for different levels of corneal scattering. Bear in mind that the CSF is expressed in a logarithmic scale, that scattering can reduce the CSF with a factor 2 to

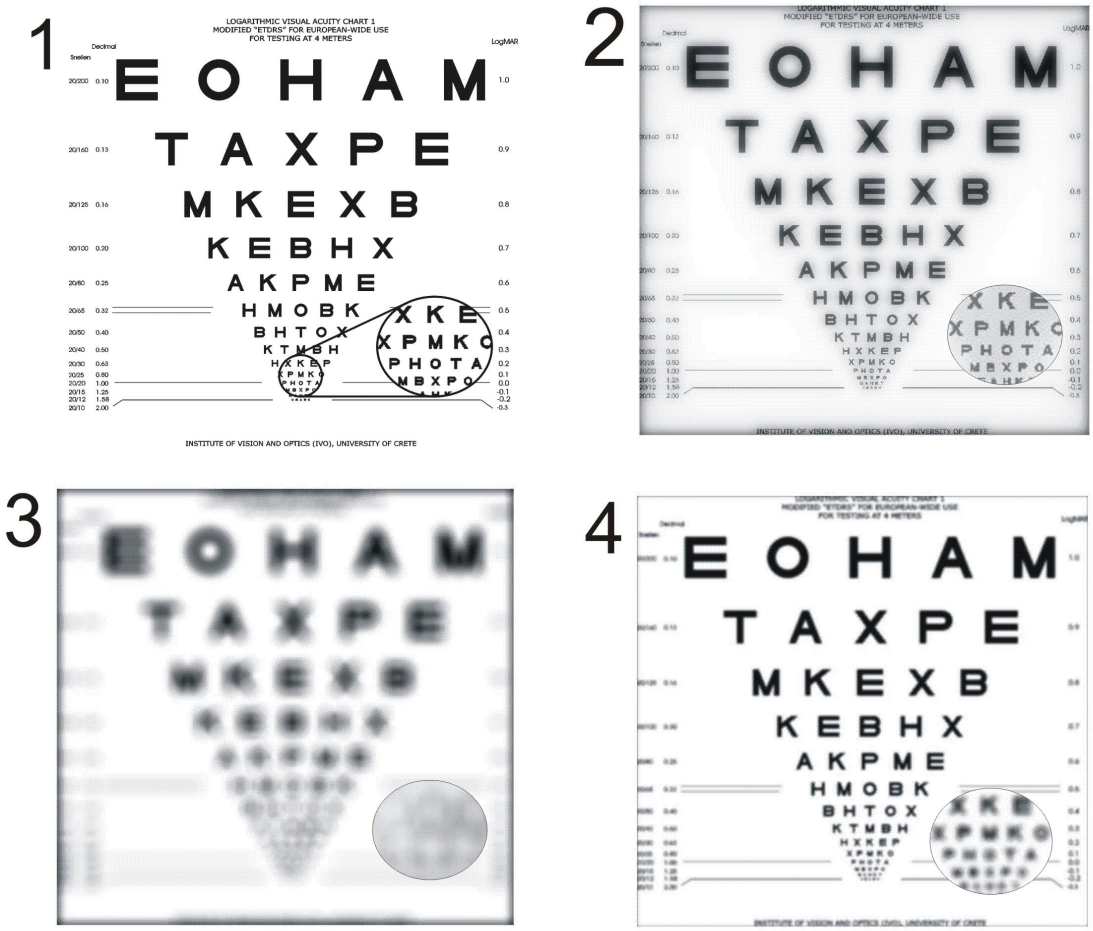

Figure 8.1: Simulation of the retinal image of a visual acuity chart in different conditions of the eye. 1. Absence of scattering and aberrations. 2. Absence of aberrations but highly scattering (Haze=4) 3. Absence of scattering but highly aberrated (-2D sphere, 4mm pupil diameter) 4. Normal condition of the eye (Haze=0, -0.4D sphere, 4mm pupil)

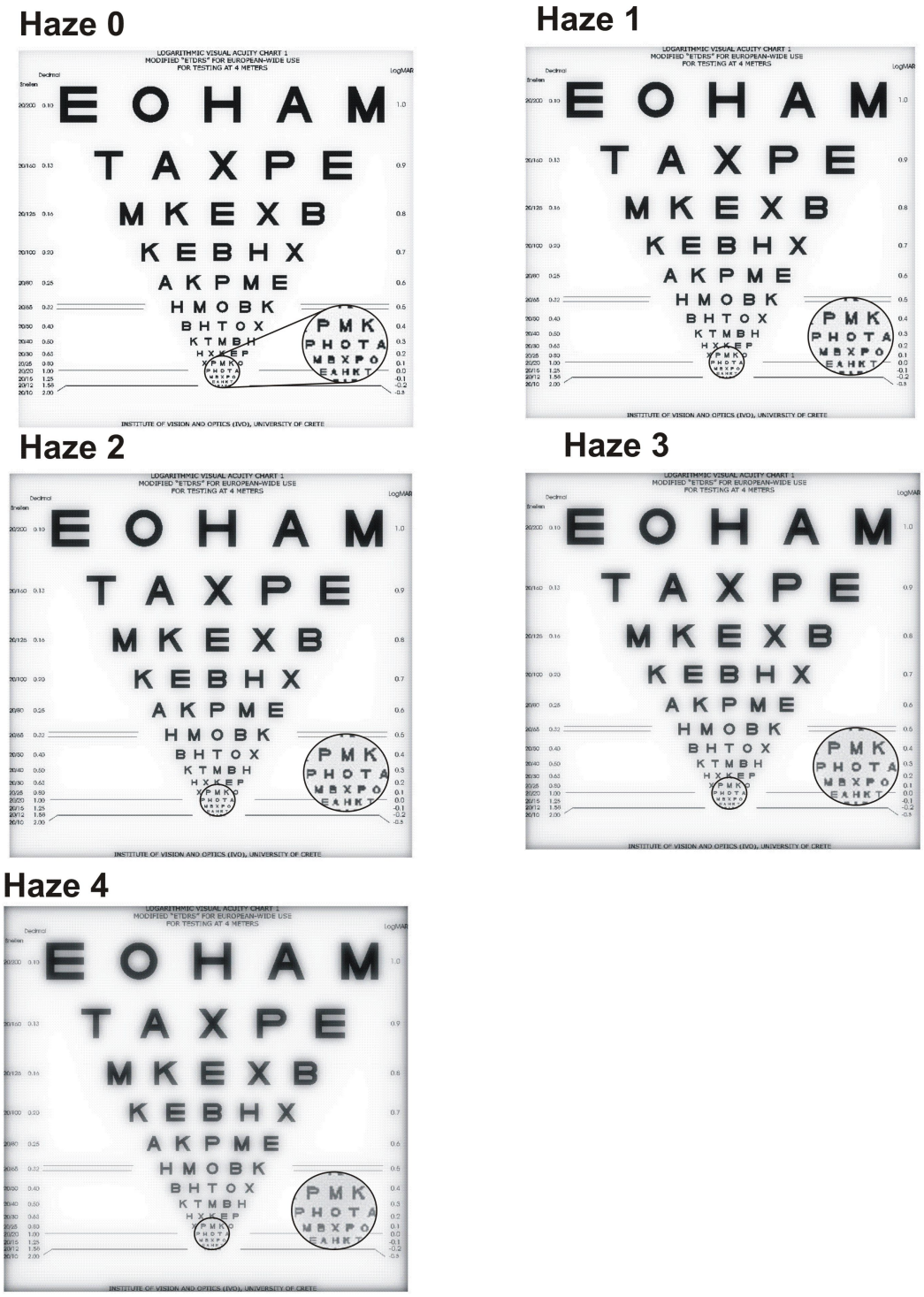

Figure 8.2: Retinal image quality for different amounts of light scattering, in the absence of light scattering

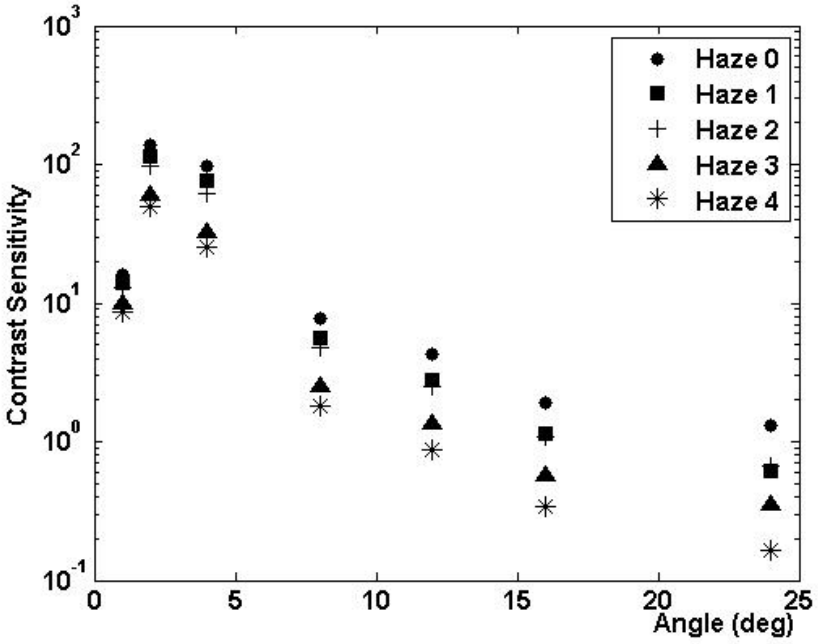

Figure 8.3: CSF affected by the different levels of corneal scattering.

10 for severe scattering, depending on the angle.

8.4 Night vision

8.4.1 Traffic scenes

From the previous section, we can conclude that ocular light scattering is more detrimental for the loss of contrast sensitivity than the reduction of acuity in the visual function. The effect of light scattering is therefore more dramatic in natural scenes with high contrast, e.g. traffic scenes at night. A typical scene is illustrated in figure 8.4. The major glare sources are the headlights of the car. In a highly scattering eye, the disability glare associated with the headlights is more luminant than the objects around the lights. This can be the reason why an observer cannot distinguish the passenger on the side of the street. Obviously, the effect of scattering on a traffic scene is more dramatic in the absence of ambient illumination (e.g. of the street lights), or with more intense glare sources (mist lamps or high beams, where bleaching of the photoreceptors causes the known "blinding" effect).

Figure 8.4: Simulation of light scattering in a night traffic scene

8.5 What are the alternatives?

So far, we have evaluated the effect of refractive surgery on the retinal image quality, in particular to the amount of light scattering addressed to the treatment. In this section, we will compare the scattering levels addressed to the common methods for the correction of the refractive error.

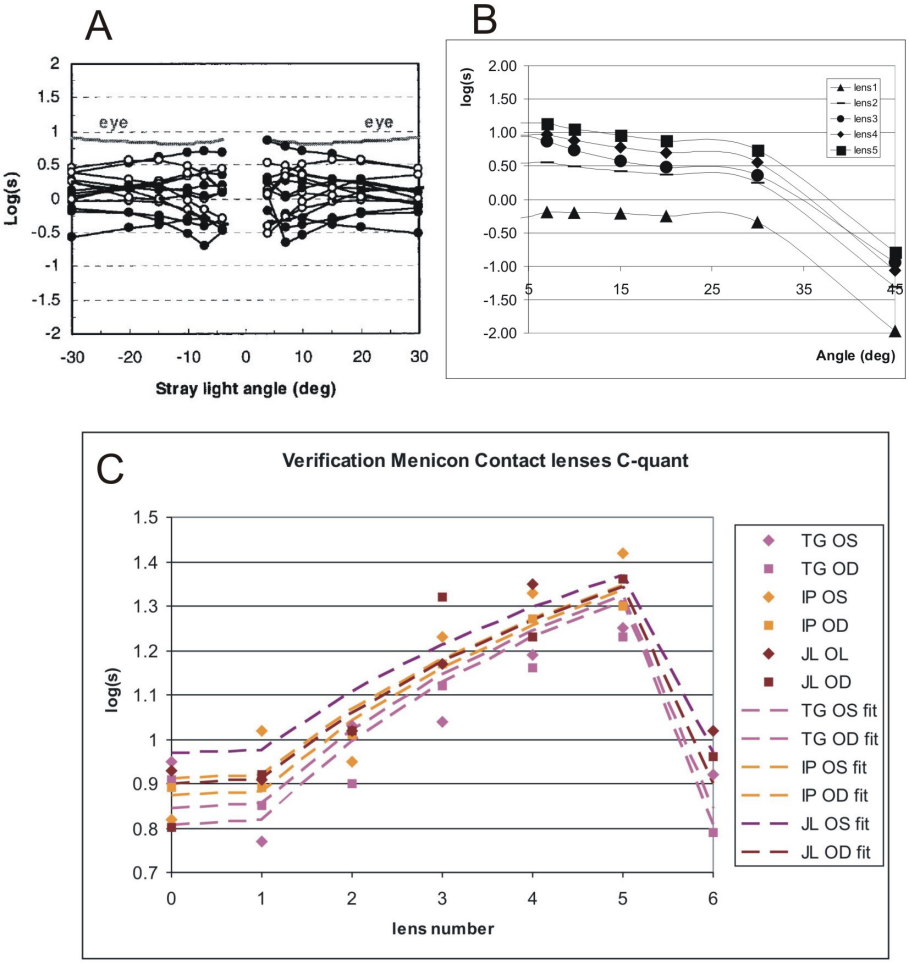

Figure 8.5: Comparison of wide angle log(s)-values in daily used spectacle glasses and the calibrated scattering contact lenses. A. log(s) values of daily used spectacles[12]. B. Wide angle calibration of scattering contact lenses C. Effect of scattering contact lenses on psychophysical log(s) values.

8.5.1 Light scattering on spectacles

Dust particles, fingerprints and scratches on the surface of spectacle lenses will cause a local distortion of the incoming wavefront and therefore be the source of light scattering affecting the retinal image quality.

Figure 8.6 illustrates the different amount of light scattering between cleaned and dirty lenses. De Wit and Coppens studied the wide angle scattering of a number of spectacle lenses as the users were wearing them[12]. They observed large variations of scattering levels on the spectacle lenses. The results are given in figure 8.5. We observe a similarity on log(s) values for the dirty spectacle lenses and the calibrated scattering contact lenses as earlier described in chapter 5. We recall that the results of

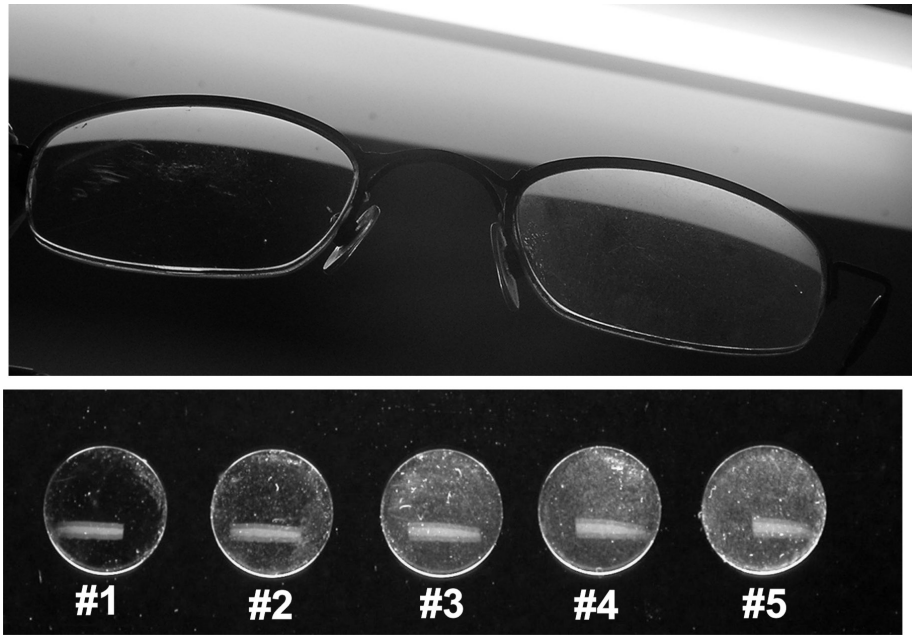

Figure 8.6: Different scattering levels in spectacles and scattering contact lenses

section 6.3 as shown in figure 8.5C suggest the increased scattering addressed to the scattering contact lenses simulate scattering levels similar to haze 2 as often clinically assessed.

8.5.2 Light scattering on Contact lenses

To our knowledge, there has not been made large studies on the ocular light scattering addressed the the wearing of contact lenses.

Origin of scattering on contact lenses

A contact lens is placed in direct contact with the cornea. Recalling the corneal morphology described in chapter 3, the tear film, refreshed by eye blinks, is now mainly distributed over the contact lens surface. The optical quality of the tear film depends on the type of contact lens used[55]. On the other hand, epithelial debris, sandwiched between the epithelium and contact lens have a reduced mobility and can give rise to light scattering (see the epithelial debris observed in confocal microscopy in figure 3.2). The epithelial debris is removed after removal and cleaning of the contact lens.
Moreover, since the cornea is not anymore directly exposed to the air, the corneal

tissue is less oxygenized causing local edema between the stromal collagen layers[48]. This edema can also lead to increased light scattering.
Handling contact lenses (cleaning, applying and removal) is generally done with the hands and repeatedly mechanical stress on the lens accompanied with this handling could lead to scratches on the lens surface inducing light scattering.

Measurement of forward light scattering on contact lenses

Some of the possible origins of contact lens scattering is not due to the optical quality of the lens, but related to the interaction between the contact lens and the cornea. It is therefore advisable to estimate light scattering on contact lenses by psychophysical means (section 6.3). The reflectivity of the previously described scattering particles can be visualized with confocal microscopy.

Conclusion

Apart from the surface irregularities on contact lenses due to handling, the morphologic response of the cornea on the use of contact lenses can lead to increased corneal light scattering. These scatterers probably accumulate with the time a subject consecutively wears the contact lens. It would be of interest to study the effect of contact lens wearing on light scattering in a large population, in particular related to the amount of time a subject consecutively wears the contact lens.

8.6 Conclusion

The effect of ocular light scattering on the visual function can give rise a loss of contrast sensitivity. Therefore, light scattering can significantly reduce the information in an image when a low luminary object is placed next to a high luminary glare source, such as often occurs in traffic scenes at night.
The effect of increased corneal light scattering after refractive excimer surgery can be associated with the morphologic changes related to the corneal healing process. The activation of highly reflective keratocytes

Appendix A

Mathematical Description of Rayleigh Scattering

The scattering function on such a particle is defined by $S(\theta, \phi)$, describing the amplitude and phase of a wavefront u scattered by the particle over the solid angle $d\theta d\phi$. In the absence of absorption, a scattering particle will cause a disturbance to the plane wavefront u_0 given by

$$u_0 = e^{-ikz+i\omega t} \tag{A.1}$$

In the far field, the scattered wave is seen as a spherical wave originating from the scattering particle. Therefore, it can be written as following:

$$u = S(\theta, \phi)\frac{e^{-ikr+i\omega t}}{ikr} \tag{A.2}$$

Combining both equations gives us:

$$u = S(\theta, \phi)\frac{e^{-ikr+ikz}}{ikr}u_0 \tag{A.3}$$

The function S is, in general, complex and can thus be written as

$$S(\theta, \phi) = s \cdot e^{i\sigma} \tag{A.4}$$

The intensity of the scattered wave is proportional the the square of the amplitude:

$$I_{sca} = \frac{s^2(\theta, \phi)}{k^2 r^2} I_0 \tag{A.5}$$

Introducing an incoming polarized wavefront, we should extend the scattering function S into fur different amplitude functions S_1, S_2, S_3 and S_4, which form a *scattering tensor* $\mathbf{S}(\theta, \phi)$. We can thus replace the definition of $S(\theta, \phi)$ by

$$\begin{pmatrix} E_l \\ E_r \end{pmatrix} = \begin{pmatrix} S_2 & S_3 \\ S_4 & S_1 \end{pmatrix} \cdot \frac{e^{-ikr+ikz}}{ikr} \begin{pmatrix} E_{l0} \\ E_{r0} \end{pmatrix} \tag{A.6}$$

The latter formulae for spherical particles can be simplified since spherical particles have $S_3 = S_4 = 0$. Two complex functions remain and are only dependent on the azimuth scattering angle θ. The latter function can now be separated in two equations:

$$\begin{aligned} E_r &= S_1\theta\tfrac{e^{-ikr+ikz}}{ikr}E_{r0} \\ E_l &= S_2\theta\tfrac{e^{-ikr+ikz}}{ikr}E_{l0} \end{aligned} \tag{A.7}$$

where r and l refer to the orientation of the electric field to the plane of scattering.

A.1 Rayleigh Scattering

However Rayleigh Scattering applies to particles with size much smaller than the wavelength, it contains the fundamental idea of the scattering theory on particles with various size. When a plane wave, characterized by its electric field E_0 reaches a small particle, the particles gets excited by the field, and will behave as a dipole. Let p be the induced dipole moment from the particle, we can propose following relationship:

$$p = \alpha E_0 \tag{A.8}$$

In this relation, the *polarizability* α of the particle is defined. The electric field of the scattered wave attributed to the dipole in a point P at a distance $r \gg \lambda$ from the particle and in a direction that makes an angle γ with $\mathbf{p}$ is

$$E = \frac{k^2 p \sin\gamma}{r} d^{-ikr} \tag{A.9}$$

In the situation of *isotropic polarizability*, the polarizability becomes a scalar and

the angle γ equals the angle θ between E_0 and the scattering direction. The scattering tensor as defined in formula A.6 can now be written as:

$$\begin{pmatrix} S_2 & S_3 \\ S_4 & S_1 \end{pmatrix} = ik^3\alpha \begin{pmatrix} \cos\theta & 0 \\ 0 & 1 \end{pmatrix} \tag{A.10}$$

The intensity of the scattered light under an angle θ with natural incident light and intensity I_0 can be found as

$$I = \frac{(1 + cos^2\theta)k^4|\alpha|^2}{2r^2} I_0 \tag{A.11}$$

A.2 Rayleigh-Gans scattering

The formula for Rayleigh scattering only applies for particles with dimensions smaller than the wavelength. However, the theory can easily be generalized to larger particles, better known as the *Rayleigh-Gans* theory. Any scattering particle can be seen as a union of small volumes so small that they follow the Rayleigh theory. The waves scattered by these subvolumes interfere because of the different positions of the volume elements in space. In order to calculate these interference effects, one should add a phase shift to the scattered wave. This is done by adding a complex amplitude $e^{i\delta}$ to the expressions above. Each element now gives

$$\begin{pmatrix} S_1 \\ S_1 \end{pmatrix} = \frac{ik^3(m-1)}{2\pi} e^{i\delta} dV \begin{pmatrix} 1 \\ \cos\theta \end{pmatrix} \tag{A.12}$$

For the entire particle, we obtain:

$$\begin{pmatrix} S_1 \\ S_2 \end{pmatrix} = \frac{ik^3(m-1)}{2\pi} R(\theta,\phi) \begin{pmatrix} 1 \\ \cos\theta \end{pmatrix} \tag{A.13}$$

where

$$R(\theta,\phi) = \frac{1}{V}\int e^{i\delta} dV \tag{A.14}$$

To calculate the scattering on a sphere with *radius a*, we make following substi-

tutions:

$$x = ka, \quad b = za, \quad u = 2x \sin\frac{\theta}{2}, \quad \delta = zu \tag{A.15}$$

then the particle consists of a series of "slices" with thickness adz and radius $a\sqrt{1-z^2}$ so that we can integrate over the volume of the particle:

$$R(\theta, \phi) = \frac{1}{V} \int_{-1}^{+1} e^{izu} \pi a^2 (1 - z^2) a dz = G(u) \tag{A.16}$$

where

$$\begin{aligned} G(u) &= 3/2 \int_0^1 \cos zu \cdot (1 - z^2) dz \\ &= \frac{9\pi}{2u^3} J_{\frac{3}{2}}(u) \end{aligned} \tag{A.17}$$

The full amplitude functions for a sphere under these conditions become

$$\begin{pmatrix} S_1(\theta) \\ S_2(\theta) \end{pmatrix} = ik^3 a^3 (m-1) \frac{2\pi}{u^3}^{\frac{1}{2}} J_{\frac{3}{2}}(u) \begin{pmatrix} 1 \\ \cos\theta \end{pmatrix} \tag{A.18}$$

Bibliography

[1] P. Artal, A. Benito, and J. Tabernero, *The human eye is an example of robust optical design*, J Vis **6** (2006), 1–7.

[2] F.A. Bettelheim, *Light scattering in lens research: an essay on accomplishments and promises*, Exp. Eye Res. **79** (2004), 747–752.

[3] D De Brouwere, HS Ginis, GD Kumionis, I Naomidi, and IG Pallikaris, *Forward scattering properties of corneal haze*, Optom Vis Sci (2008), in press.

[4] J.M. Bueno, *Depolarization effects in the human eye*, Vision Res. **41** (2001), 2687–2696.

[5] Juan M. Bueno, Dirk De Brouwere, Harilaos Ginis, Ioannis Sgouros, and Pablo Artal, *Purkinje imaging system to measure anterior segment scattering in the human eye*, Opt. Lett. **32** (2007), no. 23, 3447–3449.

[6] F.W. Campbell and D.G. Green, *Optical and retinal factors affecting visual resolution*, J. Physiol. (Lond.) **181** (1965), 576–593.

[7] W.N. Charman, D.A. Atchison, and D.H. Scott, *Theoretical analysis of peripheral imaging after excimer laser corneal refractive surgery for myopia*, J Cataract Refract Surg **28** (2002), 2017–2025.

[8] C.J. Connon, K.M. Meek, R.H. Newton, M.C. Kenney, S.A. Alba, and H. Karageozian, *Hyaluronidase treatment, collagen fibril packing, and normal transparency in rabbit corneas*, J Refract Surg **16** (2000), 448–455.

[9] C.A. Curcio and K.R. Sloan, *Packing geometry of human cone photoreceptors: variation with eccentricity and evidence for local anisotropy*, Vis. Neurosci. **9** (1992), 169–180.

[10] M.B. Datiles, R.R. Ansari, and G.F. Reed, *A clinical study of the human lens with a dynamic light scattering device*, Exp. Eye Res. **74** (2002), 93–102.

[11] D.G. Dawson, H.F. Edelhauser, and H.E. Grossniklaus, *Long-term histopathologic findings in human corneal wounds after refractive surgical procedures*, Am. J. Ophthalmol. **139** (2005), 168–178.

[12] G.C. De Wit and J.E. Coppens, *Stray light of spectacle lenses compared with stray light in the eye*, Optom Vis Sci **80** (2003), 395–400.

[13] Juan A. del Val, Sonia Barrero, Bety Y aez, Jesús Merayo, Juan A. Aparicio, Víctor R. González, José C. Pastor, and Santiago Mar, *Experimental measurement of corneal haze after excimer laser keratectomy*, Appl. Opt. **40** (2001), no. 10, 1727–1734.

[14] Vasilios F Diakonis, Aristophanis Pallikaris, George D Kymionis, and Marinos M Markomanolakis, *Alterations in endothelial cell density after photorefractive keratectomy with adjuvant mitomycin.*, Am J Ophthalmol **144** (2007), no. 1, 99–103 (eng).

[15] N. Drasdo, C.M. Thompson, and W.N. Charman, *Inconsistencies in models of the human ocular modulation transfer function*, Vision Res. **34** (1994), 1247–1253.

[16] I. Dror, A. Sandrov, and N.S. Kopeika, *Experimental investigation of the influence of the relative position of the scattering layer on image quality: the shower curtain effect*, Appl Opt **37** (1998), 6495–6499.

[17] D.B. Elliott, *Contrast sensitivity decline with ageing: a neural or optical phenomenon?*, Ophthalmic Physiol Opt **7** (1987), 415–419.

[18] Fantes FE, Hanna KD, Waring GO 3r, Pouliquen Y, Thompson KP, and Savoldelli M., *Wound healing after excimer laser keratomileusis (photorefractive keratectomy) in monkeys.*, Arch Ophthalmol. **108** (1990), no. 5, 665–675.

[19] L. Franssen, J.E. Coppens, and T.J. van den Berg, *Compensation comparison method for assessment of retinal straylight*, Invest. Ophthalmol. Vis. Sci. **47** (2006), 768–776.

[20] M.H. Friedlaender, *LASIK surgery using the IntraLase femtosecond laser*, Int Ophthalmol Clin **46** (2006), 145–153.

[21] A. Garg, TJ Lin, JL Alio, R. Azad, JJ Bevot, B Pajic, and CK Mehta, *Mastering the techniques of laser applications in ophthalmology*, Jaypee Brothers, New Dehli, 2008.

[22] Trisevgenie Gianakopoulou, *Evaluation of contrast sensitivity function following refractive surgery*, Institute of Vision and Optics, University of Crete, Heraklion, 2006.

[23] Joseph W. Goodman, *Introduction to fourier optics*, McGraw-Hill, New York, 1968.

[24] R.W. Hart and R.A. Farrell, *Light scattering in the cornea*, J Opt Soc Am **59** (1969), 766–774.

[25] M.L. Hennelly, J.L. Barbur, D.F. Edgar, and E.G. Woodward, *The effect of age on the light scattering characteristics of the eye*, Ophthalmic Physiol Opt **18** (1998), 197–203.

[26] I.J. Hodgkinson, P.B. Greer, and A.C. Molteno, *Point-spread function for light scattered in the human ocular fundus*, J Opt Soc Am A Opt Image Sci Vis **11** (1994), 479–486.

[27] B. Hohberger, R. Laemmer, W. Adler, A.G. Juenemann, and F.K. Horn, *Measuring contrast sensitivity in normal subjects with OPTEC(R) 6500: influence of age and glare*, Graefes Arch. Clin. Exp. Ophthalmol. **245** (2007), 1805–1814.

[28] J.K. IJspeert, T.J. van den Berg, and H. Spekreijse, *An improved mathematical description of the foveal visual point spread function with parameters for age, pupil size and pigmentation*, Vision Res. **33** (1993), 15–20.

[29] A. Ivarsen, T. Laurberg, and T. M?ller-Pedersen, *Role of keratocyte loss on corneal wound repair after LASIK*, Invest. Ophthalmol. Vis. Sci. **45** (2004), 3499–3506.

[30] Y. Kaji, K. Soya, S. Amano, T. Oshika, and H. Yamashita, *Relation between corneal haze and transforming growth factor-beta1 after photorefractive keratectomy and laser in situ keratomileusis*, J Cataract Refract Surg **27** (2001), 1840–1846.

[31] Paul Kaufman, *Adler's physiology of the eye*, Elsevier, NOV-2002.

[32] H Kukkonen, J Rovamo, K Tiippana, and R Nasanen, *Michelson contrast, rms contrast and energy of various spatial stimuli at threshold.*, Vision Res **33** (1993), no. 10, 1431–1436 (eng).

[33] S. Marcos and S.A. Burns, *Cone spacing and waveguide properties from cone directionality measurements*, J Opt Soc Am A Opt Image Sci Vis **16** (1999), 995–1004.

[34] K.M. Meek and C. Boote, *The organization of collagen in the corneal stroma*, Exp. Eye Res. **78** (2004), 503–512.

[35] K.M. Meek, D.W. Leonard, C.J. Connon, S. Dennis, and S. Khan, *Transparency, swelling and scarring in the corneal stroma*, Eye **17** (2003), 927–936.

[36] T. Moller-Pedersen, H.D. Cavanagh, W.M. Petroll, and J.V. Jester, *Stromal wound healing explains refractive instability and haze development after photorefractive keratectomy: a 1-year confocal microscopic study*, Ophthalmology **107** (2000), 1235–1245.

[37] E. Moreno-Barriuso and R. Navarro, *Laser Ray Tracing versus Hartmann-Shack sensor for measuring optical aberrations in the human eye*, J Opt Soc Am A Opt Image Sci Vis **17** (2000), 974–985.

[38] C.R. Munnerlyn, S.J. Koons, and J. Marshall, *Photorefractive keratectomy: a technique for laser refractive surgery*, J Cataract Refract Surg **14** (1988), 46–52.

[39] R Navarro, J Santamaria, and J Bescos, *Accommodation-dependent model of the human eye with aspherics.*, J Opt Soc Am A **2** (1985), no. 8, 1273–1281 (eng).

[40] I.G. Pallikaris, V.J. Katsanevaki, M.I. Kalyvianaki, and I.I. Naoumidi, *Advances in subepithelial excimer refractive surgery techniques: Epi-LASIK*, Curr Opin Ophthalmol **14** (2003), 207–212.

[41] I.G. Pallikaris, I.E. Lambropoulos, P.K. Kolydas, N.S. Nicolopoulos, and I.E. Kotsiras, *Excimer laser photorefractive keratectomy for myopia: clinical results in 96 eyes*, Refract Corneal Surg **9** (1993), S101–102.

[42] I.G. Pallikaris, I.I. Naoumidi, M.I. Kalyvianaki, and V.J. Katsanevaki, *Epi-LASIK: comparative histological evaluation of mechanical and alcohol-assisted epithelial separation*, J Cataract Refract Surg **29** (2003), 1496–1501.

[43] I.G. Pallikaris, M.E. Papatzanaki, E.Z. Stathi, O. Frenschock, and A. Georgiadis, *Laser in situ keratomileusis*, Lasers Surg Med **10** (1990), 463–468.

[44] Anastasios Papadiamantis, *Development of a interferometric instrument for the measurement of the retinal response on contrast gratings.*, Institute of Vision and Optics, University of Crete, Heraklion, 2006.

[45] I. Perez-Gomez and N. Efron, *Change to corneal morphology after refractive surgery (myopic laser in situ keratomileusis) as viewed with a confocal microscope*, Optom Vis Sci **80** (2003), 690–697.

[46] J. Porter, A. Guirao, I.G. Cox, and D.R. Williams, *Monochromatic aberrations of the human eye in a large population*, J Opt Soc Am A Opt Image Sci Vis **18** (2001), 1793–1803.

[47] Hema Radhakrishnan and W Neil Charman, *Age-related changes in ocular aberrations with accommodation.*, J Vis **7** (2007), no. 7, 11.1–21 (eng).

[48] Daniele P Saltarelli, *Hyper oxygen-permeable rigid contact lenses as an alternative for the treatment of pediatric aphakia.*, Eye Contact Lens **34** (2008), no. 2, 84–93 (eng).

[49] T Seiler and P J McDonnell, *Excimer laser photorefractive keratectomy.*, Surv Ophthalmol **40** (1995), no. 2, 89–118 (eng).

[50] Ioannis Sgouros, *A physicalmodelnto simulate the corneal light scattering after refractive surgery by means of a suspension of microspheres in a collagen background matrix.*, Institute of Vision and Optics, University of Crete, Heraklion, 2006.

[51] Smith, *Light and the eye*, Springer-Verlag, New York, 1973.

[52] K. Soya, S. Amano, and T. Oshika, *Quantification of simulated corneal haze by measuring back-scattered light*, Ophthalmic Res. **34** (2002), 380–388.

[53] B D Srinivasan, *Corneal reepithelialization and anti-inflammatory agents.*, Trans Am Ophthalmol Soc **80** (1982), 758–822 (eng).

[54] W. S. Stiles, *The scattering theory of the effect of glare on the brightness difference threshold*, Proceedings of the Royal Society of London. Series B, Containing Papers of a Biological Character **105** (1929), no. 735, 131–146.

[55] Dorota H Szczesna, Jaroslaw Jaronski, Henryk T Kasprzak, and Ulf Stenevi, *Interferometric measurements of dynamic changes of tear film.*, J Biomed Opt **11** (2006), no. 3, 34028 (eng).

[56] I. Thornton, M. Xu, and R.R. Krueger, *Comparison of standard (0.02) and low dose (0.002) mitomycin C in the prevention of corneal haze following surface ablation for myopia*, J Refract Surg **24** (2008), 68–76.

[57] H. C. van de Hulst, *Light scattering by small particles.*

[58] Thomas J.T.P van den Berg and Jan Kees IJspeert, *Clinical assessment of intraocular straylight*, Appl. Opt. **31** (1992), no. 19, 3694.

[59] T.J. van den Berg, *Analysis of intraocular straylight, especially in relation to age*, Optom Vis Sci **72** (1995), 52–59.

[60] TJ van den Berg, *Light scattering by donor lenses as a function of depth and wavelength*, Invest. Ophthalmol. Vis. Sci. **38** (1997), 1321–1332.

[61] T.J. van den Berg, M.P. Hagenouw, and J.E. Coppens, *The ciliary corona: physical model and simulation of the fine needles radiating from point light sources*, Invest. Ophthalmol. Vis. Sci. **46** (2005), 2627–2632.

[62] T.J. van den Berg and H. Spekreijse, *Light scattering model for donor lenses as a function of depth*, Vision Res. **39** (1999), 1437–1445.

[63] JJ Vos and TJ van den Berg, *Report on disability glare*, 1999, pp. 1–9.

[64] D.R. Williams, *Aliasing in human foveal vision*, Vision Res. **25** (1985), 195–205.

List of Figures

List of Tables